

Washington University in St. Louis

## Washington University Open Scholarship

---

Arts & Sciences Electronic Theses and  
Dissertations

Arts & Sciences

---

Winter 12-15-2021

### Genetic risk factors for neurodevelopmental disorders: insights from hiPSC-cerebral organoids

Michelle L. Wegscheid  
*Washington University in St. Louis*

Follow this and additional works at: [https://openscholarship.wustl.edu/art\\_sci\\_etds](https://openscholarship.wustl.edu/art_sci_etds)



Part of the [Developmental Biology Commons](#), and the [Neurosciences Commons](#)

---

#### Recommended Citation

Wegscheid, Michelle L., "Genetic risk factors for neurodevelopmental disorders: insights from hiPSC-cerebral organoids" (2021). *Arts & Sciences Electronic Theses and Dissertations*. 2628.  
[https://openscholarship.wustl.edu/art\\_sci\\_etds/2628](https://openscholarship.wustl.edu/art_sci_etds/2628)

This Dissertation is brought to you for free and open access by the Arts & Sciences at Washington University Open Scholarship. It has been accepted for inclusion in Arts & Sciences Electronic Theses and Dissertations by an authorized administrator of Washington University Open Scholarship. For more information, please contact [digital@wumail.wustl.edu](mailto:digital@wumail.wustl.edu).

WASHINGTON UNIVERSITY IN ST. LOUIS

Division of Biology and Biomedical Sciences  
Neurosciences

Dissertation Examination Committee:

David H. Gutmann, Chair  
Aaron DiAntonio, Co-Chair  
Kristen Kroll  
Lilianna Solnica-Krezel  
Andrew Yoo

Genetic Risk Factors for Neurodevelopmental Disorders: Insights from hiPSC-Cerebral  
Organoids  
by  
Michelle L. Wegscheid

A dissertation presented to  
The Graduate School  
of Washington University in  
partial fulfillment of the  
requirements for the degree  
of Doctor of Philosophy

May 2022  
St. Louis, Missouri

© 2022, Michelle L. Wegscheid

# Table of Contents

List of Figures .....	iv
List of Tables .....	vi
Acknowledgments.....	vii
Abstract.....	x
Chapter 1: Introduction & Perspective .....	1
1.1 Preface.....	2
1.2 Barriers to precision medicine.....	3
1.3 Clinical heterogeneity in Neurofibromatosis type 1 (NF1).....	4
1.4 Germline <i>NF1</i> gene mutations .....	5
1.5 Personalized preclinical models.....	6
1.6 Human induced pluripotent stem cells (hiPSCs).....	8
1.7 Human iPSC-derived cerebral organoids (hCOs) .....	9
1.8 Directions .....	11
Chapter 2: Isogenic hiPSC-derived CNS cells and hCOs establish differential effects of <i>NF1</i> gene mutations .....	14
2.1 Preface.....	15
2.2 Abstract .....	16
2.3 Introduction .....	16
2.4 Materials and methods .....	17
2.5 Results .....	24
2.6 Figures and tables.....	29
2.7 Discussion .....	46
Chapter 3: hiPSC-derived hCOs harboring a 17q11.2 microdeletion reveal <i>CRLF3</i> as a critical regulator of neurogenesis.....	49
3.1 Preface.....	50
3.2 Abstract .....	51
3.3 Introduction .....	51
3.4 Materials and methods .....	53

3.5	Results .....	62
3.6	Figures and tables.....	70
3.7	Discussion .....	98
Chapter 4: Conclusions and Future Directions .....		100
4.1	Preface.....	101
4.2	Summary of findings.....	102
4.3	Future directions.....	107
4.3.1	Mechanistic etiologies.....	108
4.3.2	Prospective directions for hCO modeling of NF1-associated brain pathologies ..	113
4.4	Concluding Remarks .....	120
References.....		121
Curriculum Vitae .....		138

# List of Figures

## **Chapter 1**

Figure 1.1   Precision medicine.	3
Figure 1.2   hiPSCs for disease modeling in NF1.	9
Figure 1.3   Cerebral organoid cultures.	12
Figure 1.4   Schematic diagram showing the chromosomal region 17q11.2.	13

## **Chapter 2**

Figure 2.1   Isogenic <i>NF1</i> -mutant hiPSC sequencing and allele expression analysis of isogenic and patient-derived <i>NF1</i> -mutant hiPSCs.	29
Figure 2.2   Analysis of isogenic hiPSCs, NPCs, and cerebral organoids.	31
Figure 2.3   Isogenic <i>NF1</i> -mutant hiPSC-derived NPCs exhibit increased RAS activity and cell proliferation.	33
Figure 2.4   Comparisons between isogenic and patient-derived <i>NF1</i> -mutant hiPSC-NPCs.	35
Figure 2.5   hiPSC-derived <i>NF1</i> -mutant astroglia exhibit increased RAS activity and cell proliferation.	37
Figure 2.6   Comparisons between isogenic and patient-derived <i>NF1</i> -mutant hiPSC-organoids.	39
Figure 2.7   hiPSC-derived <i>NF1</i> -mutant neurons, NPCs, and <i>Nf1</i> -mutant mice display molecular similarities and differences.	41
Figure 2.8   Differential effects of <i>NF1</i> mutations on cerebral organoid progenitor cell dynamics and neurogenesis.	42

## **Chapter 3**

Figure 3.1   Patient-derived hiPSCs and hCOs.	70
---	----

Figure 3.2   TGD hCOs and neurons exhibit neuronal defects.	72
Figure 3.3   Neuronal differentiation defects in TGD and intragenic <i>NF1</i> -mutant hCOs.	74
Figure 3.4   RAS hyperactivation drives the increased NSC proliferation in TGD organoids.	76
Figure 3.5   RAS activity and differential gene expression analysis of TGD and CTL hCOs.	78
Figure 3.6   <i>CRLF3</i> is uniquely disrupted in TGD hCOs and NF1 patients with increased SRS-2 scores.	81
Figure 3.7   <i>CRLF3</i> sequence conservation, developmental expression, and downstream signaling.	83
Figure 3.8   Impaired RhoA signaling drives <i>CRLF3</i> -mediated neuronal defects.	86
 <b>Chapter 4</b>	
Figure 4.1   Experimental conclusions from Chapter 2.	103
Figure 4.2   Experimental conclusions from Chapter 3.	106
Figure 4.3   Analysis of RAS downstream effectors in TGD hiPSC-hCOs.	109
Figure 4.4   Neurofibromin domains and putative binding partners.	112
Figure 4.5   hCO neuronal subtype specification and functional maturation.	115

# List of Tables

## **Chapter 2**

Table 2.1 | Primary antibodies. 44

Table 2.2 | Inter-clone analysis of control and *NF1*-mutant hiPSC-derived cells and organoids. 45

## **Chapter 3**

Table 3.1 | Patient-derived CTL1-3, TGD1-3 and aTGD (atypical TGD) hiPSC lines and isogenic hiPSC lines CRISPR/Cas9-engineered to harbor NF1 patient *NF1* gene mutations. 88

Table 3.2 | Human genomic DNA whole-exome sequencing. 89

Table 3.3 | Differentially expressed gene list filtered for non-significant genes in the comparison of TGD vs sh*CRLF3* samples. 90

Table 3.4 | Summary of experimental samples, replicates and statistical tests used. 91

Table 3.5 | Key resources table. 92



# **Acknowledgments**

This work was supported by the MSTP Training Grant and a Young Investigator Award from the Children's Tumor Foundation.

First, I would like to thank my advisor, Dr. David H. Gutmann, for his commitment to my training over the past four years. Dr. Gutmann's effusive enthusiasm for scientific investigation and dedication to translating those discoveries for patients has instilled in me the importance of prioritizing the big picture in research. Dr. Gutmann has invested innumerable hours helping me grapple with models, difficult questions, experimental design, and outcomes. His feedback and encouragement have been instrumental in shaping the way I navigate roadblocks and think about science. It has been a privilege and an honor to work with such a dedicated physician scientist and mentor. I am looking forward to our continued collaboration as I navigate the clerkship phase of the medical scientist training program and beyond.

Thank you to all the patients and families who motivate and support NF research. The privilege of meeting and sharing my research with you was one of the most meaningful experiences of my Ph.D. A special thank you to the Walk family. Your tireless efforts to raise funds and awareness in support of our research inspired and motivated me daily.

Thank you to my committee: Dr. Aaron DiAntonio, Dr. Kristen Kroll, Dr. Lilianna Solnica-Krezel, and Dr. Andrew Yoo. Their critiques, suggestions, and challenging questions were crucial to my growth as a scientist and to the evolution of this project. I would especially like to

thank Dr. DiAntonio, who delivered the life-changing news that I was being offered a position in the Washington University MSTP 6 years ago, and who also chaired my thesis committee. I am incredibly grateful for the privilege of having such an amazing committee, and I look forward to both staying in touch and future collaborations.

I would like to thank all the members of the Gutmann Laboratory, both past and present. They are an extraordinary group of scientists and physicians. Their passion and ingenuity inspired me daily. Their support and friendship helped me through many difficult times, as did their phenomenal desserts. A special thanks to Dr. Corina Anastasaki, who spearheaded the human induced pluripotent stem cell initiative in the Gutmann Lab. She was instrumental to my training. Thank you for your guidance, encouragement, and friendship.

I would like to thank the Genome Engineering and iPSC Center (GEiC), specifically Amber Neilson and Dr. Yi-Hsien Chen, for responding to the multitude of questions and reprogramming requests that I initiated. A special thank you to Jennifer Traber, who worked tirelessly to acquire patient samples that enabled the scientific discoveries in this dissertation.

In addition, I would like to thank my previous mentors, as I was afforded the privilege of joining the Washington University MSTP because of their training and belief in me. I would first like to thank Dr. Steven Johnson for helping me realize my passion for research as an undergraduate student. I am so grateful for the time and energy Dr. Johnson invested in my training. I would like to thank Dr. Brenda Wilson for her career guidance and for allowing me to conduct my undergraduate thesis in her lab. I would also like to thank Dr. Maciej Lesniak for allowing me to

join his laboratory during my gap year and work on the project of my choosing. Thank you to Dr. Yu Cheng, who trained me in Dr. Lesniak's Laboratory. Thank you to all the mentors with whom I did research rotations at Washington University. A special thanks to Dr. Shelly Sakiyama-Elbert for her invaluable career advice and mentorship.

Thank you to my friends and family for your steadfast support. Finally, I would like to thank my amazing husband, Matan. I could not ask for a more supportive, selfless, and inspiring partner. Thank you for your encouragement and patience.

Michelle L. Wegscheid

*Washington University in St. Louis*

*May 2022*

## ABSTRACT OF THE DISSERTATION

Genetic risk factors for neurodevelopmental disorders: insights from hiPSC-cerebral organoids

by

Michelle L. Wegscheid

Doctor of Philosophy in Biology and Biomedical Sciences

Neurosciences

Washington University in St. Louis, 2022

Professor David H. Gutmann, Chair

Professor Aaron DiAntonio, Co-Chair

Neurofibromatosis type 1 (NF1) is a common neurodevelopmental disorder (NDD) characterized by remarkable phenotypic variability, where affected children manifest a spectrum of central nervous system (CNS) abnormalities, including brain tumors, impairments in attention, behavior, learning disabilities, and an increased incidence of autism spectrum disorder (ASD). A significant barrier to the implementation of precision medicine strategies for children with NF1 is a lack of prognostic risk factors to guide clinical management. However, emerging population-based genotype-phenotype association studies have suggested that the germline *NF1* gene mutation may represent one clinically actionable risk factor for NF1-associated neurodevelopmental abnormalities. As a critical step in interpreting the significance of these reported genotype-phenotype correlations, we sought to determine whether germline *NF1* gene mutations differentially affected human brain development, while controlling for other important confounding factors (*e.g.*, sex, genomic differences). For these studies, we generated an isogenic series of CRISPR/Cas9-engineered human induced pluripotent stem cells (hiPSCs) harboring

seven different intragenic NF1 patient germline *NF1* gene mutations. Using this experimental platform, we established 2D neural progenitor cell (NPC) and astrocyte cultures, as well as three-dimensional (3D) human cerebral organoids (hCOs). While all mutations similarly increased proliferation and RAS activity in 2D NPCs and astrocytes, we observed striking differences between *NF1* mutations on 2D NPC dopamine levels and 3D NPC proliferation, apoptosis, and neuronal differentiation in developing hCOs. Importantly, identical abnormalities were observed using patient-derived hiPSC 2D and 3D cultures bearing the same *NF1* gene mutations, thus establishing differential effects of the germline *NF1* gene mutation on human brain development. Based on these findings, we next sought to determine the cellular and molecular etiologies that underlie the severe developmental delays and intellectual disability (IQ < 70) seen in children with a specific type of *NF1* mutation involving heterozygous deletion of the *NF1* gene and several contiguous genes (*NF1*-total gene deletion [*NF1*-TGD]). Using hCOs from three NF1 patients harboring *NF1*-TGDs, we identified both neural stem cell (NSC) proliferation and neuronal maturation abnormalities in *NF1*-TGD hCOs. While increased NSC proliferation resulted from decreased *NF1*/RAS regulation, the neuronal differentiation, survival, and maturation defects were caused by reduced cytokine receptor-like factor 3 (*CRLF3*) expression and impaired RhoA signaling. Furthermore, we demonstrated a higher autistic trait burden in NF1 patients harboring a deleterious germline mutation in the *CRLF3* gene (c.1166T>C, p.Leu389Pro). Taken together, this body of work conceptually advances the field by (1) demonstrating differential effects of *NF1* mutations at the cellular and tissue levels in humans, establishing that the germline *NF1* gene mutation is one important factor that underlies clinical variability in this monogenic syndrome, and (2) revealing a new causative gene within the *NF1*-TGD locus responsible for hCO neuronal abnormalities and autism in children with NF1.

# **Chapter 1: Introduction & Perspective**

## 1.1 Preface

**Parts of this chapter are adapted from the following manuscript:**

**Wegscheid, M.L.**, Anastasaki, C. & Gutmann, D.H. Human stem cell modeling in neurofibromatosis type 1 (NF1). *Experimental Neurology* **299**, 270-280 (2018).

**Author contributions for the citation above:**

M.L.W. and D.H.G. wrote the paper. M.L.W. and C.A. made the figures.

## 1.2 Barriers to precision medicine

Precision medicine is an emerging healthcare strategy with profound potential to improve disease prevention, management, and treatment for patients. In contrast to the paradigm of care standardization, in which the same intervention is administered to all patients with a given condition based on disease-specific guidelines (also known as a “one size fits all” approach), a precision medicine approach is one in which disease prevention, prognostic predictions, management strategies and treatment options are precisely and accurately informed by a series of factors (*e.g.*, genes, epigenetic modifications, environmental influences) for each patient (**Figure 1.1**). As such, precision medicine is heavily reliant on the identification of key determinants that account for variability in pathophysiology, clinical presentation, and response to treatment among individuals with the same disease. An incomplete understanding of the factors underlying disease variability is one of the most significant barriers to the actualization of precision medicine for patients.

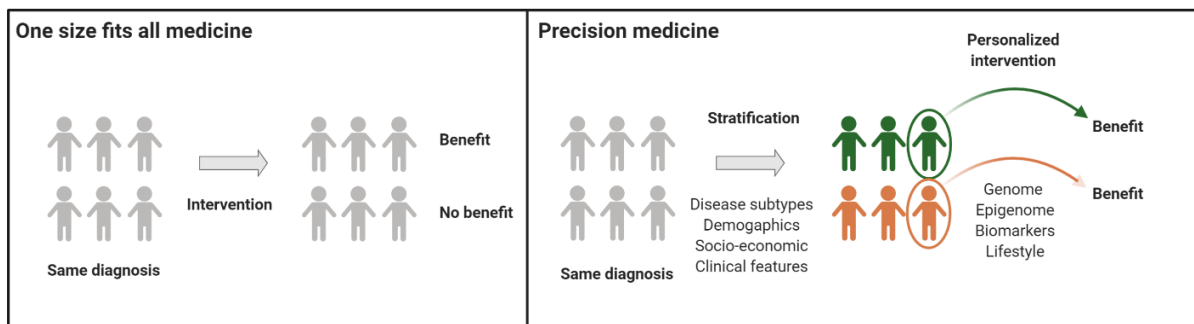


**Figure 1.1 | Precision medicine.** Precision medicine leverages patient-specific parameters (*e.g.*, genes, epigenome, environmental influences) to design and deliver the most appropriate intervention strategy for each patient, thereby optimizing patient benefit.



## 1.3 Clinical heterogeneity in Neurofibromatosis type 1

### (NF1)

This challenge is exemplified by Neurofibromatosis type 1 (NF1), a common, monogenic neurodevelopmental disorder characterized by extreme phenotypic variability. While all individuals with NF1 harbor a single mutation in one copy of the *NF1* gene located on chromosome 17q11.2 (Uusitalo et al., 2014), patients present with a wide range of clinical manifestations, including pigmentary abnormalities (café-au-lait macules, skinfold freckling, Lisch nodules), peripheral (neurofibromas, malignant peripheral nerve sheath tumors) and central (optic pathway and brainstem gliomas) nervous system tumors, bone abnormalities, vasculopathy and other cancers (Jett and Friedman, 2010). In addition to these medical problems, as many as 80% of children with NF1 manifest cognitive abnormalities related to learning disabilities (60%) (Hyman et al., 2006), motor delays (50%) (Soucy et al., 2015), social perception deficits (autism spectrum disorder; 15-30%) (Morris et al., 2016a), attention deficits (60%) (Hyman et al., 2005), and, in some cases, severe intellectual disability (Venturin et al., 2004). While there has been enormous progress since the identification of the *NF1* gene in 1990, it is still not possible to identify those children who are most likely to develop specific medical problems, to predict the clinical course of their disease, or to anticipate their responses to rationally chosen medical treatments.

## 1.4 Germline *NF1* gene mutations

One of many potential factors underlying the immense clinical heterogeneity in NF1 could be the specific *NF1* germline gene mutation that an individual is born with. Over 1,000 different pathogenic intragenic variants (*e.g.*, frameshift, missense, nonsense, splice site) throughout the *NF1* gene have been reported in this patient population (ClinVar, Gene ID: 4763, coding sequence length: 8,520 nucleotides). This large number of mutations, coupled with the lack of spatial clustering, has led to the widely accepted assumption that all mutations are functionally equivalent and have no bearing on clinical expression. However, this notion has been challenged by several population-based studies, which demonstrated differences in the effects of germline *NF1* gene mutations on clinical symptomatology. For instance, patients harboring the c.2970-2971\_delAAT, c.5425C>T and c.3112A>G *NF1* germline mutations do not develop dermal and plexiform neurofibromas, the signature peripheral nervous system tumors in NF1 (Pinna et al., 2015; Trevisson et al., 2019; Upadhyaya et al., 2007). Conversely, children with large *NF1* locus microdeletions and missense mutations involving amino acids 844-848 exhibit more severe clinical manifestations (Koczkowska et al., 2018b; Mautner et al., 2010). A strong intra-familial concordance in autism spectrum symptomatology between family members sharing the same *NF1* gene mutation has been reported (Morris et al., 2016a), implicating the *NF1* gene mutation as an important factor in determining NF1-associated autism spectrum disorder (ASD). In addition, children with NF1-associated optic pathway gliomas were more likely to harbor 5' *NF1* gene mutations (Anastasaki et al., 2017; Sharif et al., 2011), while individuals with 3' *NF1* gene mutations had increased autistic trait burden (Morris and Gutmann, 2018).

## 1.5 Personalized preclinical models

While these correlations underscore the potential importance of the germline mutation as a predictive risk factor for NF1-associated symptomatology, they do not establish differential effects of *NF1* mutations at the molecular, cellular and tissue levels. Until recently, NF1 preclinical models exclusively employed knockout strategies, either by engineering a single “knockout” allele (neomycin cassette insertion into the RAS-GAP domain) or conditionally inactivating the *Nf1* gene using Cre-Lox recombination. As these mutations are not representative of the mutations found in patients with NF1, increasing efforts are being made to employ personalized murine models harboring patient specific *Nf1* gene mutations (Guo et al., 2019; Li et al., 2016; Toonen et al., 2016). In these early phase studies, germline *Nf1* gene mutations differentially dictated optic glioma (Toonen et al., 2016) and neurofibroma (Li et al., 2016) formation, and had different effects on *NF1* protein (neurofibromin) expression (Anastasaki et al., 2015).

Authenticated preclinical animal models are valuable experimental platforms to define the factors that underlie NF1-associated disease pathogenesis and progression. However, it will be critical to complement these models with preclinical platforms using human cells and tissues. While rodents and humans share substantial genomic homology (an average of 85% sequence conservation for protein-coding genes) (Makalowski et al., 1996), there are inherent species-specific differences to consider when using animal models to inform about human disorders. Anatomically, rodent brains are unlike human brains in that they are lissencephalic, meaning that their cerebral cortices do not undergo gyrification during development like their human

counterparts (Semple et al., 2013). In addition, cerebral progenitor zone complexity and organization differs between rodents and humans (Molnar et al., 2011). Furthermore, specific cell types, like microglia, exhibit striking interspecies differences in proliferation, immune system receptor expression and response to immune stimuli *in vitro* (Smith and Dragunow, 2014).

For these reasons, it would be desirable to complement studies using personalized preclinical mouse models with human biospecimens. Unfortunately, for CNS clinical phenotypes, human brain biospecimens are exceedingly rare. Optic pathway gliomas (OPGs) in children with NF1 are almost never biopsied as part of routine medical care (Jett and Friedman, 2010). On the rare occasion that these tumors are biopsied, patient-derived xenografts (PDX), in which patient tumor tissues are implanted into immunodeficient mice, could allow for preservation of tumor histology, genetic composition, and drug sensitivity. This platform has been highly successful for high-grade brain tumors, such as glioblastoma (Joo et al., 2013), but has been problematic for low-grade gliomas due to premature senescence and low clonogenic frequencies. Another approach employs pathologic specimens, which maintain intact tissue architecture and gene expression patterns. However, the dynamic changes inherent in these tissues are reduced to a static image, and much of the information in these biospecimens regarding cell-cell interactions, stromal contributions, or the impact of germline genetics on disease development and progression is lost.

## 1.6 Human induced pluripotent stem cells (hiPSCs)

These limitations support the use of an *in vitro* human system amenable to genetic engineering, as well as dynamic molecular and functional analyses. The discovery of somatic cell reprogramming to a pluripotent state by Shinya Takahashi and colleagues in 2006 (Takahashi and Yamanaka, 2006) ushered in an era of *in vitro* human disease modeling. The work that Dr. Yamanaka received the Nobel Prize for in 2012 involved retroviral delivery of transcription factors Oct3/4, Sox2, c-Myc and Klf4 into mouse embryonic fibroblasts, generating induced pluripotent stem cells (iPSCs) with the capacity to differentiate into any cell type in the body (Takahashi and Yamanaka, 2006). Over the last ten years, refinements in reprogramming and differentiation techniques have resulted in the generation and application of human-derived iPSCs (hiPSCs) (Takahashi et al., 2007) to model complex genetic disorders, such as Rett syndrome (Marchetto et al., 2010), Fragile X syndrome (Mor-Shaked and Eiges, 2016), schizophrenia (Brennan et al., 2011), and bipolar disorder (Chen et al., 2014). The ability to engineer hiPSCs with patient-specific mutations and differentiate them into virtually any cell type renders the hiPSC platform a powerful technology to dissect the contributions of germline genetics to disease pathogenesis in NF1 (**Figure 1.2**).

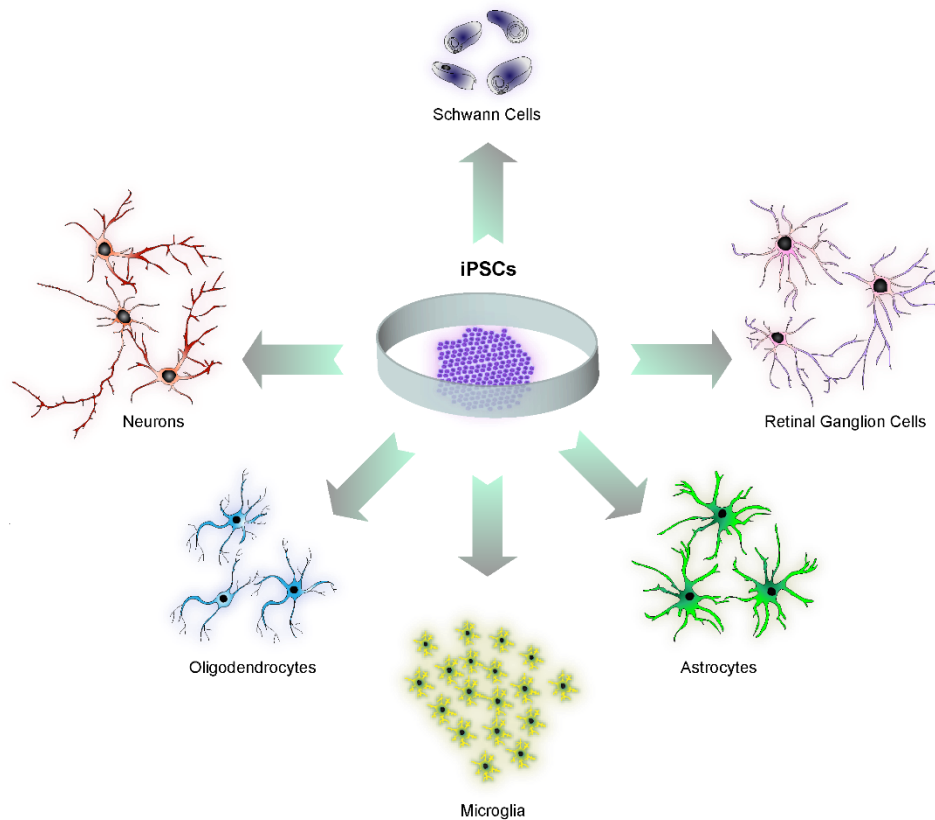


**Figure 1.2 | hiPSCs for disease modeling in NF1.** hiPSCs can be efficiently differentiated into cell types affected in NF1 using appropriate growth factors, cytokines, and extracellular matrix molecules.

## 1.7 Human iPSC-derived cerebral organoids (hCOs)

Cultures of homogenous human-derived cell populations are extremely useful for evaluating cell-specific molecular signaling pathways in disease, but these two-dimensional (2D) cultures do not permit a detailed examination of heterogeneous cell-cell interactions, patterning, and circuit abnormalities seen in the brains of patients with neurodevelopmental disorders. For this reason, three-dimensional (3D) culture systems have been developed to support the evolution of

complex, self-organizing cerebral tissues. These 3D structures, termed human cerebral organoids (hCOs), can be established from patient-derived iPSCs, and replicate many aspects of the cellular diversity, connectivity, and regional identity found in the developing human brain (Huch and Koo, 2015; Lancaster and Knoblich, 2014; Quadrato et al., 2016).

The first cerebral organoids were generated to model microcephaly (Lancaster et al., 2013), where skin fibroblasts from a patient with truncating *CDK5RAP2* mutations were reprogrammed using lentiviral *OCT4*, *SOX2*, *MYC* and *KLF4* delivery. Reverse transcriptase PCR (RT-PCR) and immunohistochemistry confirmed the presence of cell types from discrete brain regions, including midbrain, hindbrain, forebrain and hippocampal structures within the tissues, as well as the sophisticated organization of dorsal cortical regions. Moreover, the organoids derived from these patient iPSCs had premature neural differentiation and failure of radial glial stem cell expansion, demonstrating their ability to serve as an *in vitro* model of a human neurodevelopmental disorder which had been difficult to recapitulate in mice (Lancaster et al., 2013). Cerebral organoids have since been leveraged as experimentally tractable platforms to study the mechanisms underlying several other neurodevelopmental disorders (*e.g.*, ASD, lissencephaly, Zika virus-induced microcephaly) (Bershteyn et al., 2017; Mariani et al., 2015; Qian et al., 2016a). Based on these successes, 3D cerebral organoid cultures represent a promising platform for dissecting the complex interplay between different cell types relevant to disease pathogenesis and progression for specific NF1 clinical features.

## 1.8 Directions

In this introduction, we highlight the pressing need to identify key determinants underlying disease variability as a critical step towards actualizing precision medicine. This challenge is exemplified by NF1, a monogenic disorder characterized by immense clinical heterogeneity.

**Based on emerging genotype-phenotype association studies in NF1, we hypothesized that the germline *NF1* gene mutation may represent one clinically actionable risk factor for NF1-associated symptomatology.** The studies described in this dissertation aim to critically evaluate this hypothesis. For these studies, we generated a collection of isogenic and patient-derived hiPSCs harboring NF1 patient *NF1* gene mutations. Leveraging this hiPSC resource, we pioneered an hiPSC-derived cerebral organoid platform (**Figure 1.3**) to investigate the effects of different *NF1* mutations on human brain development.



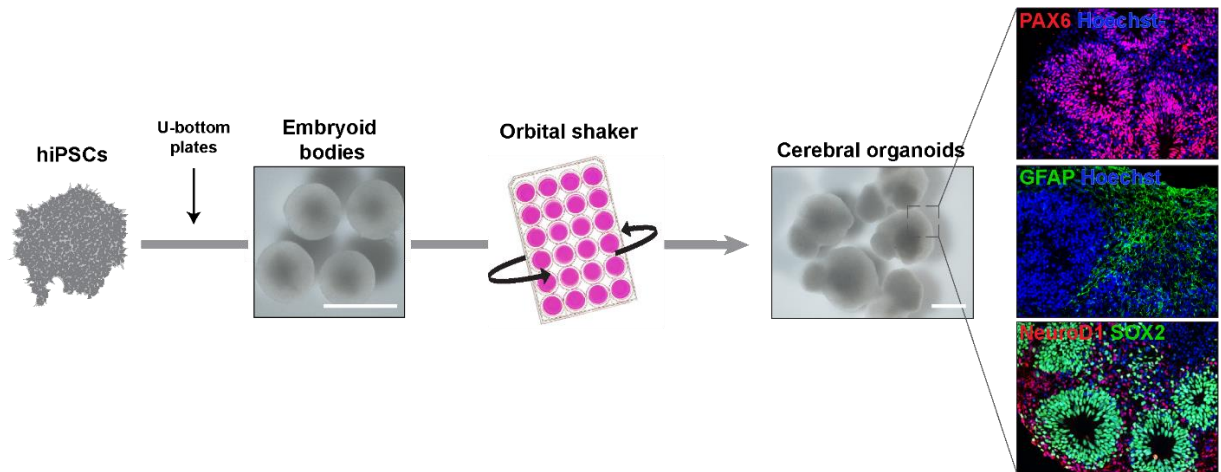


**Figure 1.3 | Cerebral organoid cultures.** hiPSCs are aggregated to allow for deposition of matrix and the formation of embryoid bodies. The generation of cerebral organoids involves neural induction in stationary culture. After expansion of the resulting neuroepithelium, samples are transferred to a rotating suspension culture to promote nutrient diffusion and further organoid maturation. hCOs are subsequently collected for molecular and cellular analyses. Representative hCOs generate PAX6<sup>+</sup> neural progenitor cells (NPCs), GFAP<sup>+</sup> astrocytes, and NeuroD1<sup>+</sup> neurons. Scale bars: 50  $\mu$ m.

**First**, we analyzed an isogenic series of CRISPR/Cas9-engineered hiPSCs harboring seven different intragenic *NF1* patient germline *NF1* gene mutations, as well as patient-derived hiPSCs bearing the same mutations (**Figure 1.4**). Importantly, unlike prior studies, the use of an isogenic series of hiPSCs eliminates other contributing factors, like sex and genomic variation (potential modifier genes) and permits a direct examination of the effects of different *NF1* gene mutations. We evaluated the effects of these different *NF1* gene mutations on hiPSC-derived 2D neural

progenitor cell (NPC) and astrocyte cultures, as well as 3D hCOs. This analysis is depicted in Chapter 2.

**Second**, we sought to understand the molecular and cellular etiologies underlying severe developmental delays and intellectual disability seen in children with a microdeletion on chromosome 17q11.2, involving the *NF1* gene and flanking regions (1.4 Mb *NF1*-total gene deletion; *NF1*-TGD). For these studies, we analyzed hCOs derived from three neurologically normal control individuals and three individuals harboring a 1.4 Mb *NF1*-TGD. The results of experiments leveraging 17q11.2 microdeletion hCOs harboring a total heterozygous *NF1* gene deletion are instructive for interpreting findings in hCOs harboring intragenic *NF1* mutations, as well as in the identification other important genes contained within the *NF1*-TGD locus that could contribute to specific clinical phenotypes. This analysis is depicted in Chapter 3.

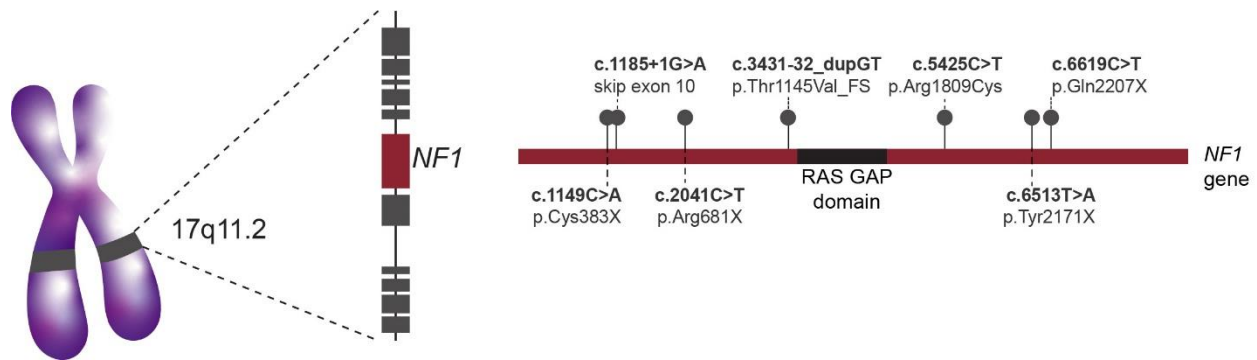


**Figure 1.4 | Schematic diagram showing the chromosomal region 17q11.2.** The *NF1* gene containing seven engineered *NF1* patient *NF1* gene mutations is indicated in red. The location of the RAS-GAP domain is highlighted in black.

**Chapter 2: Isogenic hiPSC-derived CNS cells  
and hCOs establish differential effects of *NF1*  
gene mutations**

## 2.1 Preface

**This chapter is adapted from the following manuscript:**

Anastasaki, C.\*, **Wegscheid, M.L.\***, *et al.* Human iPSC-derived Neurons and Cerebral Organoids Establish Differential Effects of *NF1* Gene Mutations. *Stem Cell Reports* **14**, 541-550 (2020). **\*co-first authors**

**Author contributions for the citation above:**

C.A., M.L.W., and D.H.G. designed and analyzed the experiments. C.A., M.L.W., K.H., J.B.P., N.D.K., J.C., O.C., and J.D.D. conducted and/or interpreted the experiments. The manuscript was assembled by C.A., M.L.W. and D.H.G.

## 2.2 Abstract

Neurofibromatosis type 1 (NF1) is a common neurodevelopmental disorder caused by a spectrum of distinct germline *NF1* gene mutations, traditionally viewed as equivalent loss-of-function alleles. To specifically address the issue of mutational equivalency in a disease with considerable clinical heterogeneity, we engineered seven isogenic human induced pluripotent stem cell lines, each with a different NF1 patient *NF1* mutation, to identify potential differential effects of *NF1* mutations on human central nervous system cells and tissues. While all mutations increased proliferation and RAS activity in two-dimensional (2D) neural progenitor cells (NPCs) and astrocytes, we observed striking differences between *NF1* mutations on 2D NPC dopamine levels, and 3D NPC proliferation, apoptosis, and neuronal differentiation in developing cerebral organoids. Together, these findings demonstrate differential effects of *NF1* gene mutations at the cellular and tissue levels, suggesting that the germline *NF1* gene mutation is one factor that underlies clinical variability.

## 2.3 Introduction

Cognitive impairments in individuals with NF1 are characterized by extensive variability, ranging from brain tumors and motor delays to learning difficulties, attention deficits and autism (Fisher et al., 2018; Hyman et al., 2006; Jett and Friedman, 2010; Korf, 2013; Morris and Gutmann, 2018). One of many potential factors underlying this clinical variability could be the specific *NF1* germline mutation, a notion suggested by population-based studies (Anastasaki et al., 2017; Bolcekova et al., 2013; Kehrer-Sawatzki et al., 2017; Koczkowska et al., 2018a; Pinna

et al., 2015; Rojnueangnit et al., 2015; Sharif et al., 2011; Trevisson et al., 2019; Upadhyaya et al., 2007). For example, patients harboring the c.2970-2971\_delAAT, c.5425C>T and c.3112A>G *NF1* germline mutations lack dermal and plexiform neurofibromas, the signature peripheral nervous system tumors in NF1 (Pinna et al., 2015; Trevisson et al., 2019; Upadhyaya et al., 2007).

While these studies raise the possibility that not all *NF1* gene mutations are functionally equivalent, they do not establish differential effects of *NF1* patient germline mutations at the cellular or tissue levels, a critical step in interpreting the significance of reported genotype-phenotype associations. To specifically evaluate differential *NF1* mutation effects on human CNS cells and tissues, while controlling for important confounding factors (*e.g.*, sex, genomic differences), we generated an isogenic series of human induced pluripotent stem cells (hiPSCs) harboring seven representative NF1-patient *NF1* mutations.

## 2.4 Materials and methods

### *Human iPSCs, hiPSC-derived CNS cells and hCOs*

Seven distinct NF1-patient germline *NF1* gene mutations (Transcript ID NM\_000267; c.1149C>A, c.1185+1G>A, c.2041C>T, c.3431-32\_dupGT, c.5425C>T, c.6513T>A, c.6619C>T) were individually engineered using CRISPR/Cas9 technology into a single commercially available male control human iPSC line (BJFF.6) by the Washington University Genome Engineering and iPSC Core Facility (GEiC). Heterozygous mutations were confirmed by next-generation sequencing (NGS) sequencing (Bell et al., 2014), and two different clones

were expanded for each of the six *NF1*-mutant and the control lines (**Figure 2.1A-C**). Only a single clone heterozygous for the c.6619C>T *NF1* mutation could be generated without any additional genomic insertions or deletions. Retention of heterozygosity in the hiPSCs was confirmed by sequencing after five passages, as well as in all derivative cell lines by RAS activity assays. Similar results were obtained after each passage. Additionally, iPSCs reprogrammed from the fibroblasts of three NF1 patients (c.1185+1G>A; c.5425C>T; c.6513T>A) and one control subject (Anastasaki et al., 2015) were employed for subsequent analyses. For NPC differentiation, hiPSCs were passaged onto PLO/Laminin (Millipore Sigma)-coated plates using ReLeSR (STEMCELL Technologies) and seeded at 200,000 cells/cm<sup>2</sup> in NPC induction medium (50% DMEM F12 [Gibco], 50% Neurobasal medium [Gibco], supplemented with N2, B27 [Fisher], 2mM GlutaMax [Gibco], 10ng/mL hLIF, 4μM CHIR99021, 3μM SB431541, and 0.1μM Compound E [all from STEMCELL Technologies]). Cells were maintained in this medium supplemented with 2μM Dorsomorphin for 3 days and without Dorsomorphin (STEMCELL technologies) for an additional 5 days. NPCs were subsequently incubated in NPC maturation medium (50% DMEM/F12, 50% Neurobasal medium supplemented with N2, B27, 2mM GlutaMax, 10ng/mL hLIF, 3μM CHIR99021 and 2μM SB431541), and were passaged weekly following Accutase (STEMCELL Technologies) dissociation according to manufacturer's instructions. NPCs were treated for 24 hours with 10μg/μL fibroblast growth factor (FGF) or brain-derived neurotrophic factor (BDNF; both STEMCELL Technologies) to assess growth factor-induced cell proliferation. GABAergic neurons were differentiated as previously described (Liu et al., 2013). For astrocytic differentiation, NPCs were plated on Primaria-coated plates in Astrocyte Growth Media (ScienCell) for a minimum of two weeks and a maximum of ten passages (Tcw et al., 2017).

Cerebral organoids were generated as previously described (Lancaster and Knoblich, 2014) with modifications: Embryoid bodies (EBs) were cultured in NIM (STEMCELL Technologies) supplemented with 20 $\mu$ M Rock inhibitor Y27632 (Millipore) and 4ng/mL bFGF (Peprotech) for the first 5 days, followed by NIM alone for an additional 4 days prior to direct transfer to cerebral organoid media without Matrigel embedding. Cerebral organoids were maintained for up to 56DIV. All experiments employed at least three biological replicates from two independently generated hiPSC clones.

### ***RNA extraction, cDNA production, qPCR and targeted allele expression analysis***

Total RNA was extracted from snap-frozen cell pellets of three independent passages of two clones per hiPSC line, using QIAGEN RNeasy Mini Kit. Total RNA was reverse-transcribed into cDNA using Applied Biosystems High-Capacity cDNA Reverse Transcription Kit per the manufacturer's instructions. Real-time quantitative PCR (qPCR) was performed using TaqMan Gene Expression assays *NFI* (Hs01035108\_m1) and *GAPDH* (Hs02786624\_g1; internal control), and relative *NFI* expression was calculated using the  $\Delta\Delta$ CT analysis method following manufacturer's instructions (ThermoFisher). For allele-specific expression analyses, primer pairs including Illumina adapter sequences concatenated to their 5' ends were used for all *NFI*-mutant hiPSCs to initially amplify the mutation-surrounding region, and later to add the P5 sites, P7 sites, and sample-specific index. The samples were pooled and the amplicons were deep-sequenced on a MiSeq machine. Illumina adapters, 5' and 3' bases with quality scores <25, as well as sequences <25 bases long were trimmed using the Trimmomatic v0.331 software. Trimmed reads were aligned to the human reference genome hg19 using STARv2.52 software and allele reads were calculated using Integrative Genomics Viewer v2.3.293.



### *Allele-Specific Analysis Primers Used*

The primers used for the first PCR reaction including the Illumina adaptor sequences were the following:

1149C>A FW:

GTGACTGGAGTTCAGACGTGTGCTCTTCCGATCTCTACTTGTTTCAGTCCATGGTGG

1149C>A REV:

ACACTCTTTCCCTACACGACGCTCTTCCGATCTCCAATGCGGAATTGGTGATGA

2041C>T FW:

GTGACTGGAGTTCAGACGTGTGCTCTTCCGATCTAATTACTACGTA CTCTGGAGC

2041C>T REV:

ACACTCTTTCCCTACACGACGCTCTTCCGATCTGCAAGAGGTTATGCACTGAC

3431-32\_dupGT FW:

GTGACTGGAGTTCAGACGTGTGCTCTTCCGATCTGACTGCAGTGAAGTTGA AGATG

3431-32\_dupGT REV:

ACACTCTTTCCCTACACGACGCTCTTCCGATCTGTAGCTCTTGTCTGGAGAT CC

5425C>T FW:

GTGACTGGAGTTCAGACGTGTGCTCTTCCGATCTGAAGCCATTGTCCAGTCTATC

5425C>T REV:

ACACTCTTTCCCTACACGACGCTCTTCCGATCTGGTACAAGTTAAGGCACACAG

6513T>A FW:

GTGACTGGAGTTCAGACGTGTGCTCTTCCGATCTGACTCAGTCTGACAGAGTTCTC

6513T>A REV:

ACACTCTTTCCCTACACGACGCTCTTCCGATCTCTAGTTCTGTCCACTGGTCC

6619C>T FW:

GTGACTGGAGTTCAGACGTGTGCTCTTCCGATCTTGCCTTCCGTTCCAGTTACC

6619C>T REV:

ACACTCTTTCCCTACACGACGCTCTTCCGATCTGAGCTCTTGGTTGCAGGGAT

The primers used for the second amplification PCR reaction which include the unique indexes employed to identify different sequencing products were the following:

Primer 1.0 FW:

AATGATACGGCGACCACCGAGATCTACACACTCTTTCCCTACACGACGCTCTTC  
CGATCT

Primer 1.0 SIC2 FW:

AATGATACGGCGACCACCGAGATCTACACAATGAAACACTCTTTCCCTACA  
CGACGCTCTTCCGATCT

Common REV: GTGACTGGAGTTCAGACGTGTGCTCTTCCGATCT

Index 1 REV: CAAGCAGAAGACGGCATAACGAGATAAATAGATGGTGACTGGAGTTC

Index 2 REV: CAAGCAGAAGACGGCATAACGAGATCAGAGGAGAGTGACTGGAGTTC

Index 3 REV: CAAGCAGAAGACGGCATAACGAGATCGTATAGATGTGACTGGAGTTC

Index 4 REV: CAAGCAGAAGACGGCATAACGAGATAAGGGCTCAGTGACTGGAGTTC

### ***Immunohistochemistry and ELISA Assays***

Immunocytochemistry on NPCs, astrocytes and neurons was performed following established protocols (Anastasaki et al., 2015) using the antibodies described (**Table 2.1**). RAS activity

(ThermoFisher), GABA, dopamine (both Rocky Mountain Diagnostics) detection (Anastasaki et al., 2015), BrdU proliferation assays (Roche) and direct cell counting were performed as previously described (Toonen et al., 2016). Immunohistochemistry on cryosections of cerebral organoids was performed as previously described (Sloan et al., 2018). A minimum of three independent samples representing different passages of two separate clones were employed for each line.

### ***Mice***

All animals were maintained on an inbred C57BL/6 background using a 12 h light–dark cycle with *ad libitum* access to food and water. Heterozygous *Nf1* mice were generated to harbor point mutations corresponding to the human c.1149C>A, c.2041C>T, c.3431\_32dupGT and c.5425C>T mutations. The c.1149C>A, c.2041C>T, and c.3431\_32dupGT mice were generated using C57BL/6 ES cells backcrossed a minimum of 10 times to wild-type C57BL/6 mice, while the c.5425C>T mice were generated by CRISPR/Cas9 engineering on a C57BL/6 genetic background and heterozygous mutation was confirmed by direct sequencing.

### ***Statistics***

All statistical tests were performed using GraphPad Prism 5 software. T-tests, one-way or two-way analysis of variance (ANOVA) with Dunnett or Bonferroni post-test correction was performed using GraphPad Prism 5 software. Statistical significance was set at  $P < 0.05$ .

### ***Next Generation RNA Sequencing and Analysis***

RNA was extracted from three independently generated samples of isogenic CTL or *NFI*-mutant (c.1185+1G>A; c.6513T>A) NPCs, and one sample each from the non-isogenic CTL and patient-derived *NFI*-mutant NPCs harboring the same *NFI* mutations. Samples were prepared according to library kit manufacturer's protocol, indexed, pooled, and sequenced on an Illumina HiSeq. Basecalls and demultiplexing were performed with Illumina's bcl2fastq software and a custom python demultiplexing program with a maximum of one mismatch in the indexing read. RNA-seq reads were then aligned to the Ensembl release 76 primary assembly with STAR version 2.5.1a. Gene counts were derived from the number of uniquely aligned unambiguous reads by Subread:featureCount version 1.4.6-p5. Isoform expressions of known Ensembl transcripts were estimated with Salmon version 0.8.2. Sequencing performance was assessed for the total number of aligned reads, total number of uniquely aligned reads, and features detected. The ribosomal fraction, known junction saturation, and read distribution over known gene models were quantified with RSeQC version 2.6.2. The raw gene count matrix was then imported into Partek Flow software, version 8.0. Normalization size factors were calculated for all gene counts by CPM to adjust for differences in sequencing depth. Ribosomal genes and genes not expressed in the smallest group size minus samples greater than one count-per-million were excluded from further analysis. Gene-specific analysis was then performed using the lognormal with shrinkage model (limma-trend method) to analyze for differential expression between the three groups of samples. Principle component analysis (PCA) was conducted in Partek Flow using normalized gene counts. The "grouping" is simply a post hoc highlighting of the genotypes for assistance in visualizing that the different samples clustered together by genotype during the principle component. For further visualization, a heatmap was generated

using the differential genes for each group filtered at p-values  $\leq 0.05$  and log fold-changes more extreme or equal to  $\pm 2$ . Features and samples were clustered using Pearson Correlation as a distance metric. The accession number for the deep sequencing data reported in this paper is GEO: GSE144601.

## 2.5 Results

### Generation of isogenic *NF1*-mutant hiPSCs

The seven *NF1* pathogenic mutations, derived from patients in our clinical population at Washington University/ St. Louis Children's Hospital, represent the spectrum of mutations typically seen in individuals with NF1. In this regard, the selected mutations were interspersed throughout the *NF1* protein (neurofibromin) coding sequence, were both proximal and distal to the well-characterized RAS GTPase activating protein (RAS-GAP) domain (GRD), and included four nonsense (c.1149C>A, c.2041C>T, c.6513T>A, c.6619C>T), one splice site (c.1185+1G>A), one missense (c.5425C>T) and one frameshift (c.3431-32\_dupGT) mutation (**Figure 2.1, 2.2, 2.3A**). All the engineered isogenic hiPSCs harbored only a single *NF1* mutation ("*NF1*-mutant"), retained expression of the remaining wild-type *NF1* allele as confirmed by DNA and RNA sequencing (**Figure 2.1D**), and expressed similar levels of *NF1* mRNA (**Figure 2.3B**). For all hiPSC lines with two clones, identical results were obtained using numerous independently generated biological replicates, as well as with three NF1 patient-derived hiPSC lines generated from somatic cells (fibroblasts; **Figure 2.4, Table 2.2**).

## **Isogenic *NF1*-mutant hiPSC-derived NPCs and astroglia have increased RAS activity and proliferation**

To determine the consequences of the different *NF1* gene mutations on neurofibromin signal transduction and function in human CNS cells, *NF1*-mutant and control hiPSCs were first differentiated into neural progenitor cells (NPCs) capable of generating both neurons (TUJ1<sup>+</sup> cells) and glia (S100β<sup>+</sup> cells) (**Figure 2.2**). Since neurofibromin primarily functions as a RAS-GAP to control cell proliferation, we initially assessed RAS activity. Consistent with this negative RAS regulatory property, all *NF1*-mutant NPCs exhibited a comparable 1.8-2.2-fold increase in RAS-GTP relative to the isogenic control (**Figure 2.3C**). Importantly, the addition of growth factors (FGF or BDNF) did not further increase RAS activity in the *NF1*-mutant lines but resulted in greater RAS-GTP levels in the control lines, equivalent to the levels observed in the unstimulated *NF1*-mutant lines (**Figure 2.3D-E**). These findings demonstrate that a heterozygous *NF1* mutation phenocopies the effect of exogenous growth factor stimulation on RAS activation. Additionally, all *NF1*-mutant NPCs exhibited increased cell division, as evidenced by elevated BrdU incorporation (2.6-3.2-fold increase; **Figure 2.3F**) and total cell number (1.9-2-fold increase; **Figure 2.3G**). To evaluate the effects of distinct *NF1* gene mutations on the production of NPCs in a three-dimensional (3D) model of human brain development, we generated cerebral organoids from the control and *NF1*-mutant hiPSC lines. Despite repeated efforts, we were unable to derive organoids from two of the seven *NF1*-mutant hiPSC lines (c.2041C>T and c.6513T>A), but successfully generated organoids from the control and five of the seven *NF1*-mutant hiPSC lines (c.1149C>A, c.1185+1G>A, c.3431-32\_dupGT, c.5425C>T, c.6619C>T; **Figure 2.3H**). The organoids formed radially organized ventricle-like structures populated by SOX2<sup>+</sup> NPCs by 16 days *in vitro* (DIV). Similar to the 2D cultures, all *NF1*-mutant organoids

exhibited a 2.8-3.2-fold increase in RAS activity (**Figure 2.3I**), as well as a 1.6-2.2-fold increase in total NPCs per ventricular zone at 16DIV (**Figure 2.3J**).

Next, we sought to determine whether these heterozygous *NFI* mutational effects were observed in another proliferating CNS cell type by differentiating the NPCs into astrocytes (**Figure 2.5A**). Similar to the NPCs, *NFI*-mutant astrocytes exhibited 2-2.3-fold elevated RAS activity (**Figure 2.5B**), 2.3-2.7-fold increased cell division (**Figure 2.5C**) and 2.1-2.5-fold greater total cell number (**Figure 2.5D**) relative to the control line. Consistent with the 2D astrocytes, 56DIV *NFI*-mutant organoids had more EAAT1- and GFAP-expressing cells (astrocytes) (**Figure 2.5E**) compared to control organoids. Importantly, isogenic *NFI*-mutant NPCs and organoids were similar to those of their respective patient-derived NPCs (c.1185+1G>A; c.5425C>T; c.6513T>A) and organoids (c.1185+1G>A; c.5425C>T) (**Figure 2.4, 2.6, Table 2.2**) in RAS activity and NPC proliferation, as well as to whole brain lysates from genetically engineered mice (GEM) harboring the analogous germline *Nfi* gene mutations (c.1149C>A, c.2041C>T, c.3431-32\_dupGT, and c.5425C>T; **Figure 2.7A**). Taken together, these data illustrate that all heterozygous *NFI* mutations increase RAS activity and RAS-regulated cell proliferation in both human and murine CNS cells.

### **hiPSC-derived *NFI*-mutant neurons exhibit both shared and differential deficits in 2D cultures**

As many children with NF1 exhibit cognitive deficits and neurodevelopmental delays (Hyman et al., 2006; Hyman et al., 2005; Jett and Friedman, 2010; Morris and Gutmann, 2018), we sought to determine the effects of distinct *NFI* germline mutations on human CNS neuronal function

and differentiation. Based on the observation that *Nf1*-mutant (*Nf1*<sup>+/-</sup>) mice exhibit elevated GABA-ergic tone that contributes to the observed deficits in learning and spatial memory (Costa et al., 2002; Cui et al., 2008), we assayed GABA levels in NPC-derived GABAergic neurons (**Figure 2.7B, 2.4E**). In all *NF1*-mutant neurons (2D cultures), GABA levels were increased (6.5-7.8-fold) relative to isogenic control neurons, revealing a shared abnormality in all *NF1*-mutant GABAergic neurons.

In contrast, *NF1*-mutant NPCs in 2D cultures displayed striking differences in dopamine (DA; **Figure 2.7C**) levels. DA levels were reduced by >70% in the c.1149C>A, c.2041C>T and c.6619C>T *NF1* mutants, but by <40% in the c.1185+1G>A, c.3431-32\_dupGT, c.5425C>T and c.6513T>A *NF1* mutants relative to the control line. These differential effects mirror findings using patient-derived NPCs (**Figure 2.4F, Table 2.2**) (Anastasaki et al., 2015), as well as mice engineered with *NF1* patient-specific *Nf1* germline mutations (**Figure 2.7D**) (Toonen et al., 2016). Taken together, these findings demonstrate the existence of differential effects of *NF1* germline mutations on neuronal differentiation *in vitro*.

### **Differential effects of *NF1* mutations on cerebral organoid NPC proliferation, apoptosis, and differentiation**

To further explore the differential effects of *NF1* mutations in the developing human brain, we used the more contextually relevant cerebral organoid platform (see Section 2.4: Methods and Materials). Examination of NPC proliferation, apoptosis, and neuronal differentiation in 16DIV cerebral organoids revealed two distinct groups of *NF1* mutants (**Figure 2.8**): Group 1 (c.1185+1G>A; c.5425C>T; c.6619C>T) *NF1* mutants exhibited increased NPC proliferation



(1.3-1.4-fold) and apoptosis (2-3-fold), but had similar numbers of early (NeuroD1<sup>+</sup>, TUJ1<sup>+</sup>) and late (MAP2<sup>+</sup>) immature neurons relative to controls. In this manner, Group 1 *NFI* mutations increased both proliferation and apoptosis during NPC differentiation, allowing neurogenesis to proceed normally. In contrast, Group 2 (c.1149C>A; c.3431-32\_dupGT) *NFI*-mutant organoids had normal NPC proliferation, but reduced NPC apoptosis (70-92% reduction) and very few immature neurons relative to the isogenic controls (73-84% reduction). In this latter group, the reduction in NPC death was coupled with a delay in neurogenesis, suggesting that inappropriate survival of NPC subpopulations creates a barrier to initiating timely neuronal differentiation. Importantly, these observations persist in patient-derived cerebral organoids harboring the same mutations (**Figure 2.6, Table 2.2**).

## 2.6 Figures and tables

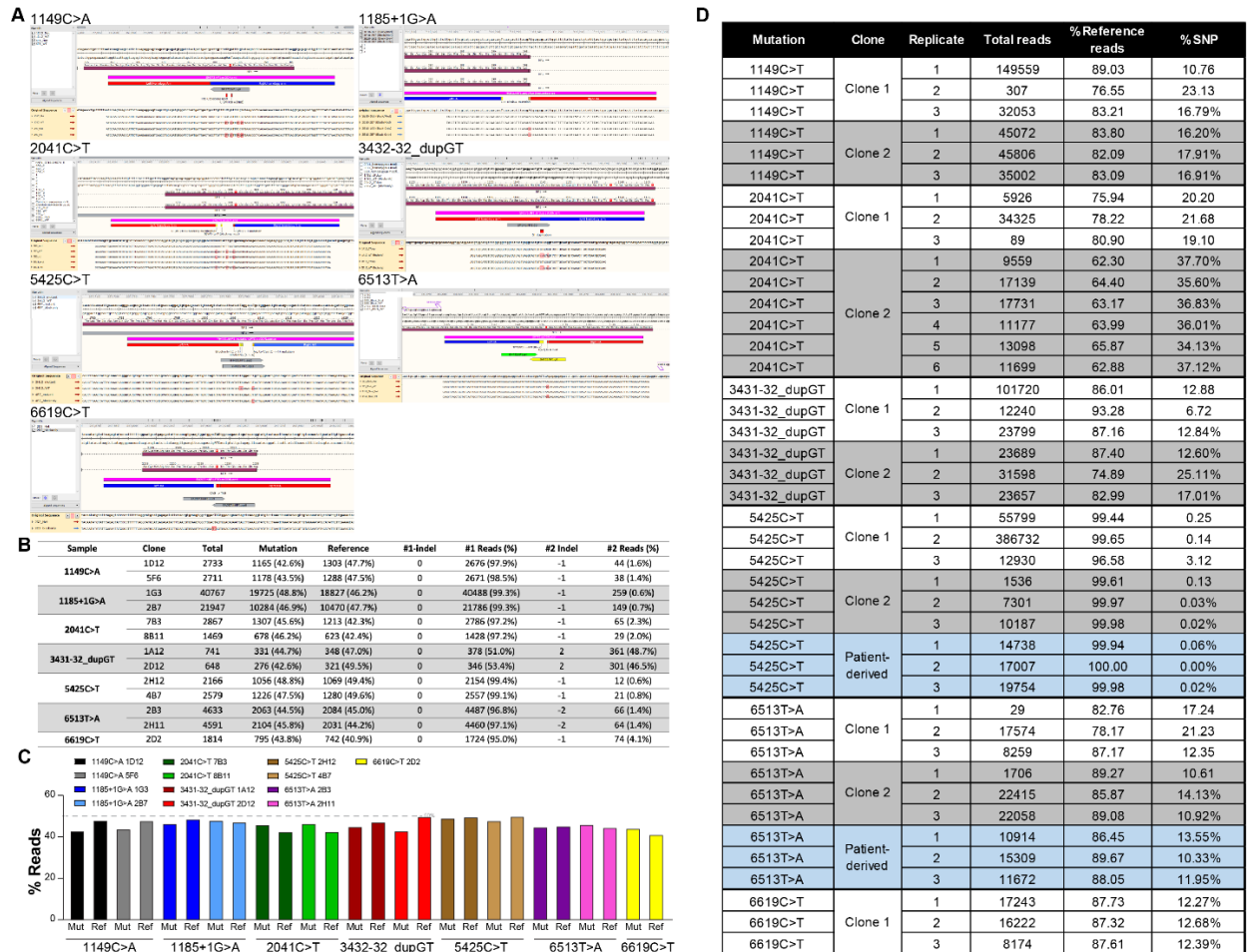


**Figure 2.1 | Isogenic *NFI*-mutant hiPSC sequencing and allele expression analysis of isogenic and patient-derived *NFI*-mutant hiPSCs.**

(A) Snapgene view of NGS sequencing of all *NFI*-mutant hiPSC clones. (Block only: control;

Block/mod: introduced *NFI* gene mutation). (B-C) Table and histogram summarizing the

percentage of sequence reads detected for the mutant and reference (wild-type) alleles at the

mutation site at the genomic level. (D) Analysis of reference and mutant (SNP) allele expression

in each *NFI*-mutant hiPSC line at the RNA level demonstrates that the wild-type reference allele

is over-represented in all *NFI*-mutant hiPSCs relative to the mutation-bearing (SNP) allele. Data are represented as the percentages of reference and mutant reads relative to the total reads.

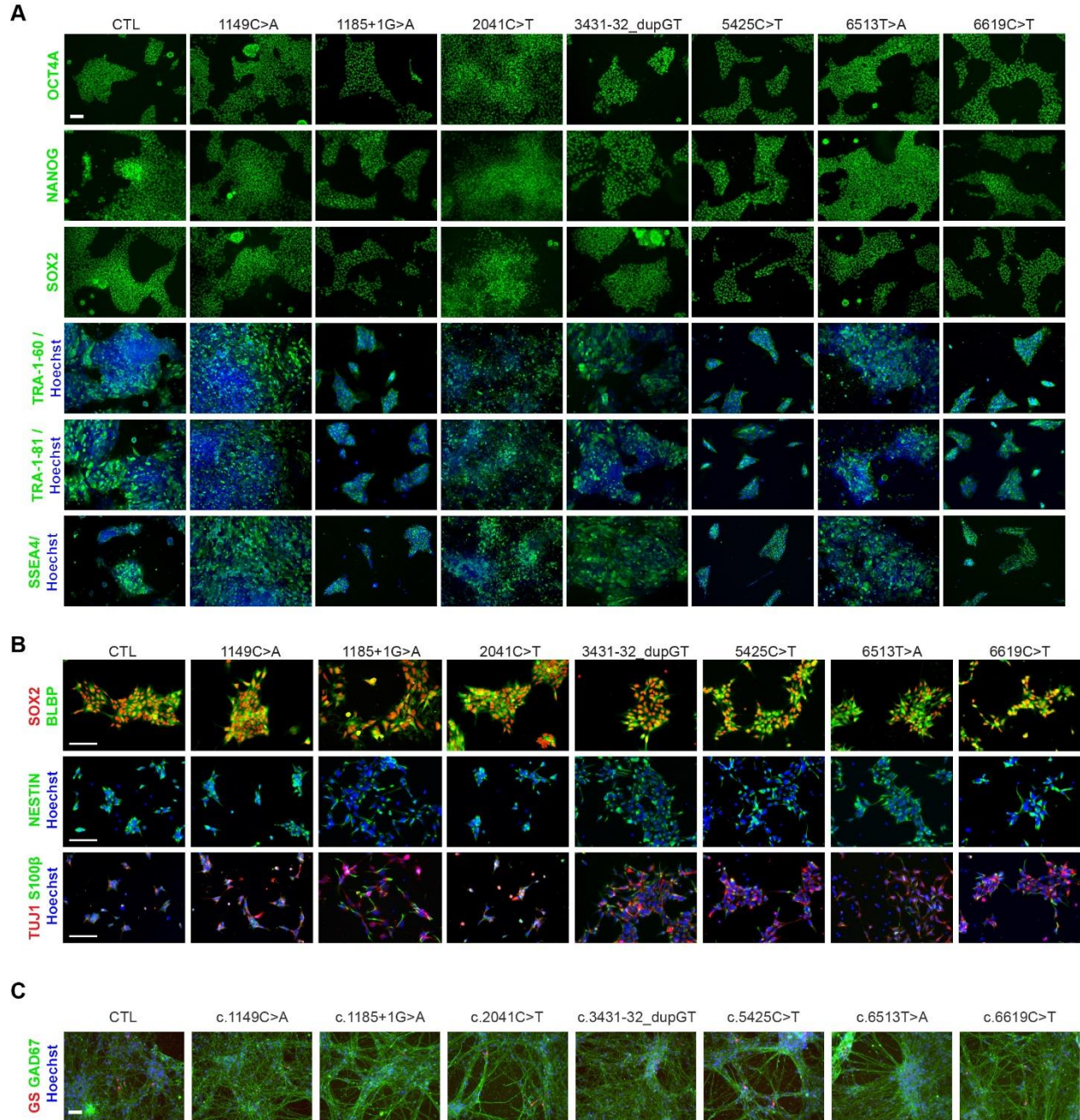


**Figure 2.2 | Analysis of isogenic hiPSCs, NPCs, and cerebral organoids.**

(A) Immunofluorescence analysis of all hiPSCs with the NANOG, SOX2, OCT4A, SSEA-4, TRA-1-60, and TRA-1-81 pluripotency markers. Scale bar, 100μm. (B) NPCs were immunopositive for the SOX2, BLBP and NESTIN neural stem cell markers (top two panels),

and were multipotent, as illustrated by TUJ1<sup>+</sup> and S100β<sup>+</sup> double labeling (bottom panel). Scale bars, 100μm. (C) Control and *NFI*-mutant NPC-differentiated GABAergic neuronal cultures were immunopositive for GAD67 (green) and immunonegative for the excitatory neuron marker glutamate synthetase (GS; red). Scale bar, 100μm.

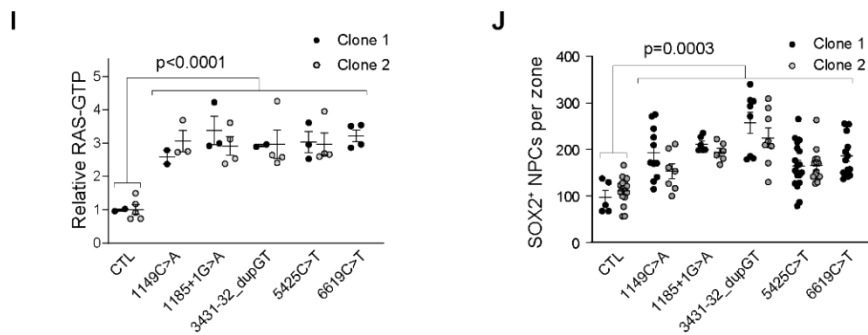
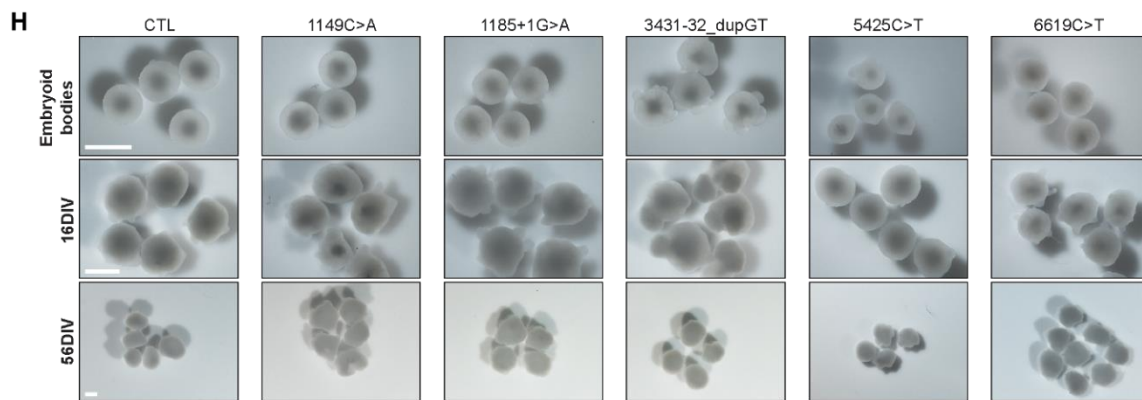
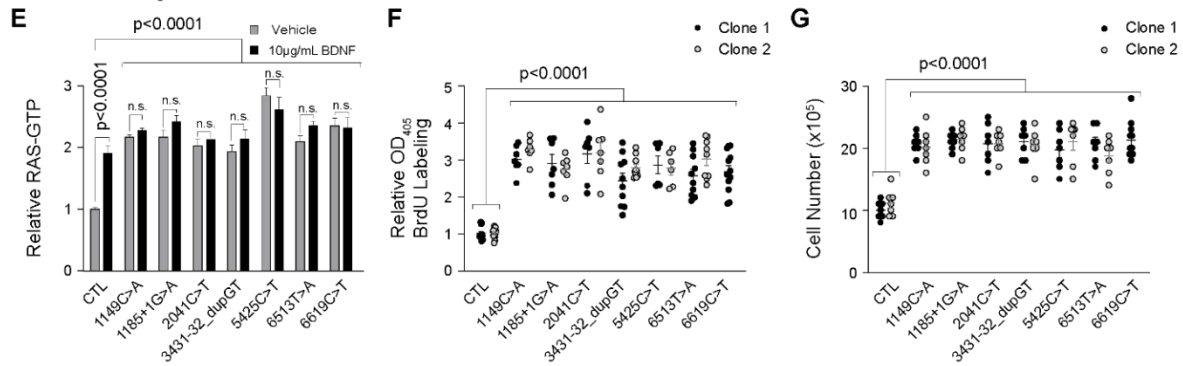
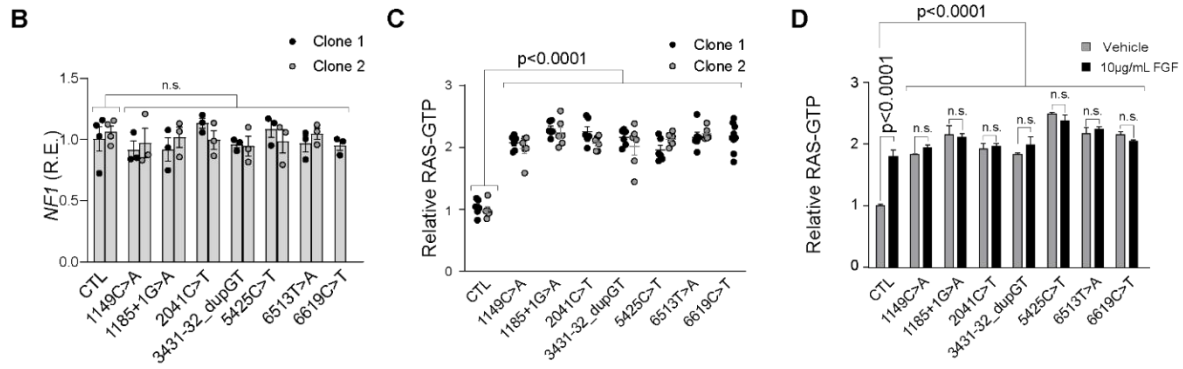
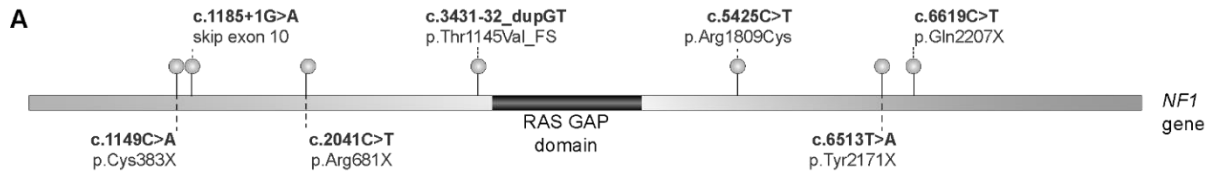


**Figure 2.3 | Isogenic *NF1*-mutant hiPSC-derived NPCs exhibit increased RAS activity and cell proliferation.**

(A) Schematic diagram illustrating the position of the engineered *NF1* patient mutations within the *NF1* gene. The location of the RAS-GAP domain is highlighted in black. (B) Relative *NF1* mRNA expression in isogenic *NF1*-mutant NPCs is similar to the controls. (C–E) (C) Quantitation demonstrating increased RAS activity (RAS-GTP) in isogenic *NF1*-mutant NPCs relative to controls (CTL) before and after the addition of (D) 10  $\mu$ g/mL FGF or (E) BDNF. A minimum of three independent replicates was performed for each treatment condition. (F) BrdU incorporation is increased by 2.6- to 3.2-fold in *NF1*-mutant NPCs relative to control NPCs. (G) 1.9- to 2-fold increases in total cell numbers were observed in *NF1*-mutant NPCs compared with controls. (H) Representative bright-field images of embryoid bodies and cerebral organoids at 16 and 56DIV. (I–J) (I) Quantitation demonstrating increased RAS activity (2.8- to 3.2-fold) and (J) increased numbers of SOX2<sup>+</sup> NPCs per ventricular zone (1.6- to 2.2-fold) in 16DIV *NF1*-mutant cerebral organoids relative to control organoids. Each dot represents an independently generated data point derived from separate experiments and the two different clones for each line are denoted as black versus gray dots. All data are represented as means  $\pm$  SEM. (B, C, F, G, I, and J) One-way ANOVA with Tukey post-test. (D–E) Two-way ANOVA with Bonferroni post-test. n.s., not significant. Scale bar, 1 mm.

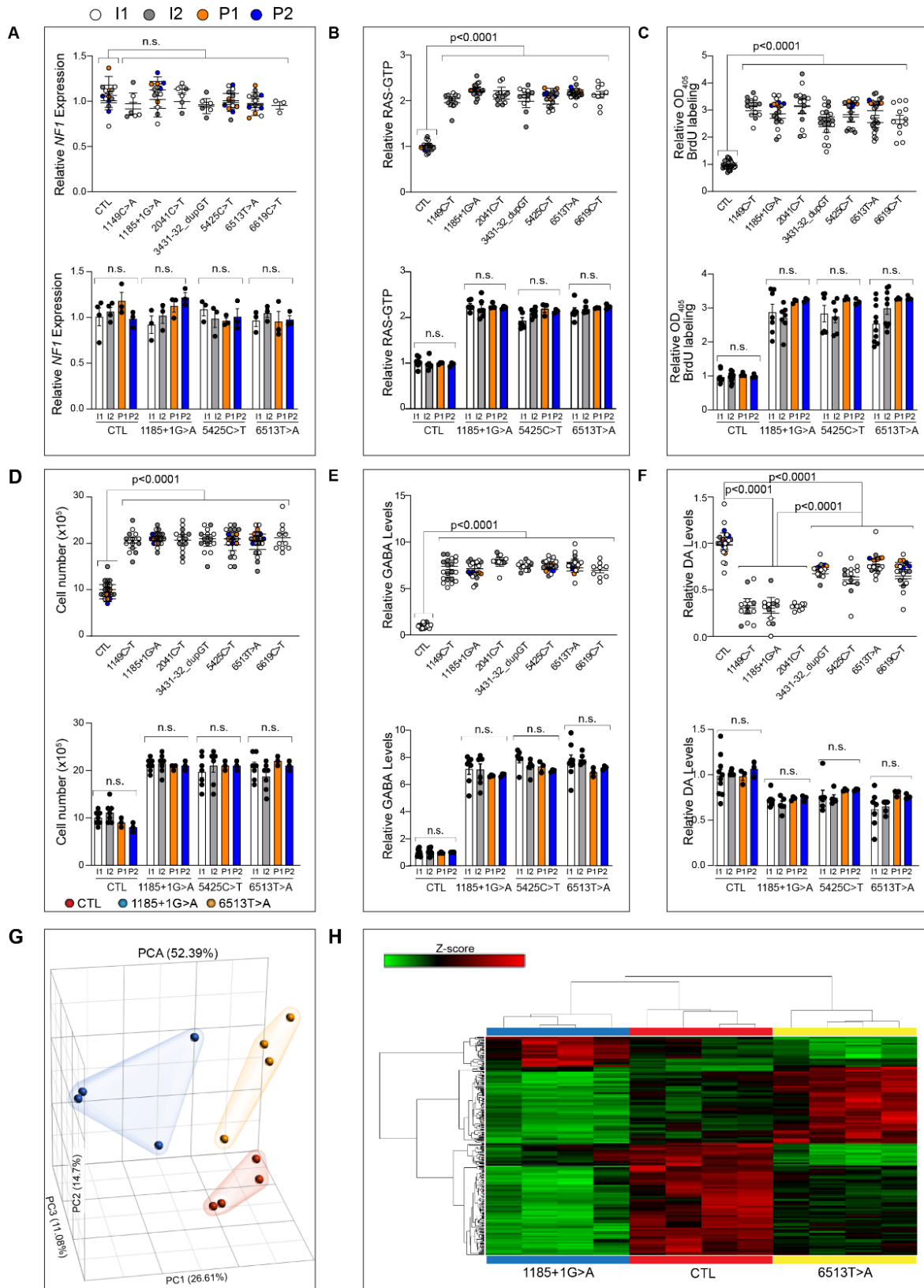




**Figure 2.4 | Comparisons between isogenic and patient-derived *NFI*-mutant hiPSC-NPCs.**

(A) Relative *NFI* mRNA expression, (B) RAS activity, (C) BrdU incorporation, and (D) cell numbers are similar between the isogenic and their respective patient-derived NPC lines that harbor the same *NFI* gene mutation. The top panels illustrate all the clones (Isogenic clones: I1, I2; white, grey circles, respectively; Patient-derived clones: P1, P2; orange and blue circles, respectively) employed for each assay, and represent comparisons between all *NFI*-mutant NPCs and controls. The bottom panels illustrate the individual comparisons between the isogenic (I1, I2) and their respective patient-derived (P1, P2) NPCs (CTL; c.1185+1G>A; c.5425C>T; c.6513T>A). Relative (E) GABA levels and (F) DA levels are similar between the isogenic and their respective patient-derived NPC lines harboring the same *NFI* gene mutation. The top panels illustrate all the clones (Isogenic clones: I1, I2; white, grey circles, respectively; Patient-derived clones: P1, P2; orange and blue circles, respectively) employed for each assay, and represent the comparisons between all *NFI*-mutant NPCs and controls. The bottom panels illustrate the individual comparisons between the isogenic (I1, I2) and their respective patient-derived (P1, P2) NPCs (CTL; c.1185+1G>A; c.5425C>T; c.6513T>A). All data are represented as means  $\pm$  SEM; Oneway ANOVA with Tukey post-test. ns, not significant. (G) PCA plot and (H) histogram analysis illustrate differential clustering of gene expression between patient-derived and isogenic NPCs harboring two separate *NFI* mutations (c.1185+1G>A; c.6513T>A) or no *NFI* mutation (control; CTL), following next-generation sequencing.

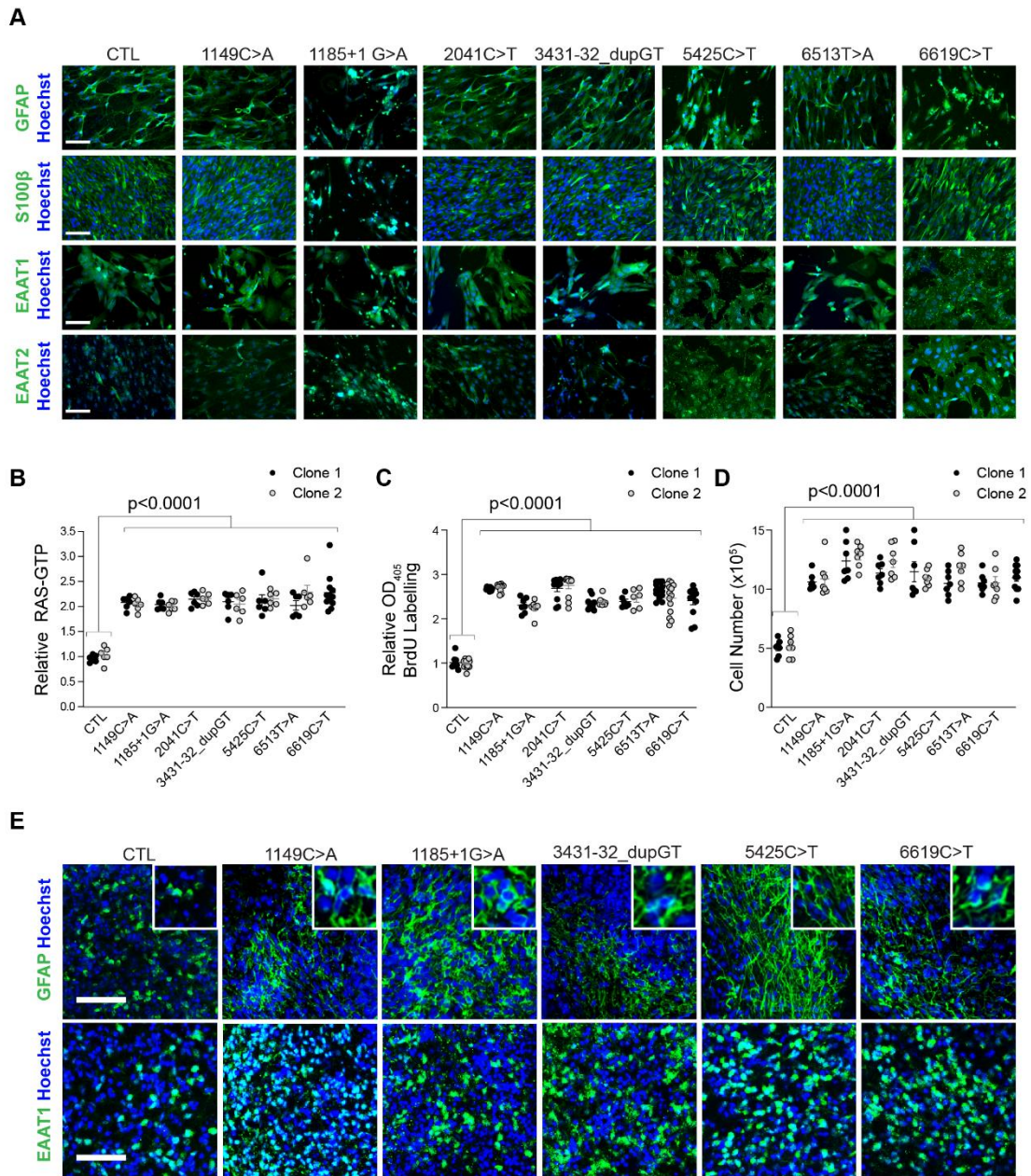


**Figure 2.5 | hiPSC-derived *NF1*-mutant astroglia exhibit increased RAS activity and cell proliferation.**

(A) *NF1*-mutant and control NPCs were differentiated into GFAP<sup>+</sup>, S100<sup>+</sup>, EAAT1<sup>+</sup>, and EAAT2<sup>+</sup> astrocytes in 2D cultures. Scale bar, 100  $\mu$ m. (B) RAS-GTP was increased by 2- to 2.3-

fold in *NFI*-mutant astrocytes relative to controls (CTL). **(C)** Proliferation of *NFI*-mutant astrocytes was 2.3- to 2.7-fold higher relative to controls. **(D)** Direct cell counting demonstrated a 2.1- to 2.5-fold increase in *NFI*-mutant astrocytes compared with controls.

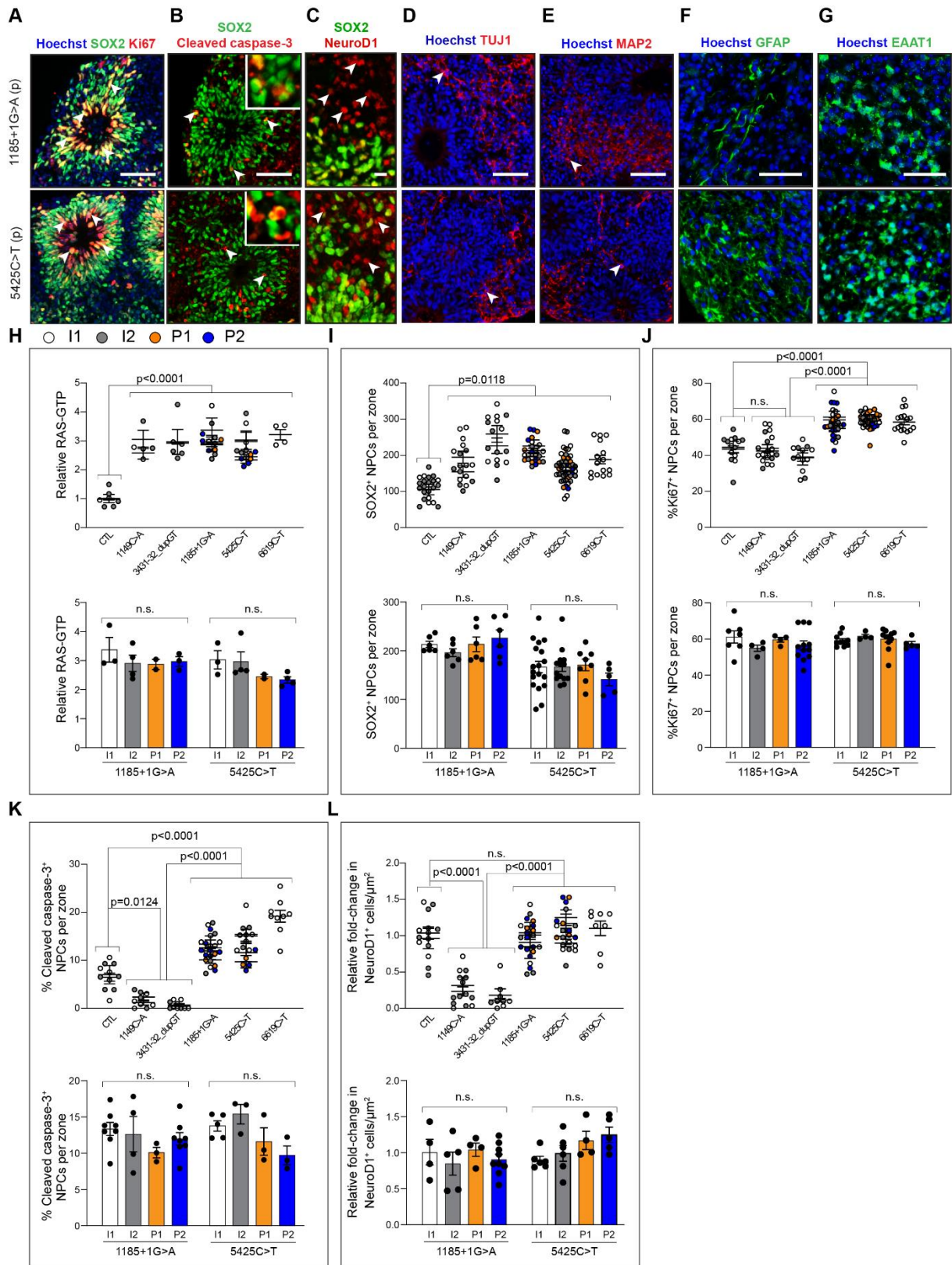


**Figure 2.6 | Comparisons between isogenic and patient-derived *NFI*-mutant hiPSC-organoids.**

Representative images of (A) NPC proliferation (Ki67<sup>+</sup> cells; white arrowheads), (B) NPC apoptosis (cleaved caspase-3; white arrowheads), (C, D) early immature neurons (NeuroD1; TUJ1; white arrowheads), (E) late immature neurons (MAP2; white arrowheads) at 16DIV, and the production of (F) EAAT1<sup>+</sup> glial cells and (G) GFAP<sup>+</sup> fibers at 56DIV in cerebral organoids generated from c.1185+1G>A and c.5425C>T patient-derived hiPSC lines. Scale bars: (C) 10μm; (A, B, D, E, F, G) 50μm. There were no differences in (H) RAS activity or (I) SOX2<sup>+</sup> NPCs per ventricular zone (VZ) between the isogenic *NFI*-mutant cerebral organoids and their corresponding patient-derived at 16DIV. There were no differences in (J) %Ki67<sup>+</sup> NPCs per VZ, (K) %cleaved caspase-3<sup>+</sup> NPCs per VZ, or (L) NeuroD1<sup>+</sup> immature neurons between the isogenic *NFI*-mutant and their corresponding patient-derived cerebral organoids at 16DIV. The top panels illustrate all the clones (Isogenic clones: I1, I2; white, grey circles, respectively; Patient-derived clones: P1, P2; orange and blue circles, respectively) employed for each assay, and represent the comparisons between all *NFI*-mutant organoids and controls. The bottom panels illustrate the individual comparisons between the isogenic (I1, I2) and their respective patient-derived (P1, P2) NPCs (c.1185+1G>A; c.5425C>T). All data are represented as means ± SEM; One-way ANOVA with Tukey post-test. ns, not significant.

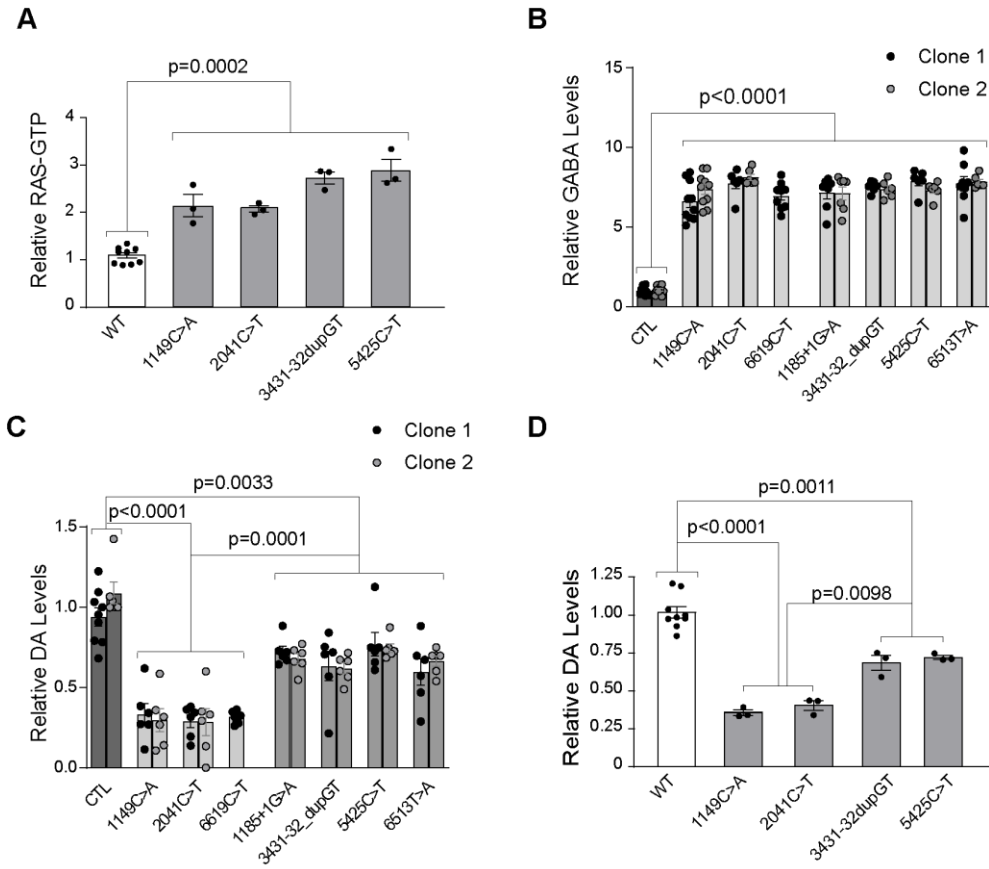


**Figure 2.7 | hiPSC-derived *Nf1*-mutant neurons, NPCs, and *Nf1*-mutant mice display molecular similarities and differences.**

(A) *Nf1*-mutant (c.1149C > A, c.2041C > T, c.3431- 32\_dupGT, c.5425C > T) genetically engineered mouse brain lysates exhibit increased RAS activity compared with wild-type littermate controls. (B) GABA levels are increased in all *Nf1*-mutant NPC-derived neurons relative to controls. (C-D) Dopamine levels are differentially reduced in (C) *Nf1*-mutant NPCs relative to controls and (D) *Nf1*-mutant genetically engineered mouse brain lysates compared with WT littermate controls. Each dot represents an independently generated data point derived from separate experiments and the two different clones for each line are denoted as black versus gray dots. All data are represented as means ± SEM. One-way ANOVA with Tukey post-test.

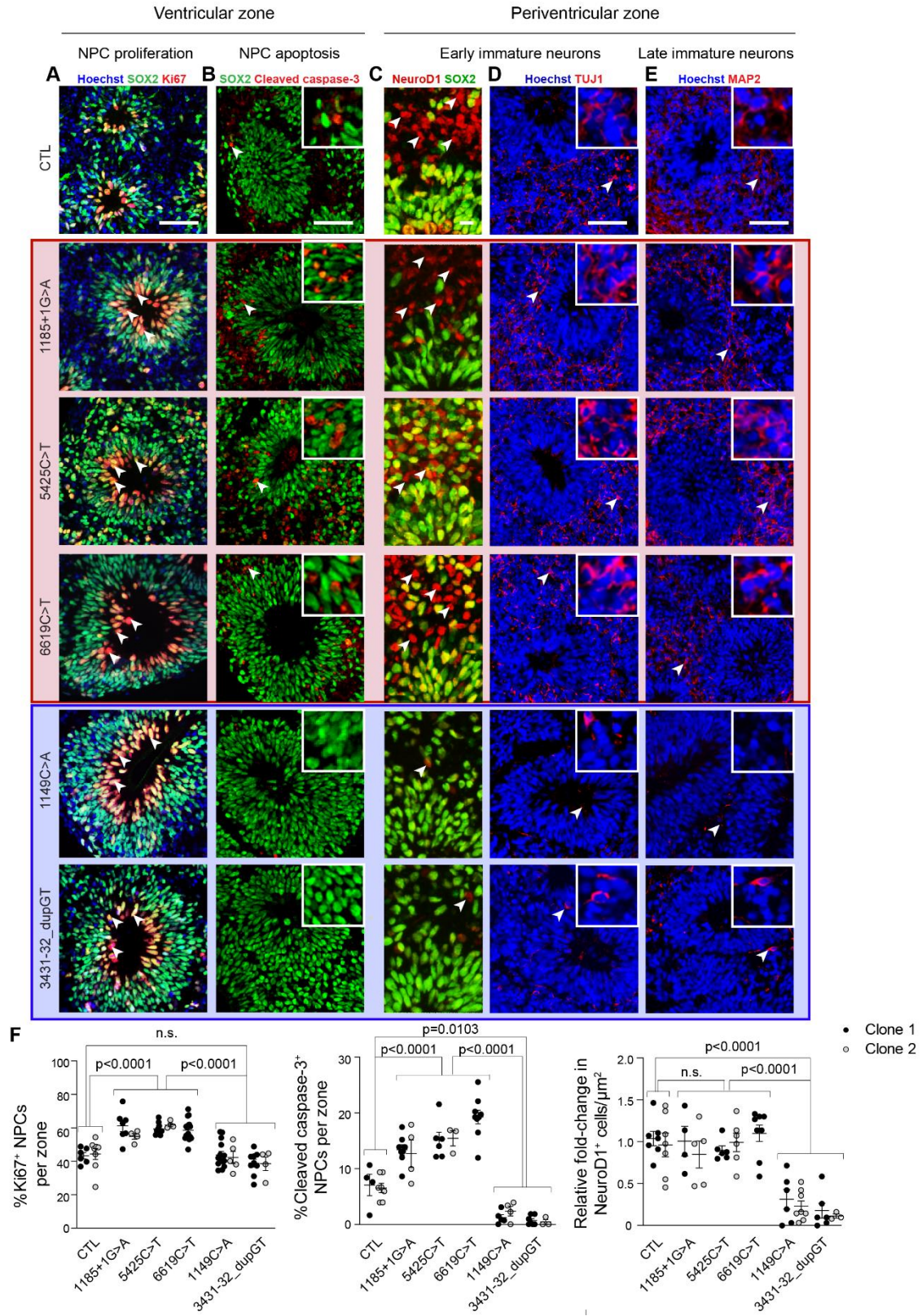


**Figure 2.8 | Differential effects of *NF1* mutations on cerebral organoid progenitor cell dynamics and neurogenesis.**

(**A-B**) SOX2<sup>+</sup> NPCs in the ventricular zones of group 1 *NF1*-mutant cerebral organoids exhibit (**A**) 1.3- to 1.4-fold increased proliferation (Ki67<sup>+</sup> cells; white arrowheads) and (**B**) 2- to 3-fold increased cell apoptosis (cleaved caspase-3; white arrowheads) compared with control and group 2 cerebral organoids at 16DIV. (**C-E**) Decreased numbers of (**C, D**) early immature neurons (NeuroD1; TUJ1 white arrowheads) and (**E**) late immature neurons (MAP2; white arrowheads) migrating into the periventricular zone of group 2 compared with group 1 and control cerebral organoids at 16DIV. (**F**) Quantifications of %Ki67<sup>+</sup> NPCs, %cleaved caspase-3<sup>+</sup> NPCs and NeuroD1<sup>+</sup> immature neurons in *NF1*-mutant cerebral organoids compared with controls at 16DIV. Each dot represents an independently generated data point derived from separate experiments and the two different clones for each line are denoted as black versus gray dots. All data are represented as means ± SEM. One-way ANOVA with Dunnett post-test. n.s., not significant. Scale bars: (**C**) 10 μm; (**A, B, D, and E**) 50 μm.



**Table 2.1 | Primary antibodies.**

<b>Antibody</b>	<b>Vendor</b>	<b>Catalog No</b>	<b>Host</b>	<b>Application (dilution)</b>
BLBP	Millipore	ABN14	Rabbit	ICC (1:200)
Cleaved caspase-3	Cell Signaling	9664	Rabbit	IF (1:250)
EAAT1	Abcam	ab416	Rabbit	ICC, IF (1:500)
EAAT2	Abcam	ab41621	Rabbit	ICC (1:500)
GFAP	Abcam	ab4648	Mouse	ICC, IF (1:500)
Ki67	Fisher Scientific	BDB556003	Mouse	IF (1:100)
MAP2	Abcam	ab11267	Mouse	IF (1:500)
Nanog (D73G4)	Cell Signaling	9656S	Rabbit	ICC (1:200)
Nestin	Abcam	ab92391	Rabbit	ICC (1:250)
NeuroD1	Abcam	ab60704	Mouse	IF (1:500)
Oct-4A (C30A3)	Cell Signaling	9656S	Rabbit	ICC (1:200)
S100 $\beta$	Abcam	ab41548	Rabbit	ICC (1:200)
SOX2	Cell Signaling	4900S	Mouse	ICC (1:1000); IF (1:250)
Sox2 (D6D9)	Cell Signaling	9656S	Rabbit	ICC (1:200)
SOX2	Abcam	ab92494	Rabbit	IF (1:250)
SSEA4 (MC813)	Cell Signaling	9656S	Mouse	ICC (1:200)
TRA-1-60 (S)	Cell Signaling	9656S	Mouse	ICC (1:200)
TRA-1-81	Cell Signaling	9656S	Mouse	ICC (1:200)
TUJ-1	Abcam	ab78078	Mouse	ICC (1:1000)

**Table 2.2 | Inter-clone analysis of control and *NFI*-mutant hiPSC-derived cells and organoids.**

	NPCs <i>NFI</i> Relative Expression		Isogenic NPCs *			Isogenic Astrocytes *				
	Isogenic *	Isogenic vs Patient-derived **	RAS assays	BrdU Assays	Direct cell count	RAS assays	BrdU Assays	Direct cell count		
CTL	0.598	0.479 / 0.634	0.559	0.929	0.258	0.317	0.566	0.775		
1149C>T	0.153	n/a	0.383	0.155	0.657	0.604	0.395	0.690		
1185+1G>A	0.953	0.046 / 0.956	0.564	0.552	0.758	0.532	0.504	0.563		
2041C>T	0.381	n/a	0.078	0.939	>0.999	0.847	0.543	0.142		
3431-32_dupGT	0.570	n/a	0.363	0.146	0.686	0.709	0.426	0.553		
5425C>T	0.151	3.380 / 0.104	0.065	0.785	0.491	0.742	0.458	0.060		
6513T>A	0.846	0.941 / 0.441	0.590	0.093	0.204	0.148	0.096	>0.999		
	Isogenic vs Patient-derived NPCs **			NPCs GABA		NPCs DA				
	RAS assays	BrdU Assays	Direct cell count	Isogenic *	Isogenic vs Patient-derived **	Isogenic *	Isogenic vs Patient-derived **			
CTL	0.309 / 0.742	0.593 / 0.573	1.207 / 0.343	0.598	0.479 / 0.634	0.121	0.925 / 0.431			
1149C>T	n/a	n/a	n/a	0.153	n/a	0.716	n/a			
1185+1G>A	0.372 / 0.704	1.399 / 0.318	2.600 / 0.154	0.953	0.046 / 0.956	0.371	0.017 / 0.984			
2041C>T	n/a	n/a	n/a	0.381	n/a	0.963	n/a			
3431-32_dupGT	n/a	n/a	n/a	0.570	n/a	0.879	n/a			
5425C>T	0.598 / 0.580	1.058 / 0.404	1.000 / 0.422	0.151	3.380 / 0.104	0.766	0.188 / 0.833			
6513T>A	1.289 / 0.322	3.975 / 0.058	0.500 / 0.622	0.846	0.941 / 0.441	0.469	0.986 / 0.410			
	Isogenic Organoids *					Isogenic vs Patient-derived **				
	Ki67 <sup>+</sup>	RAS assays	NSCs per PZ	NeuroD1 <sup>+</sup>	Cleaved Caspase 3 <sup>+</sup>	Ki67 <sup>+</sup>	RAS assays	NSCs per PZ	NeuroD1 <sup>+</sup>	Cleaved Caspase 3 <sup>+</sup>
CTL	0.803	0.943	0.367	0.651	0.603	n/a	n/a	n/a	n/a	n/a
1149C>T	0.711	0.354	0.125	0.517	0.433	n/a	n/a	n/a	n/a	n/a
1185+1G>A	0.217	0.383	0.138	0.527	0.784	0.830/ 0.491	0.561/ 0.656	0.632/ 0.599	0.488/ 0.695	0.838/ 0.491
3431-32_dupGT	0.944	0.951	0.291	0.636	0.895	n/a	n/a	n/a	n/a	n/a
5425C>T	0.216	0.909	0.982	0.466	0.288	0.780/ 0.516	1.850/ 0.208	0.632/ 0.599	2.675/ 0.080	4.029/ 0.037

Table detailing the inter-clone analyses of isogenic iPSC-derived NPCs and organoids, as well as isogenic versus patient-derived hiPSC-derived NPCs and organoids harboring the same germline *NFI* mutations. There are no statistically significant differences in the relative *NFI* mRNA expression in NPCs, RAS activity, BrdU incorporation, or cell number in NPCs or astrocytes, GABA and dopamine (DA) levels in NPCs, %Ki67<sup>+</sup> progenitor cells per ventricular zone (VZ), RAS activity, NPCs per ventricular zone (VZ), NeuroD1<sup>+</sup> cells or %cleaved caspase3<sup>+</sup> progenitor cells per VZ in cerebral organoids. \*t-test; P-values reported, \*\*One-Way ANOVA; F / P-values reported, respectively. n/a: not applicable.

## 2.7 Discussion

The findings described in this report, in combination with compelling population-based genotype-phenotype associations, suggest that the germline *NF1* gene mutation is one of the factors that underlies clinical heterogeneity in patients with NF1. Using an isogenic series of *NF1*-mutant hiPSC lines, we identified differential *NF1* mutational effects on human CNS cells and tissues. Importantly, unlike prior studies, the use of an isogenic series of hiPSCs eliminates other contributing factors, like sex and genomic variation (potential modifier genes) and permits a direct examination of the effects of different *NF1* gene mutations. Moreover, this study raises several important points relevant to NF1 pathobiology.

First, we established that all heterozygous *NF1* gene mutations similarly increase CNS NPC and astroglial cell proliferation and RAS activity, which is consistent with numerous reports demonstrating that neurofibromin controls cell proliferation largely by regulating RAS activity in mouse, swine, and *Drosophila* cells and tissues. Moreover, the regulation of RAS-mediated cell proliferation by neurofibromin is further supported using paired hiPSC-derived NPCs, heterozygous and homozygous for the same *NF1* gene mutation, where a clear gene dose dependency was revealed (C. Anastasaki, manuscript in preparation). As such, the vast majority of human clinical trials for *NF1*-null tumors have appropriately employed molecularly targeted therapies that inhibit RAS and RAS downstream effectors (*e.g.*, MEK) (Dombi et al., 2016).

Second, we demonstrated differential effects of *NF1* germline mutations on neuronal differentiation. These differential effects could reflect the fact that neurofibromin functions as a

high-affinity dimer, where different mutations could change the overall architecture of the dimer interface (Sherekar et al., 2020). Since neurons from individuals with NF1 harbor only a single *NF1* germline mutation, different *NF1* mutations likely cause unique neuron-related pathologies. As such, the use of isogenic hiPSCs revealed differential effects of distinct *NF1* gene mutations on NPC proliferation, apoptosis, and neuronal differentiation not previously reported in the developing *Nf1*-knockout (*Nf1*<sup>wt/neo</sup>) mouse brain. Given the high degree of mutational specificity for autism symptomatology in children with NF1 (Morris and Gutmann, 2018), these findings suggest that investigations employing *Nf1* mice with different patient germline *Nf1* mutations might uncover unique behavioral abnormalities not appreciated using conventional *Nf1* knockout mice (Costa et al., 2002; Omrani et al., 2015) and identify causative underlying molecular mechanisms.

Third, the fact that the observed differences in neuronal differentiation in cerebral organoids and NPC DA levels do not correlate with RAS activation supports the existence of non-RAS-mediated neurofibromin functions. In this regard, neurofibromin also directly binds to several proteins important for neuronal differentiation, spinogenesis and serotonin receptor activity, including collapsin response mediator protein-2 (Patrakitkomjorn et al., 2008), syndecan (Hsueh et al., 2001), and the 5-hydroxytryptamine-6 receptor (Deraredj Nadim et al., 2016), through domains distinct from the GRD. Moreover, the notion that non-RAS-mediated neurofibromin functions exist in neurons is reinforced by the presence of a neurofibromin isoform containing an additional amino terminal exon (11alt12), whose expression is restricted to postnatal brain neurons (Gutmann et al., 1999b). Future investigations aimed at discovering novel neuron-

specific neurofibromin binding partners will be critical to understanding how *NF1* mutations differentially affect cognition and behavior in children with NF1.

Finally, although population and murine studies provided the first evidence for *NF1* genotype-phenotype correlations, there had been no direct demonstration of the primary effect of the *NF1* mutation at the cellular and tissue levels in humans. The use of this experimental human iPSC platform revealed *NF1* mutational abnormalities in human NPCs and neurons. Collectively, these studies establish a foundational basis for future studies aimed at unraveling mechanistic etiologies responsible for *NF1*-specific CNS phenotypes, discovering new therapeutic targets, and assessing treatments relevant to precision medicine.

**Chapter 3: hiPSC-derived hCOs harboring a  
17q11.2 microdeletion reveal *CRLF3* as a  
critical regulator of neurogenesis**

## 3.1 Preface

**This chapter is adapted from the following manuscript:**

**Wegscheid, M.L., et al.** Patient-derived iPSC-cerebral organoid modeling of the 17q11.2 microdeletion syndrome establishes *CRLF3* as a critical regulator of neurogenesis. *Cell Reports* **36**, 109315 (2021).

**Author contributions for the citation above:**

M.L.W. and D.H.G designed the experiments. M.L.W., K.A.H., O.M.C., C.A., S.M.M., and J.B.P. conducted the experiments and/or analyzed the data. S.M.M. and J.N.T. collected patient specimens. The manuscript was assembled by M.L.W. and D.H.G.

## 3.2 Abstract

Neurodevelopmental disorders are often caused by chromosomal microdeletions comprising numerous contiguous genes. A subset of Neurofibromatosis type 1 (NF1) patients with severe developmental delays and intellectual disability harbor such a microdeletion event on chromosome 17q11.2, involving the *NF1* gene and flanking regions (*NF1* total gene deletion; *NF1*-TGD). Using patient-derived human induced pluripotent stem cell (hiPSC)-forebrain cerebral organoids (hCOs), we identified both neural stem cell (NSC) proliferation and neuronal maturation abnormalities in *NF1*-TGD hCOs. While increased NSC proliferation resulted from decreased *NF1*/RAS regulation, the neuronal differentiation, survival, and maturation defects were caused by reduced cytokine receptor-like factor 3 (*CRLF3*) expression and impaired RhoA signaling. Furthermore, we demonstrated a higher autistic trait burden in NF1 patients harboring a deleterious germline mutation in the *CRLF3* gene (c.1166T>C, p.Leu389Pro). Collectively, these findings identify a new causative gene within the *NF1*-TGD locus responsible for hCO neuronal abnormalities and autism in children with NF1.

## 3.3 Introduction

Neurodevelopmental disorders (NDDs) comprise a diverse collection of syndromes in which affected children exhibit autism spectrum symptomatology, cognitive delays, and intellectual disabilities. Genomic sequencing and chromosomal analyses have revealed that many NDDs are associated with chromosomal copy number variations (CNVs) (Coe et al., 2019; Grayton et al., 2012), leading to altered expression of specific genes. As such, microdeletion syndromes have



been highly instructive for identifying pathology-causing genes, as well as dissecting the underlying mechanisms responsible for these neurodevelopmental abnormalities (Frega et al., 2019; Pucilowska et al., 2018; Ramocki et al., 2010; Shcheglovitov et al., 2013).

Microdeletions on chromosome 17q11.2 most commonly encompass 1.4 Mb of genomic DNA, including the entire *NF1* gene and its flanking regions (type-1 *NF1*-total gene deletion; *NF1*-TGD). These microdeletion events are found in 4.7-11% of patients with Neurofibromatosis type 1 (NF1; OMIM #162200) (Kluwe et al., 2004; Rasmussen et al., 1998), where children with *NF1*-TGD mutations manifest profound developmental delays, intellectual disability (IQ < 70), and an elevated risk of cancer (Descheemaeker et al., 2004; Mautner et al., 2010; Ottenhoff et al., 2020; Pasmant et al., 2010; Venturin et al., 2004). While it is possible that these clinical abnormalities result from the total deletion of one copy of the *NF1* gene, the *NF1*-TGD locus contains 13 other protein-coding and four microRNA genes, which could also contribute to these manifestations. To this end, only the deletion of one of these genes, *SUZ12*, has been previously correlated with the increased cancer incidence in these patients (De Raedt et al., 2014; Lee et al., 2014; Wassef et al., 2019; Zhang et al., 2014). In contrast, the underlying molecular etiologies for the neurodevelopmental deficits in this population are unknown.

To define the molecular and cellular cause(s) for the neurodevelopmental abnormalities in patients with 17q11.2 microdeletions, we established human induced pluripotent stem cell (hiPSC)-forebrain cerebral organoid (hCO) models from several NF1 patients with a 1.4 Mb *NF1*-TGD mutation (TGD hCOs). Leveraging this platform, we identified neuronal survival, differentiation, and maturation abnormalities in the TGD hCOs, which were not observed in

hCOs harboring intragenic *NF1* mutations or an atypical deletion (aTGD). Using several converging strategies, we identified a single gene (*CRLF3*) and signaling pathway (RhoA activation) responsible for the neuronal maturation defects observed in TGD hCOs. Moreover, we demonstrated a higher autistic trait burden in NF1 patients harboring a deleterious germline mutation in the *CRLF3* gene (p.Leu389Pro). Collectively, these experiments reveal a new causative gene and mechanism responsible for the profound neurodevelopmental abnormalities of TGD hCOs.

### 3.4 Materials and methods

#### *Human induced pluripotent stem cells*

Patient-derived hiPSC lines were reprogrammed by the Washington University Genome Engineering and iPSC Core Facility (GEiC) using biospecimens (skin, blood, urine) acquired from three individuals harboring a 1.4 Mb *NF1*-total gene deletion (TGD) and one patient harboring an atypical TGD (aTGD) (**Table 3.1**) with an established diagnosis of NF1 under an approved Human Studies Protocol at Washington University. As atypical TGD mutations are rare in the NF1 population (Messiaen et al., 2011), no additional patients with this genomic alteration were available to generate hiPSC lines. Briefly, fibroblasts, renal cells or peripheral blood cells were infected with a Sendai virus carrying four stem cell reprogramming factors (*OCT4*, *KLF4*, *SOX2*, *C-MYC*), as previously reported (Anastasaki et al., 2020; Anastasaki et al., 2015). hiPSC colonies were isolated and pluripotency was confirmed by morphological assessment and expression of stem cell markers (**Figure 3.1A**). Two to three different clones were expanded for each line, tested, and verified negative for *Mycoplasma* contamination, and

used to generate human cerebral organoids (hCOs) (**Figure 3.1B-E**), neural stem cells (NSCs) (**Figure 3.7H**) and neurons. The sizes of the *NF1* locus deletions were determined by MLPA assay (MRC Holland) at the Medical Genomics Laboratory (University of Alabama, Birmingham). Single clones of two patient-derived neurologically normal controls were provided by Drs. Matthew B. Harms (CTL2, male) and Fumihiko Urano (CTL3, male) at Washington University. Five distinct isogenic human induced pluripotent stem cell (hiPSC) lines harboring NF1 patient germline *NF1* gene mutations (Transcript ID NM\_000267; c.1149C>A, c.1185+1G>A, c.3431-32\_dupGT, c.5425C>T, c.6619C>T) were individually engineered into a single commercially available male control human iPSC line (BJFF.6, CTL1) as previously described (Anastasaki et al., 2020) (**Table 3.1**). All hiPSC lines generated by CRISPR/Cas9 engineering were subjected to subcloning and Illumina deep sequencing to verify the presence of the introduced mutation. These renewable resources are continuously frozen at low passage (< 5). All hiPSC clones were used for analysis and relative to prior frozen aliquots of the same clone to ensure reproducibility. hiPSCs have been authenticated by (a) routine testing for *Mycoplasma* infection, (b) regular quality control checks for pluripotency by monitoring expression of pluripotency markers, and (c) competence to undergo multi-lineage differentiation.

### ***Human subject details***

Samples for exome sequencing were acquired from a previously assembled cohort of individuals with NF1 from Washington University Neurofibromatosis Center whose DNA was banked under a Human Studies protocol approved by the Washington University Human Research Protection Office (Constantino et al., 2015). Informed consent was obtained from all participants. Patients

with copy number variants (CNVs) ( $n = 1$ ) were excluded. Of the patients between 10 and 19 years of age with clinically indicated SRS-2 testing, 11 were male (64.7%) and 6 were female (35.3%). Selected individuals ranged in age from 10 to 18 years (median, 13 years), with SRS-2 T scores from 45 to 98 (**Table 3.2**). There was no significant difference between males ( $n = 11$ ) and females ( $n = 6$ ) with respect to SRS-2 scores, between males ( $n = 5$ ) and females ( $n = 2$ ) in the group with a deleterious p.Leu389Pro *CRLF3* mutation ( $n = 7$ ), or between males ( $n = 6$ ) and females ( $n = 4$ ) without a *CRLF3* mutation ( $n = 10$ ).

### ***Human iPSC, cerebral organoid, NSC and 2D neuron cultures***

hiPSCs were cultured on Matrigel (Corning)-coated culture flasks and were fed daily with mTeSR Plus (05825, STEMCELL Technologies). hiPSCs were passaged with ReLeSR (05873, STEMCELL technologies) following manufacturer's instructions. hCOs were generated as previously described (Anastasaki et al., 2020). Briefly, cerebral organoids were cultured from hiPSCs by first aggregating 40,000 hiPSCs per well of an ultra-low binding 96-well U-bottom plate (Corning) to allow for embryoid body (EB) formation. EBs were fed every other day with STEMdiff Neural Induction Medium (05835, STEMCELL technologies) supplemented with low concentration bFGF (4ng/mL; 100-18B, PeproTech) and ROCK inhibitor (20  $\mu$ M; Y27632, Millipore) for the first 6 days, followed by NIM minus bFGF and ROCK inhibitor for an additional 3 days. Tissues were then transferred to Corning Costar 24 Well Clear Flat Bottom Ultra Low Attachment plates (1 organoid per well) in hCO differentiation medium (125 ml DMEM-F12, 125 ml Neurobasal medium, 1.25 ml N2 supplement, 62.5  $\mu$ l insulin, 2.5 ml GlutaMAX supplement, 1.25 ml MEM-NEAA, 2.5 ml B27 supplement, 2.5 ml penicillin-streptomycin, 87.5 $\mu$ l of a 1:100 dilution of 2-mercaptoethanol in DMEM-F12) on an orbital

shaker rotating at 80 rpm. hCO differentiation media was changed every 3 days. hCOs were maintained for up to 84DIV. Neural progenitor cells (NSCs) were generated using previously described methods (Anastasaki et al., 2020). For non-specific neuronal differentiation, NSCs were cultured in PLO/Laminin-coated plates in neuronal differentiation media (490 ml Neurobasal media, 5 ml N2 supplement, 5 ml MEM-NEAA ) supplemented with 0.01  $\mu\text{g/ml}$  BDNF (450-02, PeproTech), IGF-I (100-11, PeproTech), GDNF (78058, STEMCELL technologies), cAMP (1 $\mu\text{M}$ ; 1698950, PeproTech), and Compound E (0.2  $\mu\text{M}$ ; 73954, STEMCELL technologies) for 7 days.

### ***Whole exome sequencing***

Genomic DNA samples were whole exome sequenced (OtoGenetics Ltd), and FASTQ files aligned to the human reference genome assembly (GRCh37/hg19) using Samtools 1.4.1 software. Sequence variants of *CRLF3* were called, filtered, and prioritized according to their impact annotation obtained from SnpEff. Pathogenicity of resulting variants was additionally confirmed using CADD, SIFT, PolyPhen, likelihood ratio test (LRT), GERP++, and Fathmm.

### ***Next generation RNA sequencing and analysis***

RNA sequencing (RNA-seq) was performed on CTL1, CTL2, TGD1, TGD2, TGD3, aTGD and sh*CRLF3*-1 NSCs as previously described (Anastasaki et al., 2020). Sequencing analyses were generated using Partek Flow software, version 9.0.20 (Partek Inc, 2020). RNA-seq reads were aligned to the Ensembl transcripts release 100 top-level assembly with STAR version 2.7.3a (Dobin et al., 2013). Gene counts and isoform expression were derived from Ensembl output. Sequencing performance was assessed for the total number of aligned reads, total number of

uniquely aligned reads, and features detected. Normalization size factors were calculated for all gene counts by median ratio. Differential genetic analysis was then performed using DESeq2 (Love et al., 2014) to analyze for differences between conditions. Results for TGD samples compared separately with CTLs and aTGD samples were filtered for only those genes with  $P$  values and false discovery rates (FDR)  $\leq 0.01$  and log fold-changes  $\geq \pm 5$ . This gene list was then filtered further for only non-significant genes in the comparison of TGD samples vs sh*CRLF3* samples. This resulted in a gene list of 31 genes (**Table 3.3**). Gene Ontology enrichment (Ashburner et al., 2000) was run on the resulting gene list. Deep sequencing data is in the process of being submitted to GEO.

### ***Immunohistochemistry***

hCOs were fixed, embedded and cryosectioned at 12  $\mu\text{m}$  as previously described (Sloan et al., 2018). Tissues were permeabilized in 0.5% Triton X-100 in PBS for 5 minutes. After three PBS washes, tissues were blocked in a solution of 10% goat serum (GS) in PBS for one hour at room temperature, then immunolabeled with primary antibodies, diluted in a solution of 2% GS, overnight at 4°C. The following primary antibodies were used: anti-SOX2 (1:400, 4900, Cell Signaling Technology), anti-SOX2 (1:200, ab92494, Abcam), anti-OCT4A (1:400, 2840, Cell Signaling Technology), anti-NANOG (1:800, 3580, Cell Signaling Technology), anti-SMI-32 (2.5  $\mu\text{g}/\text{mL}$ , 801701, Biolegend), anti-SMI-312 (2.5  $\mu\text{g}/\text{mL}$ , 837904, Biolegend), anti-NeuroD1 (1:250, ab205300, Abcam), anti-NeuroD1 (1:500, ab60704, Abcam), anti-NeuN (1:500, MAB377, Millipore), anti-Ki67 (1:100, BD556003, BD Biosciences), anti-MAP2 (1:500, ab11267, Abcam), anti-cleaved caspase-3 (1:250, 9664, Cell Signaling Technology), anti-active caspase-3 (1:100, AF835, R&D systems), anti-PAX6 (1:250, ab19504, Abcam), anti-OTX2

(1:200, MA5-15854, Thermo Fisher Scientific), anti-EN1 (1:50, PA5-14149, Thermo Fisher Scientific), anti-GBX2 (1:50, LS-C197281, Lifespan Biosciences), anti-TBR1 (1:200, ab31940, Abcam), anti-SATB2 (1:100, ab51502, Abcam), anti-Vimentin (1:100, 5741, Cell Signaling Technology), anti-Nestin (1:250, ab92391, Abcam). The following day, slides were washed three times with PBS and labelled with relevant secondary antibodies [AlexaFluor488/568 (1:200, Invitrogen)] for one hour at room temperature. Hoechst (1:5000 in PBS) was used for cell nucleus staining. For EdU pulse-chase analyses, 16DIV hCOs were incubated with 10  $\mu$ M EdU for 1.5 hours. EdU staining was performed using Click-IT EdU Alexa Fluor 488 Imaging Kit (C10337, Invitrogen). TUNEL assays were performed using *In Situ* Cell Death Detection Kit, Fluorescein (11684795910, Roche). All imaging was done on a Leica fluorescent microscope (Leica DMI8) using Leica Application Suite X software for initial processing. Cell counter plugin of ImageJ was used to quantify cells in images of immunolabeled hCOs.

### ***RAS, Rac1, and RhoA activity assays***

For small molecule treatments, 14DIV hCOs were incubated with 10  $\mu$ M Pan-RAS-IN-1 (HY-101295, MedChemExpress) for 48 hours, and RAS activity (STA-440, Cell Biolabs) was determined on liquid nitrogen snap frozen specimens according to the manufacturer's instructions. NSCs or 8DIV EBs were treated for 24h with 1  $\mu$ g/ml Rho Activator II (CN-03; Cytoskeleton; CN03) to induce Rho activation. RhoA (BK124, Cytoskeleton) and Rac1 (BK128, Cytoskeleton) activity assays were performed on liquid nitrogen snap frozen NSC and hCO specimens, according to the manufacturer's instructions.

### ***Real-time quantitative PCR***

Total RNA was extracted (RNeasy Mini Kit, Qiagen) from hiPSC-derived hCOs according to manufacturer's instructions. RNA concentrations and purity were assessed using a NanoDrop 2000 Spectrophotometer prior to reverse transcription using a high-capacity cDNA reverse transcription kit (4374966, Applied Biosystems). RT-qPCR was performed using TaqMan gene expression assays [*CRLF3* (Hs00367579\_m1), *ATAD5* (Hs00227495\_m1), *TEFM* (Hs00895248\_m1), *ADAP2* (Hs01106939\_m1), *COPRS* (Hs01047650\_m1), *UTP6* (Hs00251161\_m1), *SUZ12* (Hs00248742\_m1), *LRRC37B* (Hs03045845\_m1), *MIR193A* (Hs04273253\_s1), *MIR365B* (Hs04231549\_s1), *MIR4725* (Hs06637953\_s1), *MIR4733* (Hs04274676\_s1)] and TaqMan Fast Advanced Master Mix, no UNG (4444964, Applied Biosystems) according to manufacturer's instructions. All reactions were performed using the Bio-Rad CFX96 Real-Time PCR system equipped with Bio-Rad CFX Manager 3.1 software. Gene expression levels of technical replicates were estimated by  $\Delta\Delta C_t$  method using GAPDH (Hs02786624\_g1) as a reference gene.

### ***Western blot analysis***

hCO, NSC and iPSC samples were collected, sonicated in RIPA buffer (89900, Thermo Scientific) containing 2  $\mu\text{g/mL}$  aprotinin (ab146286, Abcam), 10  $\mu\text{g/mL}$  leupeptin (L2884, Sigma-Aldrich), and 1 mM PMSF (10837091001, Sigma-Aldrich), and total protein concentrations determined (Pierce BCA protein assay kit, 23225, Thermo Scientific). Reducing Laemmli buffer (1610747, Bio-Rad) was added and samples incubate at 95°C for 5 minutes. Equal amounts of protein (30 to 45  $\mu\text{g}$ ) were loaded into each well of 8% or 10% SDS-PAGE gels and run for 1.5 hours at 120 V, followed by transfer to polyvinylidene fluoride membranes



using an Invitrogen power blotting system. The membranes were blocked for 1 hour in 5 % milk in Tris-buffered saline (TBS), followed by incubation overnight at 4°C with primary antibodies in TBS: anti-SUZ12 (1 µg/mL, ab12073, Abcam), anti-COPRS (1:500, NBP2-30884, Novus Biologicals), anti-CRLF3 (1:100, HPA007596, Sigma-Aldrich), anti-ATAD5 (1:500, LS-C19118, Lifespan Biosciences), anti-UTP6 (1:300, 17671-1-AP, Proteintech), anti-N-cadherin (1:1000, ab18203, Abcam), anti-neurofibromin (1:100, manuscript in preparation), anti-Vinculin (1:5000, ab129002, Abcam) and anti-GAPDH (1:2,000, ab8245, Abcam). After washing with TBS, blots were incubated with a 1:5,000 dilution of goat anti-rabbit IRDye 680RD (926-68071, LI-COR Biosciences) and goat anti-mouse IRDye 800CW (925-32210, LI-COR Biosciences) secondary antibodies in TBS for one hour at room temperature. Imaging of immunoblots was performed using a LI-COR Odyssey Fc imaging system (LI-COR Biosciences). Protein bands were quantified using LI-COR Image Studio Software v5.2, and experimental protein values were normalized to GAPDH or Vinculin as an internal loading control.

### ***RNA interference***

CTL1 hiPSCs were infected with four independent *CRLF3* shRNA lentiviral particles (sc-94066-V, Santa Cruz Biotechnology; sh*CRLF3* A: AAAGGCTTCGCACATTCAGTTGGACAGCT; sh*CRLF3* B: TACAGTCTGAGCAGTCGAAGAAATATAGC; sh*CRLF3* C: GACATTGAAGCCGTGACTCTAGGAACCAC; TL305215V, Origene) (MOI = 5) or control shRNA lentiviral particles (sc-108080, Santa Cruz Biotechnology; TR30021V shRNA scramble control particles, Origene) (MOI = 5). Infected cultures were incubated with mTeSR Plus medium (05825, STEMCELL Technologies) containing 0.4 µg/mL puromycin (73342, STEMCELL Technologies) for selection, and the medium was replaced every other day until

drug-resistant colonies formed (~14 days). Resulting colonies were expanded, assayed for *CRLF3* gene expression by Western blotting and were differentiated into NSCs or hCOs.

### ***Ortholog sequence comparison***

NCBI's Eukaryotic Genome Annotation pipeline was used to identify vertebrate orthologs of human *CRLF3*. Amino acid sequence alignments were generated by NCBI's constraint-based multiple alignment tool (Cobalt) that finds a collection of pairwise constraints derived from conserved domain database, protein motif database, and sequence similarity, using RPS-BLAST, BLASTP, and PHI-BLAST (Papadopoulos and Agarwala, 2007). Alignment results were visualized by Jalview.

### ***Quantification and statistical analysis***

No statistical methods were used to predetermine sample size. Sample size was deemed satisfactory based on the magnitude and consistency of differences between groups. No randomization of samples was performed, and investigators were not blinded during experiments and outcome assessment. Image fields for NeuroD1<sup>+</sup> neuronal quantifications were selected from the inner subventricular zones of hCOs. Image fields for NeuN<sup>+</sup>, TBR1<sup>+</sup> and SATB2<sup>+</sup> neuronal quantifications were selected from the outer subventricular zones of hCOs. The number of biological replicates (hCOs) per independent experimental replicate per genotype is provided in the figure legends. For each genotype, all available clones were analyzed. All statistical analyses were performed using GraphPad Prism 8 software. Statistical significance was determined using one-way analysis of variance (ANOVA) with Dunnett's multiple comparisons test, Bonferroni multiple comparisons test, Tukey multiple comparison's test, two-way ANOVA with Sidak's

multiple comparison test, or unpaired, two-tailed *t*-test. The exact values from the tests are indicated in the figures. Statistical significance was defined as  $P < 0.05$ . Bar graphs indicate the mean  $\pm$  SEM. Box plot indicates median (central line), interquartile range (box) and minimum and maximum values (whiskers).

A summary table summarizing all the experiments is included in **Table 3.4**, discriminating the samples in each figure panel with the statistical methods used for analysis.

## 3.5 Results

### TGD hCOs have neuronal defects

Using hCOs from three neurologically normal control individuals and three individuals harboring a 1.4 Mb *NF1*-TGD (**Figure 3.2A**, **Table 3.1**, **Figure 3.1A-E**), we first assessed neural stem cell (NSC) proliferation. Similar to hCOs harboring intragenic *NF1* patient *NF1* gene point mutations (Anastasaki et al., 2020) (**Table 3.1**), TGD hCOs also exhibited increased NSC proliferation (%Ki67<sup>+</sup> NSCs per hCO ventricular zone [VZ]) at 16 and 35 days *in vitro* (DIV) (**Figure 3.2B, D**) and 5-ethynyl-2'-deoxyuridine (EdU) incorporation at 16DIV (**Figure 3.3A**) relative to control hCOs.

Next, to assess the temporal course of neurogenesis in these PAX6<sup>+</sup>/OTX2<sup>+</sup> dorsal telencephalic forebrain hCOs (**Figure 3.1E**), cryosections were immunostained for markers of early- (NeuroD1<sup>+</sup>) and late- (NeuN<sup>+</sup>) stage immature neurons, as well as deep- (TBR1<sup>+</sup>) and upper-layer (SATB2<sup>+</sup>) neurons (**Figure 3.2C, 3.1F-G**). The TGD hCOs produced increased numbers of

NeuroD1<sup>+</sup> immature neurons relative to control hCOs from 16 to 56DIV (**Figure 3.2E**), after which time, NeuroD1<sup>+</sup> neurons were no longer present. Late-stage immature NeuN<sup>+</sup> neurons and deep-layer TBR1<sup>+</sup> neurons were first detected at 35DIV in both control and TGD hCOs; however, the TGD hCOs had reduced numbers of NeuN<sup>+</sup> and TBR1<sup>+</sup> neurons (**Figure 3.2F, 3.1G**) at 35 and 56DIV. Despite normalization of NeuN<sup>+</sup> neuronal numbers at 84DIV (**Figure 3.2F**) and no microcephalic defects (**Figure 3.1B-D**), the TGD hCOs had reduced numbers of upper-layer SABT2<sup>+</sup> neurons at 84DIV (**Figure 3.1H**), demonstrating a persistent imbalance in the neuronal subtypes generated. This impaired neuronal differentiation was unique to the TGD hCOs, as it was not observed in hCOs harboring five distinct intragenic *NF1* gene mutations (**Table 3.1, Figure 3.3B**).

As the increased numbers of early-stage immature neurons in the TGD hCOs did not generate a compensatory increase in late-stage immature neurons, we hypothesized that the TGD NeuroD1<sup>+</sup> neurons were being eliminated by programmed cell death. To measure apoptosis, 35 and 56DIV hCOs were immunolabeled for the early- (cleaved caspase-3) and late-stage (TUNEL) apoptotic markers, respectively. Greater caspase-3 cleavage (11.8% increase; **Figure 3.2G-H**) and DNA fragmentation (6.3% TUNEL increase; **Figure 3.3C**) were observed in the TGD NeuroD1<sup>+</sup> neurons relative to controls, establishing a concurrent increase in production and apoptosis of early-stage immature neurons in TGD hCOs. The increased apoptosis of NeuroD1<sup>+</sup> neurons in TGD hCOs, coupled with differentiation of the remaining NeuroD1<sup>+</sup> neurons in TGD hCOs at 56DIV, accounts for normalization of late-stage immature neurons at 84DIV.

The finding of neuronal differentiation defects in the TGD hCOs prompted us to determine whether there were also defects in dendrite and axonal extension, as reported in children with autism spectrum disorder (ASD) and intellectual disability (Hutsler and Zhang, 2010; Lazar et al., 2014; Mukaetova-Ladinska et al., 2004; Wolff et al., 2012). While the TGD hCOs produced normal SMI-312<sup>+</sup> axonal projections, they had reduced MAP2<sup>+</sup> and SMI-32<sup>+</sup> dendrites in hCOs from 35 to 84DIV (**Figure 3.2I; 3.1F; 3.3D-E**), abnormalities not observed in hCOs harboring intragenic *NFI* mutations (**Figure 3.3F**). Similar to TGD hCOs, hiPSC-derived neurons in 2D cultures also exhibited reduced MAP2<sup>+</sup> and SMI-32<sup>+</sup> dendrites (**Figure 3.2J**). Taken together, these results reveal that TGD hCOs and hCOs harboring intragenic *NFI* mutations have increased NSC proliferation, reflecting impaired *NFI* gene function, but additionally exhibit neuronal abnormalities (dendritic maturation) unique to TGD hCOs.

### **NSC hyperproliferation in TGD hCOs is RAS-dependent**

To further explore the impact of complete *NFI* deletion on NSC proliferation in the absence of other genetic contributors, we generated hCOs from the single available patient-derived hiPSC line harboring a rare atypical (0.6-0.9 Mb) deletion (aTGD), involving the loss of six protein-coding genes, including *NFI*, but not the eight protein-coding genes deleted in the common 1.4 Mb *NFI*-TGD (**Figure 3.4A**). Similar to the TGD and intragenic *NFI*-mutant hCOs (Anastasaki et al., 2020), the aTGD hCOs had increased NSC proliferation (%Ki67<sup>+</sup> NSCs; **Figure 3.4B**) relative to controls. Since the *NFI* protein (neurofibromin) has previously been shown to mediate increased cell proliferation through RAS regulation in numerous *NFI*-mutant cell types (Chen et al., 2015; Hegedus et al., 2007; Lee et al., 2010; Sanchez-Ortiz et al., 2014; Wang et al., 2012), we hypothesized that the increased NSC proliferation observed in the *NFI*-mutant hCOs was

RAS-dependent. Similar to the intragenic *NFI*-mutant hCOs (Anastasaki et al., 2020), TGD and aTGD hCOs had increased RAS activity (1.4 and 2.1-fold, respectively) relative to controls (**Figure 3.4C**). To investigate the relationship between RAS hyperactivation and increased NSC proliferation in the *NFI*-mutant hCOs, we incubated control, TGD, and aTGD hCOs with an experimentally determined concentration of the pan-RAS inhibitor IN-1 (IN-1) for 48 hours (**Figure 3.5A-C**). While IN-1 had no effect on NSC proliferation in control hCOs (**Figure 3.5D**) or neuronal differentiation and dendrite maturation in TGD and aTGD hCOs (**Figure 3.5E-F**), it reduced the NSC hyperproliferation in TGD and aTGD hCOs (**Figure 3.4D**), confirming that RAS hyperactivation is solely responsible for the increased NSC proliferation observed in *NFI*-mutant hCOs.

#### **TGD hCOs have reduced *CRLF3* expression**

In striking contrast to the TGD hCOs, the aTGD hCOs lacked neuronal survival, differentiation and maturation abnormalities. In this regard, the aTGD hCOs produced normal numbers of late-stage immature neurons (**Figure 3.4E**), exhibited no increase in immature neuron apoptosis (**Figure 3.4F**), and had normal dendrites (**Figure 3.4G**) relative to controls. These observations demonstrate that genes outside of the atypical deletion region are responsible for the neuronal differentiation and maturation defects observed in the TGD hCOs.

To identify the responsible gene(s), we conducted a systematic analysis of the genes contained within the 1.4 Mb deletion region, but not in the atypical deletion region (**Figure 3.6A**). First, the deletion status of two genes in the aTGD hCOs (*COPRS* and *RAB11FIP4*) was assayed by RT-qPCR (**Figure 3.6B, 3.5G**), revealing reduced expression of *RAB11FIP4* (within the aTGD

region), but not *COPRS* (outside the aTGD region). Next, we excluded the three microRNA genes that exhibited highly variable mRNA expression (**Figure 3.5H**), as well as one protein-coding gene (*ADAP2*) and one microRNA gene (*MIR4733*), which were not expressed in control hCOs. We then analyzed the differential gene expression of the seven remaining protein-coding genes at an experimentally-determined time point where the highest levels of mRNA expression were detected in control hCOs (**Figure 3.5I**).

All seven genes had reduced mRNA expression in the TGD hCOs relative to controls (**Figure 3.6B**). However, cytokine receptor-like factor 3 (*CRLF3*) was the only gene with reduced protein levels in the TGD hCOs relative to the aTGD and control hCOs (82% and 66%, respectively) (**Figure 3.6B-C, 3.5J-N**), implicating *CRLF3* in the neuronal defects observed only in TGD hCOs.

### ***CRLF3* mutation is associated with increased autism trait burden in patients with NF1**

To further investigate *CRLF3* as a potential gene involved in neurodevelopment, we evaluated *CRLF3* mutation status in a previously assembled cohort of individuals with NF1 from the Washington University NF Center. We specifically chose patients who underwent Social Responsiveness Scale, second edition (SRS-2) testing as part of routine NF1 clinical screening, had DNA banked under an approved Human Studies protocol (Constantino et al., 2015), and were between the ages of 10 and 19, based on the World Health Organization's definition of adolescence (World Health, 2017) and previously described age-dependent differences in autistic trait burden in children, adolescents, and adults with NF1 (Morris et al., 2016b). After excluding patients with CNVs ( $n = 1$ ), 17 patients were analyzed (**Table 3.2**).

Genomic DNA was whole-exome sequenced (WES) to identify genetic variants, which were prioritized according to their annotated impact (STAR Methods). A single deleterious *CRLF3* missense mutation (c.1166T>C, p.Leu389Pro) affecting a highly conserved amino acid within the *CRLF3* protein (**Figure 3.7A**) was identified in 7/17 of the NF1 patients (**Figure 3.6D**). Grouping of patients by *CRLF3* c.1166T>C mutation status revealed higher SRS-2 scores in NF1 patients with the mutation than in those without it ( $P = 0.0374$ ) (**Figure 3.6E**). The neuronal differentiation, survival, and maturation abnormalities in TGD hCOs harboring a heterozygous *CRLF3* deletion, coupled with the observed increase in autistic trait burden in patients harboring a deleterious mutation in the *CRLF3* gene, suggests an essential role for *CRLF3* in human brain development. This notion is further supported by the high amino acid sequence conservation of *CRLF3* across vertebrates (Hahn et al., 2019; Hahn et al., 2017; Ostrowski and Heinrich, 2018) and enriched *CRLF3* expression found in human embryonic brain tissues (Yang et al., 2009) (**Figure 3.7B**).

### ***CRLF3* reduction recapitulates the TGD neuronal defects**

To determine whether reduced *CRLF3* expression was responsible for the neuronal maturation defects observed in TGD hCOs, control hiPSCs were infected with four unique *CRLF3* (sh*CRLF3*) and four unique control (shCTL) short hairpin RNA constructs. All four sh*CRLF3* constructs had reduced *CRLF3* expression relative to shCTLs (**Figure 3.8A, 3.7C**). While *CRLF3* reduction had no effect on NSC proliferation (**Figure 3.8B**) or neurofibromin protein expression and subcellular localization (**Figure 3.7D-F**), it fully replicated the neuronal abnormalities observed in the TGD hCOs. In this regard, sh*CRLF3* hCOs had increased numbers



of early-stage immature neurons at 16DIV, reduced numbers of late-stage immature neurons at 35DIV (**Figure 3.8C**), increased immature neuron apoptosis (**Figure 3.8D**), reduced SMI-32<sup>+</sup> dendrites (**Figure 3.8E**) and SATB2<sup>+</sup> upper layer neurons (**Figure 3.7G**) compared to shCTL hCOs. These results demonstrate that reduced *CRLF3* expression is sufficient to produce the TGD neurogenic abnormalities, establishing *CRLF3* as a key regulator of human neuron differentiation, survival, and maturation.

### ***CRLF3*-mediated dendritic defects result from impaired RhoA activation**

To gain mechanistic insights into *CRLF3*-mediated signaling in human brain cells, we performed RNA sequencing on CTL, TGD, sh*CRLF3* and aTGD NSCs (**Figure 3.8F-G, 3.7H**). First, we identified differentially-expressed genes (DEGs; *P* values, false discover rates (FDR)  $\leq 0.01$ ; log-fold changes  $\geq \pm 5$ ) in TGD NSCs relative to CTL and aTGD NSCs. This DEG list was filtered for non-significant genes in the comparison of TGD and sh*CRLF3* NSCs (**Table 3.3**). Subsequent gene ontology (GO) enrichment analysis demonstrated  $\delta$ -catenin binding as the most highly enriched GO term (**Figure 3.8G**). Notably, dysregulation of  $\delta$ -catenin signaling has been implicated in autism (Turner et al., 2015), dendritic spine morphogenesis, maintenance and function during development (Arikkath et al., 2009; Matter et al., 2009) through regulation of N-cadherin levels (Fukata and Kaibuchi, 2001; Tan et al., 2010) and activation of Rho-family GTPases, RhoA and Rac1 (Arikkath et al., 2009; Elia et al., 2006; Gilbert and Man, 2016). To determine whether *CRLF3* regulates this pathway in cells and tissues harboring a TGD, we measured N-cadherin protein levels, as well as Rac1 and RhoA activation in CTL, TGD and sh*CRLF3* NSCs (**Figure 3.8H-K, 3.7I-K**). Consistent with this mechanism, TGD and sh*CRLF3* NSCs had reduced N-cadherin levels (TGD, 65% reduction; sh*CRLF3*, 52% reduction; **Figure**

**3.8H, 3.7I**), decreased Rac1 activation (TGD, 18.5% reduction; **Figure 3.8I**; sh*CRLF3*, 13.1% reduction; **Figure 3.7J**), and decreased RhoA activation (TGD, 76.6% reduction; **Figure 3.8J**; sh*CRLF3*, 77.1% reduction; **Figure 3.8K**) relative to controls. Moreover, treatment of TGD and sh*CRLF3* hCOs with an experimentally determined concentration of RhoA activator CN03 (**Figure 3.7K**) rescued the neuron maturation (TGD, 35.8% reduction in NeuroD1, 1.9-fold increase in NeuN; sh*CRLF3*, 57.7% reduction in NeuroD1, 2.6-fold increase in NeuN; **Figure 3.8L-M; 3.7L**), neuron apoptosis (TGD, 23% reduction; sh*CRLF3*, 17.6% reduction in Cl. Caspase-3; **Figure 3.8N; 3.7M**) and dendrite maturation defects (TGD, 2.5-fold increase; sh*CRLF3*, 2.6-fold increase in SMI-32 immunopositivity; **Figure 3.8O; 3.7N**) to control levels in 35DIV hCOs. These results establish reduced RhoA signaling as the etiologic mechanism responsible for the impaired neuron maturation and neurite outgrowth in TGD hCOs.

### 3.6 Figures and tables

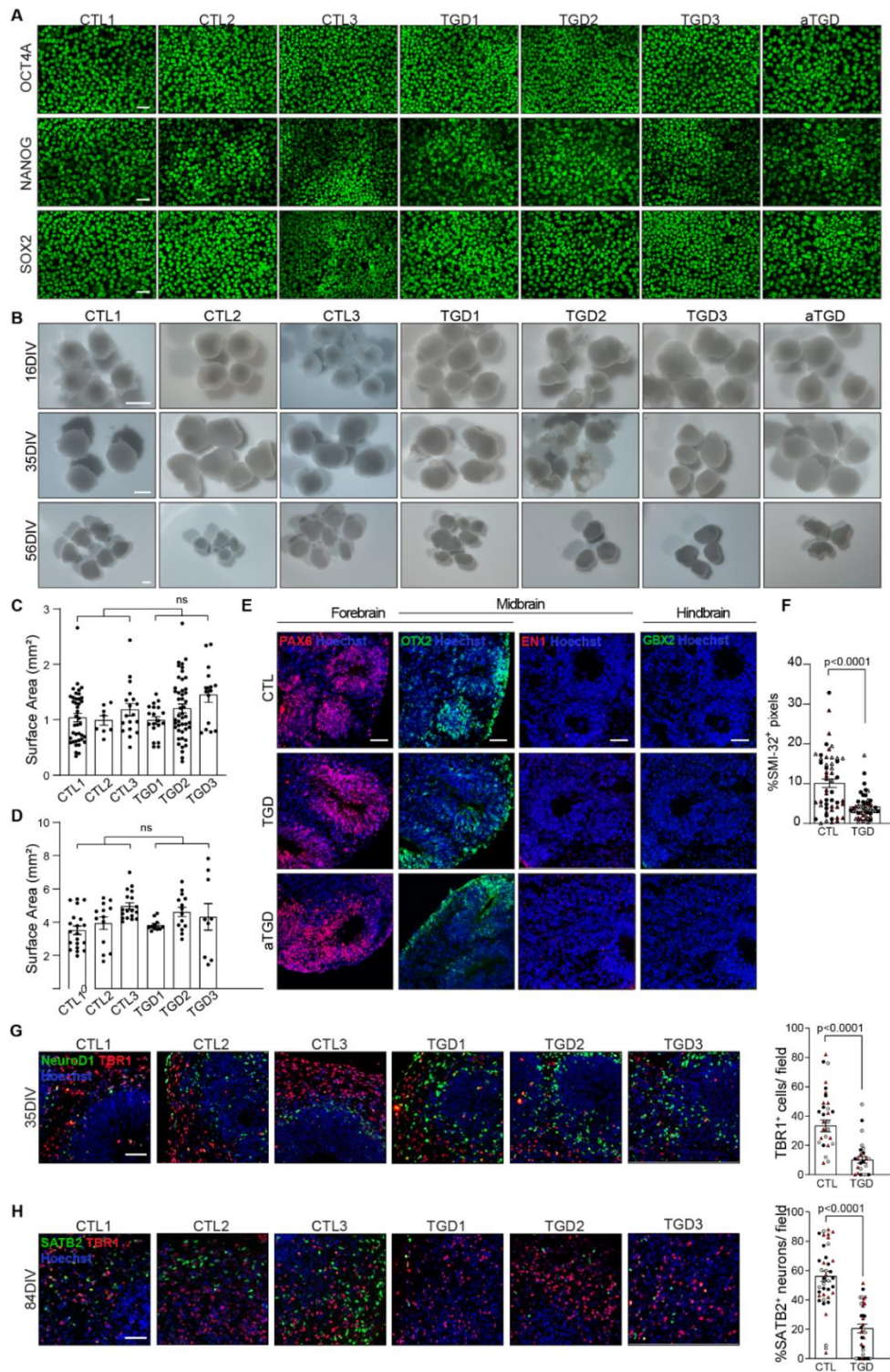


### Figure 3.1 | Patient-derived hiPSCs and hCOs.

(A) Representative images of hiPSCs immunolabeled for pluripotency markers OCT4A, NANOG, and SOX2. Scale bars: 50  $\mu\text{m}$ . (B) Representative bright-field images of hCOs at 16, 35 and 56DIV. Scale bars: 1 mm. (C-D) Quantification of surface areas of hCOs at (C) 16DIV and (D) 84DIV. (E) Representative immunofluorescence images of 16DIV CTL (CTL1), TGD (TGD1) and aTGD hCOs immunolabeled for dorsal forebrain (PAX6, OTX2), midbrain (OTX2, EN1) and hindbrain (GBX2) markers. Scale bars: 50  $\mu\text{m}$ . (F) (related to **Figure 3.2I**) Quantitation of SMI-32<sup>+</sup> immunopositive dendrites in 35DIV TGD relative to CTL hCOs. (G) Representative images of 35DIV CTL and TGD hCOs immunolabeled for early-stage immature neurons (NeuroD1) and deep-layer cortical neurons (TBR1) and quantification of the number of TBR1<sup>+</sup> deep-layer neurons per image field in hCOs at 35DIV. (H) Representative images of 84DIV CTL and TGD hCOs immunolabeled for deep-layer (TBR1) and upper-layer (SATB2) neurons and quantification of %SATB2<sup>+</sup> upper-layer neurons in hCOs at 84DIV. Scale bars, 100  $\mu\text{m}$ . Independent hiPSC lines representing three different CTL or TGD lines (black, CTL1 / TGD1; white, CTL2 / TGD2; red, CTL3 / TGD3) are shown. Data are expressed as the mean  $\pm$  SEM. Each data point represents one hCO, 2-6 hCOs per experimental replicate, 3-5 experimental replicates per genotype. Statistical analysis by unpaired, two-tailed *t*-test or one-way ANOVA with Bonferroni multiple comparisons test.

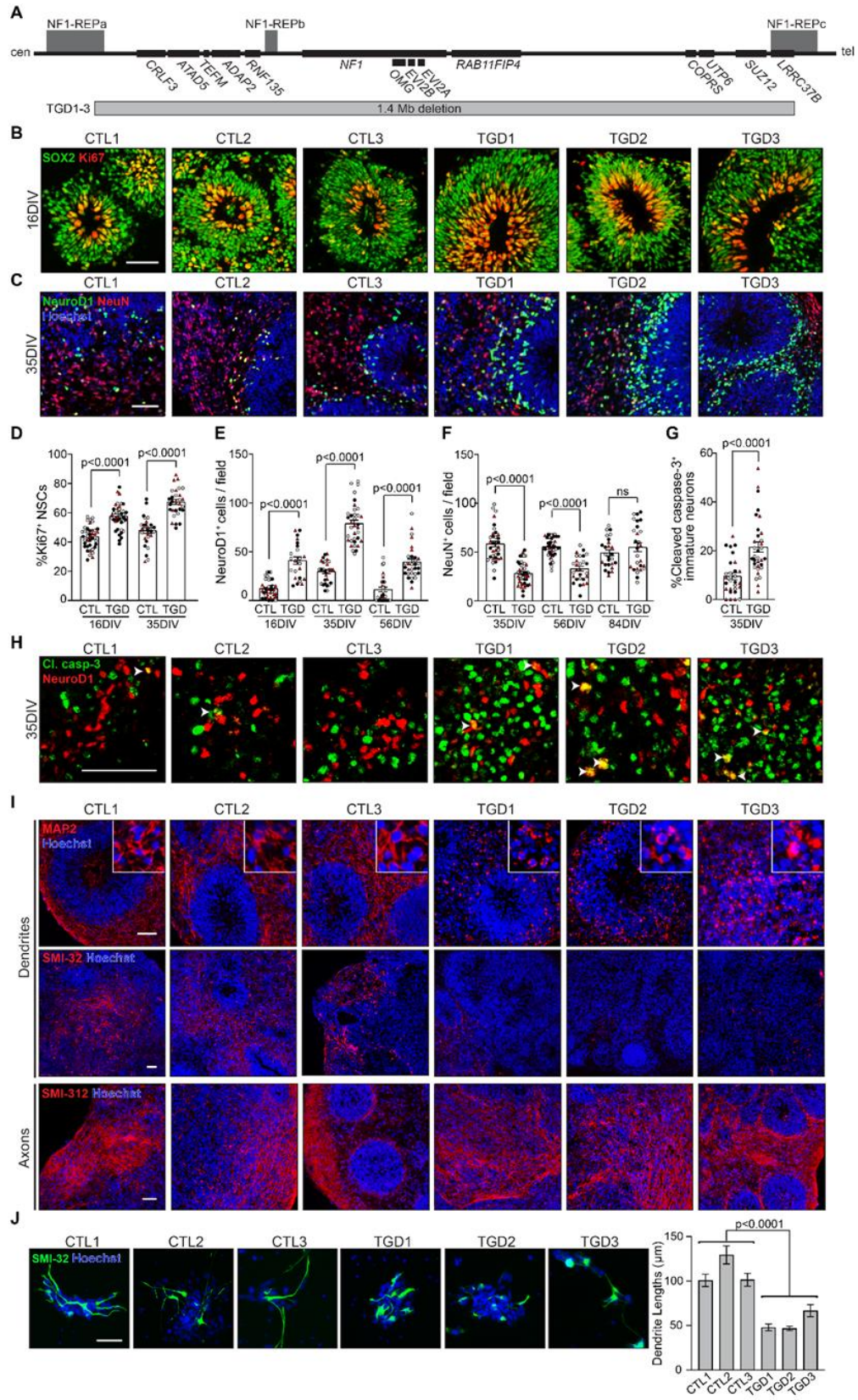


**Figure 3.2 | TGD hCOs and neurons exhibit neuronal defects.**

(A) Protein-coding genes within the 17q11.2 microdeletion region, denoting the length and location of the 1.4 Mb deletion (adapted (Kehrer-Sawatzki et al., 2017)). (B, D) Images and quantification of VZ NSC proliferation (Ki67<sup>+</sup>, red) in control (CTL) and TGD hCOs at 16 and 35DIV. (C) Images of 35DIV hCOs immunolabeled for NeuroD1<sup>+</sup> (green) and NeuN<sup>+</sup> (red) neuronal markers. (E-F) Number of (E) NeuroD1<sup>+</sup> and (F) NeuN<sup>+</sup> neurons per image field in the SVZs of TGD hCOs relative to CTL. (G) Increased apoptotic immature neurons in TGD hCOs compared to CTL at 35DIV. (D-G) Each data point represents one hCO, 2-6 hCOs per experimental replicate, 3-5 experimental replicates per genotype. Independent hiPSC lines representing three different CTL or TGD lines (black, CTL1/ TGD1; white, CTL2/ TGD2; red, CTL3/ TGD3) are shown. (H) White arrowheads indicate co-localization of NeuroD1<sup>+</sup> neurons (red) and cleaved caspase-3 (green) in CTL and TGD hCOs at 35DIV. (I) Images of hCOs immunolabeled for dendrites (MAP2<sup>+</sup>, SMI-32<sup>+</sup>) and axons (SMI-312<sup>+</sup>) at 35DIV. (J) Images of 2D CTL and TGD neurons immunolabeled for SMI-32, with a graph depicting the mean dendrite lengths per genotype. Three independent experimental replicates per genotype, 48-112 neurites per replicate. Data are shown as the mean  $\pm$  SEM. Statistical analyses by unpaired, (D-G) two-tailed *t*-test or (J) one-way ANOVA. Scale bars: B-I: 50 $\mu$ m, J: 100 $\mu$ m.

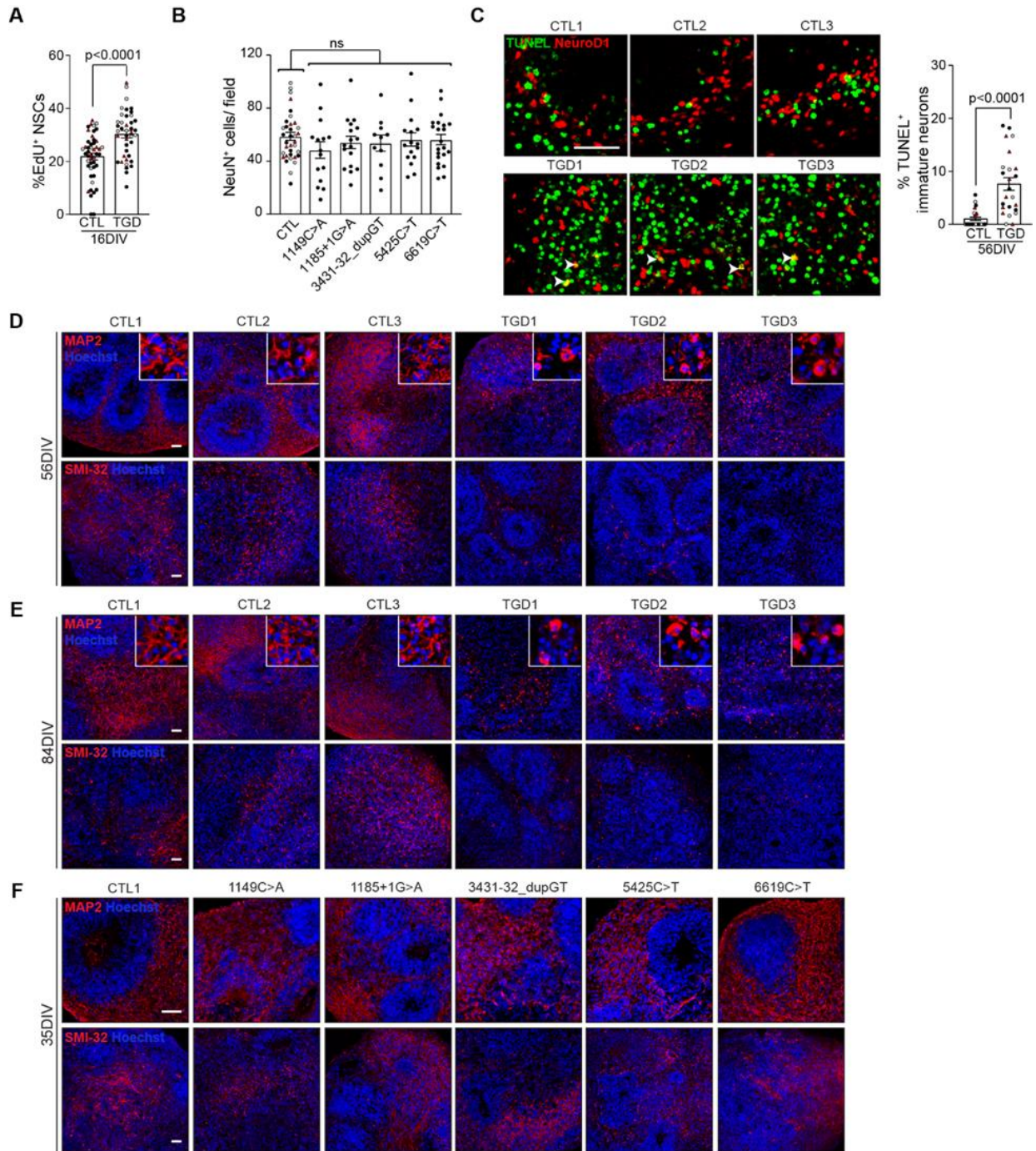


**Figure 3.3 | Neuronal differentiation defects in TGD and intragenic *NFI*-mutant hCOs.**

(A) %EdU<sup>+</sup> neural stem cells (NSCs) in 16DIV CTL and TGD hCOs. (B) Quantification of late-stage immature (NeuN<sup>+</sup>) neurons per image field in the SVZ of intragenic *NFI*-mutant hCOs

relative to CTL hCOs at 35DIV. (C) Representative images and quantification of CTL and TGD hCOs immunolabeled for TUNEL (green) and NeuroD1 (red) (co-localization indicated by white arrows) at 56DIV. (A-C) Independent hiPSC lines (black, CTL1 / TGD1; white, CTL2 / TGD2; red, CTL3 / TGD3) are shown. (D-E) Representative images of CTL and TGD hCOs immunolabeled for MAP2<sup>+</sup> and SMI-32<sup>+</sup> dendrites at (D) 56DIV and (E) 84DIV. (F) Representative control (CTL1) and intragenic *NFI*-mutant hCOs immunolabeled for dendrite-specific markers (MAP2<sup>+</sup>, SMI-32<sup>+</sup>) at 35DIV. Data are shown as the mean  $\pm$  SEM. Each data point represents one biological replicate (hCO), 2-6 biological replicates per experimental replicate, 3-5 experimental replicates per genotype. Statistical analysis by unpaired, two-tailed *t*-test or one-way ANOVA with Dunnett's multiple comparisons test. Scale bars: 50  $\mu$ m.



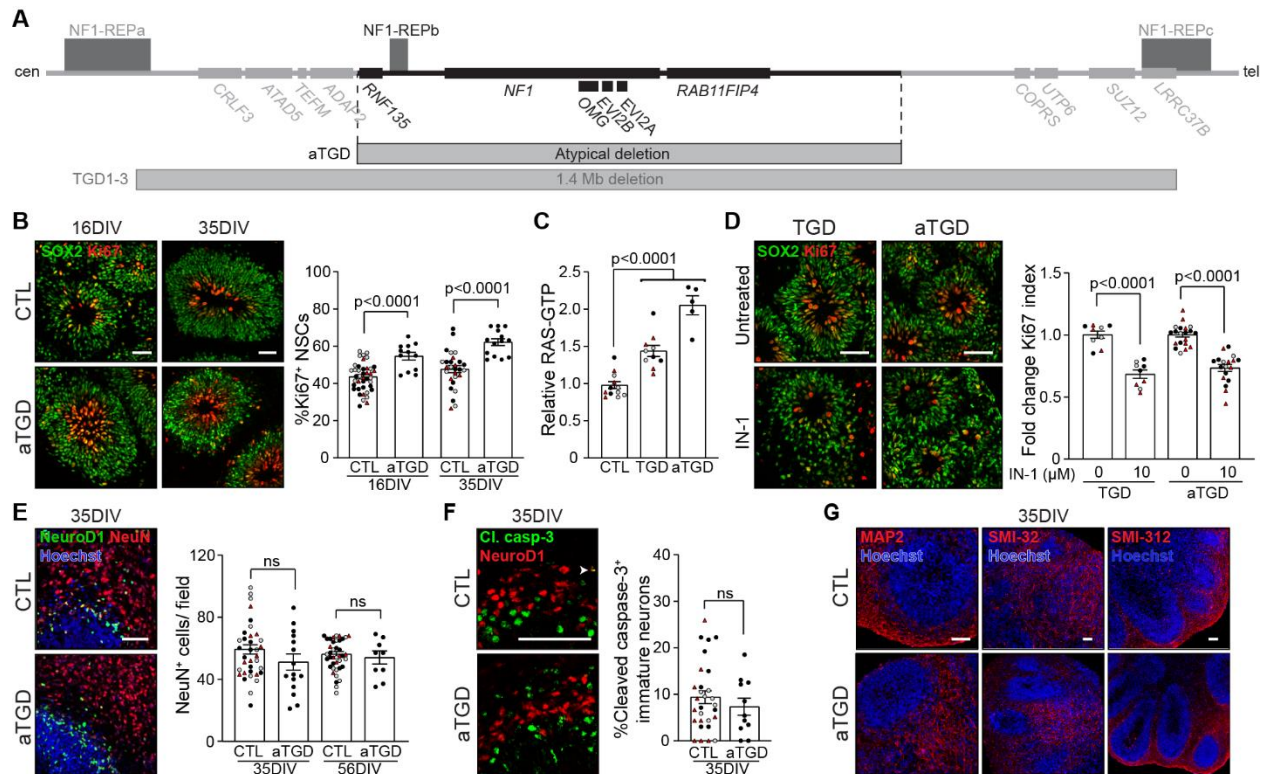


**Figure 3.4 | RAS hyperactivation drives the increased NSC proliferation in TGD hCOs.**

(A) Diagram illustrating the 1.4 Mb (TGD) and atypical (aTGD) microdeletions, highlighting their commonly deleted region. (B) Images and quantification of NSC (SOX2<sup>+</sup>) proliferation (Ki67<sup>+</sup>) in CTL and aTGD hCOs at 16 and 35DIV. (C) TGD and aTGD hCOs have increased RAS activity relative to CTL hCOs at 16DIV. Each data point represents an independent experimental replicate consisting of 4 pooled hCOs. (D) Images and quantification of NSC proliferation (fold change in %Ki67<sup>+</sup> NSCs) in three clones of TGD and aTGD hCOs at 16DIV with or without IN-1 treatment. (E-G) Images and quantification of CTL and aTGD hCOs showing normal (E) production of NeuN<sup>+</sup> neurons at 35 and 56DIV, (F) early-stage immature neuron apoptosis, and (G) production of dendrites (MAP2<sup>+</sup>, SMI-32<sup>+</sup>) and axons (SMI-312<sup>+</sup>) at 35DIV. (B, D-F) Each data point represents one hCO, 2-6 hCOs per experimental replicate, 3-5

experimental replicates per genotype. Independent hiPSC lines representing three different CTL or aTGD lines (black, CTL1/ aTGD1; white, CTL2/ aTGD2; red, CTL3/ aTGD3) are shown. All data are shown as the mean  $\pm$  SEM. Statistical analysis by one-way ANOVA with Dunnett's multiple comparisons test or unpaired, two-tailed *t*-test. Scale bars: 50 $\mu$ m.

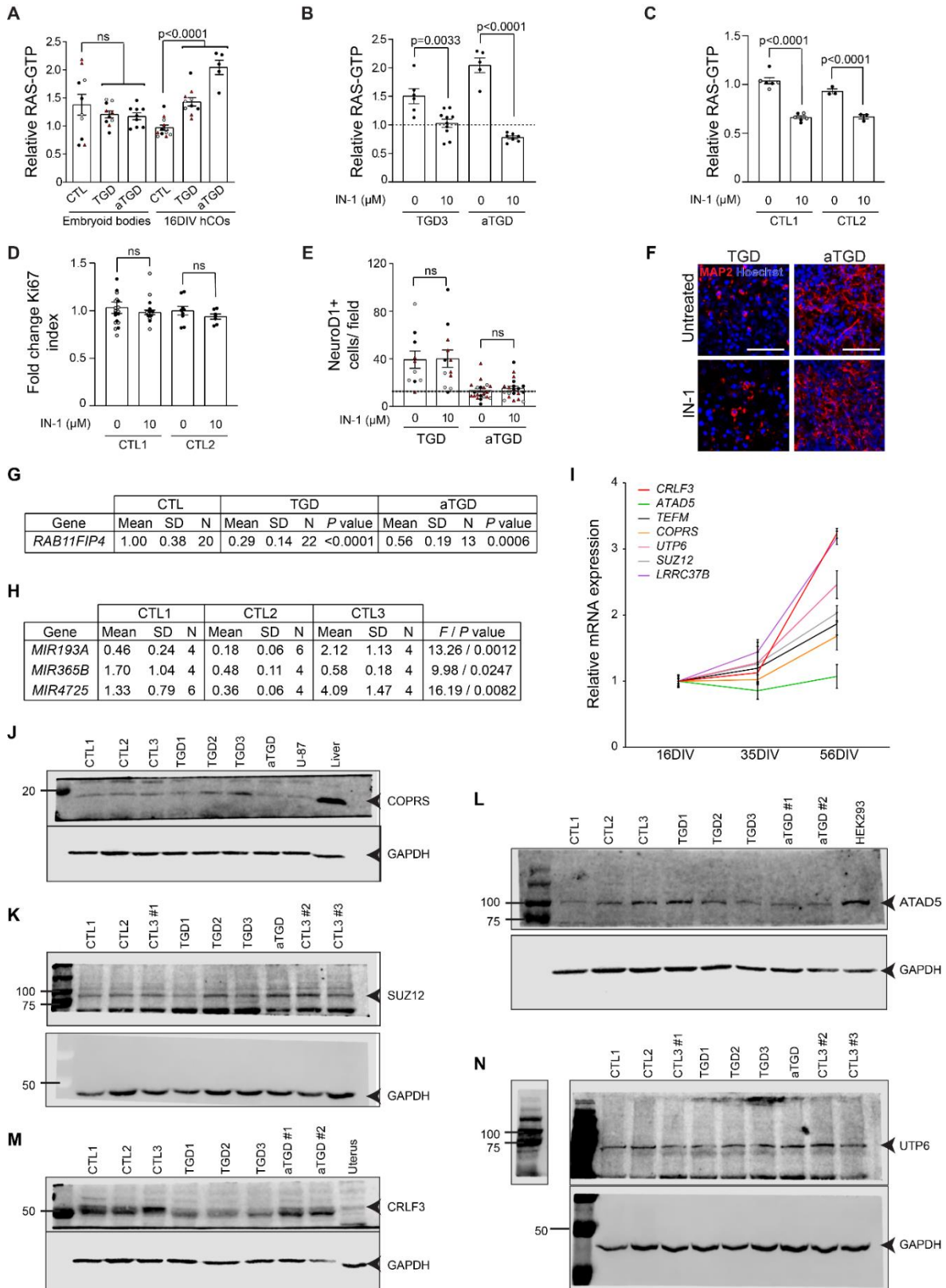


**Figure 3.5 | RAS activity and differential gene expression analysis of TGD and CTL hCOs.**

(A) RAS activation in CTL and TGD 8DIV embryoid bodies and 16DIV hCOs. (B-C) Reduced RAS activity in (B) TGD3 and aTGD 16DIV hCOs and (C) CTL1 and CTL2 hCOs following 10  $\mu$ M pan-RAS-IN-1 (IN-1) treatment. The mean CTL hCO RAS activity was assigned a value of 1 (dotted line). (A-C) Each data point represents an independent experimental replicate consisting of 20 pooled embryoid bodies or 4 pooled hCOs. Statistical analysis by unpaired, two-tailed *t*-test or one-way ANOVA with Dunnett's multiple comparisons. (D) Quantification of NSC proliferation (fold change in %Ki67<sup>+</sup> NSCs) in control hCOs at 16DIV with or without IN-1 treatment. Each data point represents one hCO, 2-6 hCOs per experimental replicate, 3-5 experimental replicates per genotype. Statistical analysis by unpaired, two-tailed *t*-test. (E) Number of early-stage immature (NeuroD1<sup>+</sup>) neurons per image field in the SVZ of 16DIV TGD3 and aTGD hCOs with and without IN-1 treatment. Each data point represents one hCO, 3-12 hCOs per clone. Statistical analysis by unpaired, two-tailed *t*-test comparing TGD3 and aTGD hCOs with control values (indicated by dotted line). (A-E) All data are shown as the mean  $\pm$  SEM. Independent (A, E) hiPSC lines (black, CTL1 / TGD1 / aTGD1; white, CTL2 / TGD2 / aTGD2; red, CTL3 / TGD3, aTGD-3), or (C-D) independent hiPSC clones (black, clone 1; white, clone 2; red, clone 3) are shown. (F) Representative images of 16DIV TGD3 and aTGD hCOs with and without RAS-IN-1 treatment immunolabeled for MAP2<sup>+</sup> dendrites. Scale bars: 50  $\mu$ m. (G) mRNA expression of *RAB11FIP4* in 56DIV hCOs showing gene deletion status in TGD1-3 and aTGD. Statistical analysis by unpaired, two-tailed *t*-test. (H) RT-qPCR analysis of microRNA gene expression in CTL hCOs at the time point of highest expression (16DIV). Statistical analysis by one-way ANOVA; *F*-ratio / *P* values reported. *MIR4733* was not expressed in CTL hCOs. Each mRNA expression data point represents one biological replicate

(hCO), 2-3 hCOs per experimental replicate. **(I)** Time course analysis of mRNA expression in 16, 35 and 56DIV CTL hCOs for 7 protein-coding genes included in differential gene expression analysis, illustrating highest transcript expression levels for 6 of the 7 genes at 56DIV. *ATAD5* had no change in expression over time. Each time point represents 2 independent experimental replicates of CTL1 hCOs with each experimental replicate containing 2 biological replicates (hCOs). Data are shown as the mean  $\pm$  SEM. **(J-N)** Representative unprocessed western blots of CTL and TGD protein expression including **(J)** COPRS, **(K)** SUZ12, **(L)** ATAD5, **(M)** CRLF3 and **(N)** UTP6.

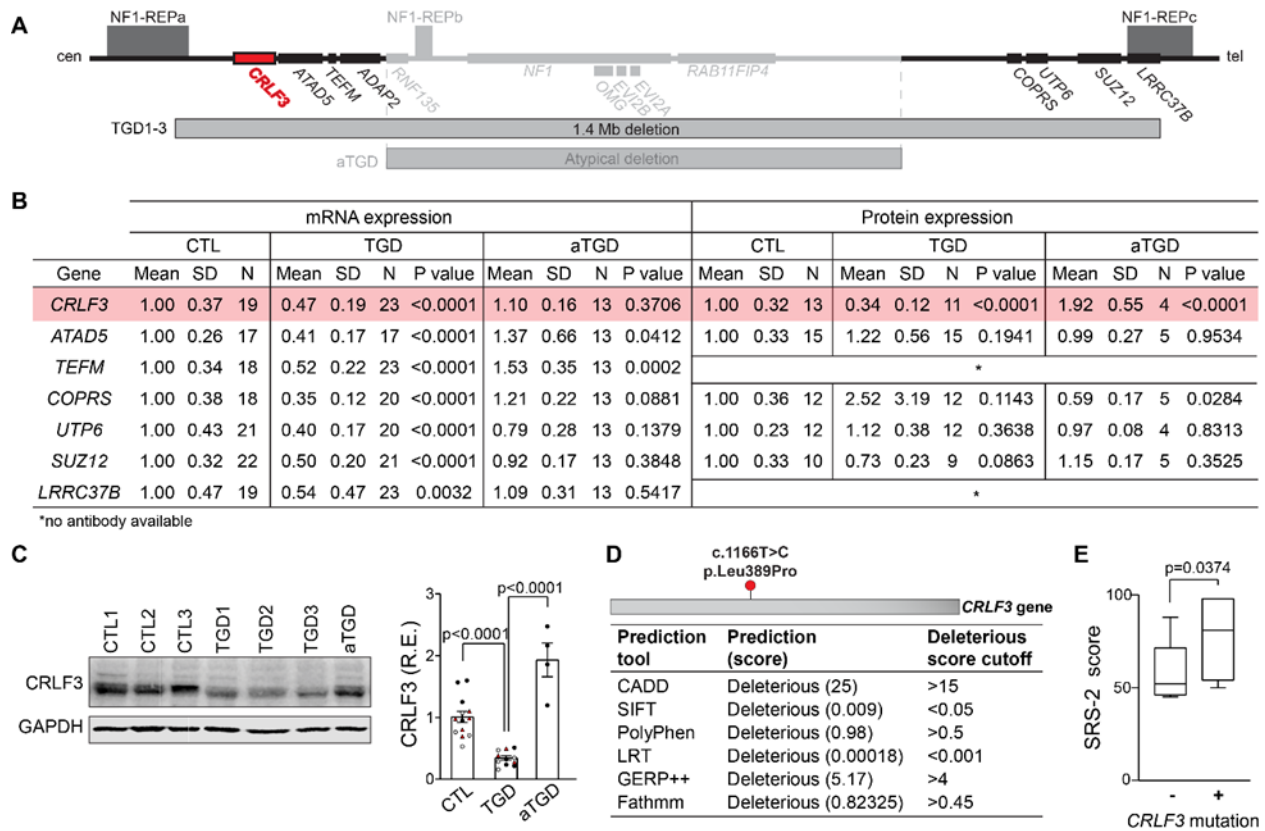


**Figure 3.6 | *CRLF3* is uniquely disrupted in TGD hCOs and NF1 patients with increased SRS-2 scores.**

(A) 17q11.2 region highlighting the loci uniquely deleted in TGD microdeletions and the *CRLF3* gene (red). (B) mRNA and protein expression analysis at 56DIV of protein-coding genes uniquely deleted in TGD hCOs. Each mRNA data point represents 1 hCO, 3 hCOs per experimental replicate. Each protein data point represents an independent replicate consisting of 4 pooled hCOs. (C) Western blot and quantification demonstrating reduced *CRLF3* protein levels in TGD relative to CTL and aTGD 56DIV hCOs. Data are shown as the mean  $\pm$  SEM. Independent hiPSC lines representing three different CTL or TGD lines (black, CTL1/ TGD1; white, CTL2/ TGD2; red, CTL3/ TGD3) are shown. (D) Position of the deleterious *CRLF3*

c.1166T>C mutation found in 7/17 NF1 patients, with mutational effect predictions using six methods. **(E)** NF1 patients with the *CRLF3* c.1166T>C mutation ( $n=7$ ) have higher SRS-2 scores than those without it ( $n=10$ ). Box plot indicates median (central line), interquartile range (box) and minimum and maximum values (whiskers). **(C, E)** Statistical analysis by unpaired, two-tailed  $t$ -test.

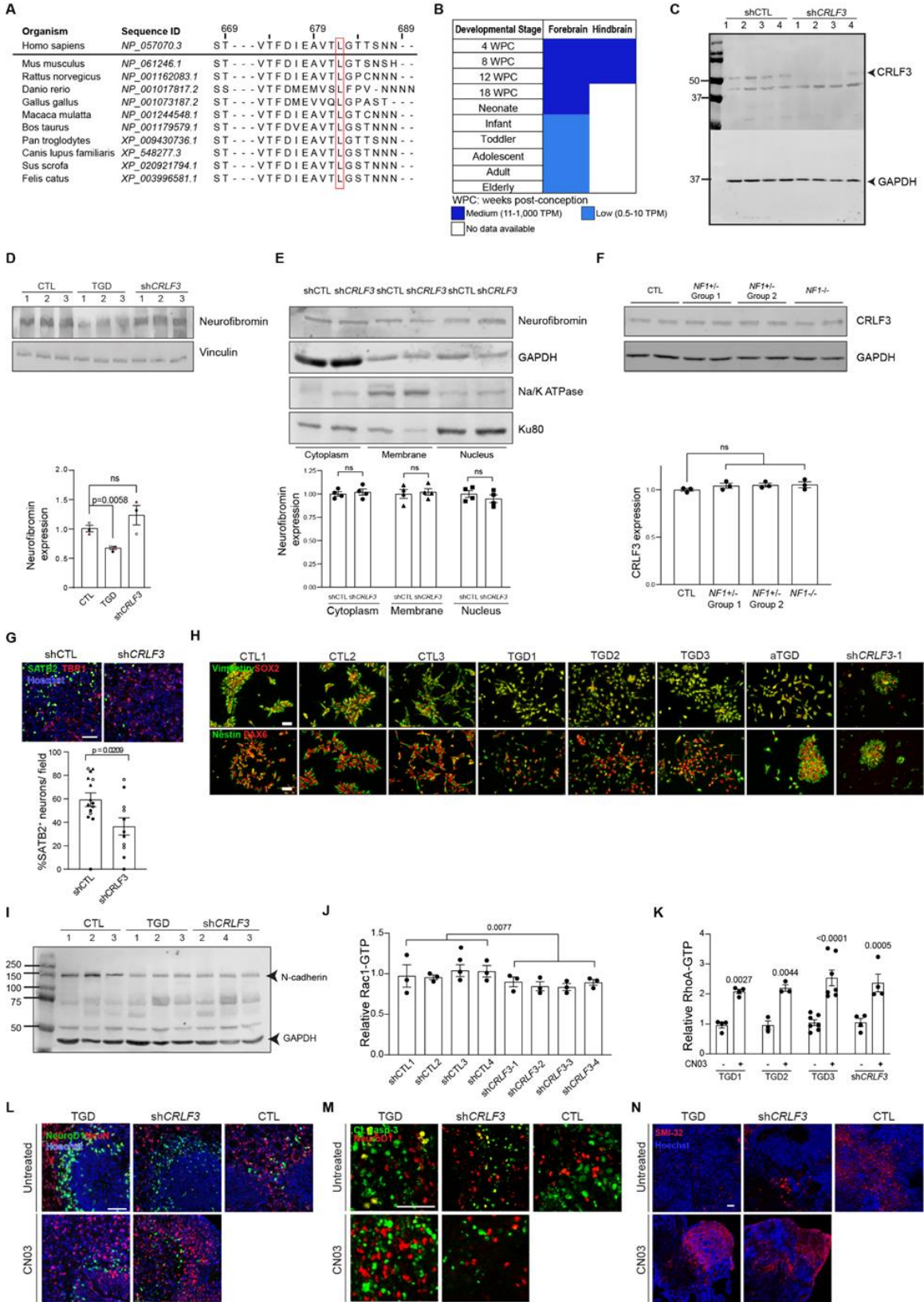




**Figure 3.7 | *CRLF3* sequence conservation, developmental expression, and downstream signaling.**

(A) Amino acid sequence alignments revealed 92.8% conservation in p.Leu389 between human and 303 vertebrate *CRLF3* orthologs. Ten representative orthologs from NCBI's Eukaryotic Genome Annotation pipeline are shown, with p.Leu389 outlined in red. (B) Heat map of *CRLF3* mRNA expression levels in the human forebrain and hindbrain at different developmental stages, as reported by the Expression Atlas: Human RNA-seq time-series of the development of seven major organs. TPM: transcripts per million. (C) Uncropped western immunoblot from **Figure 3.8A**. (D) Neurofibromin relative expression in CTL, TGD, and sh*CRLF3* hiPSC-derived NSCs. Independent hiPSC lines (black, CTL1 / TGD1 / sh*CRLF3*-1; white, CTL2 / TGD2 / sh*CRLF3*-2; red, CTL3 / TGD3 / sh*CRLF3*-3) are shown. Statistical analysis by unpaired, two-tailed *t*-test. (E) Immunoblots and quantitation of neurofibromin expression in different subcellular fractions (cytoplasm, membrane, nucleus) in shCTL and sh*CRLF3* NPCs. GAPDH (cytoplasm), Na/K ATPase (membrane) and human-specific Ku80 (nucleus) were used as loading controls. (F) Immunoblot and quantitation of *CRLF3* expression in NPCs harboring *NF1* point mutations, either conferring <30% reduced (Group 1), or >70% reduced (Group 2) neurofibromin levels, NPCs harboring homozygous null *NF1* mutations (*NF1*<sup>-/-</sup>), or non-mutant controls. GAPDH was used as a loading control. (E-F) Data are expressed as the mean ± SEM. Statistical analysis by (E) unpaired, two-tailed *t*-test or (F) one-way ANOVA with Bonferroni post-test correction. ns, not significant. (G) Representative images of 84DIV shCTL and sh*CRLF3* hCOs immunolabeled for deep-layer (TBR1) and upper-layer (SATB2) neurons and quantification of %SATB2<sup>+</sup> upper-layer neurons in hCOs at 84DIV. Scale bar: 100 μm. (H) hiPSC-derived NSCs immunolabeled for NSC markers SOX2, Vimentin, Nestin and PAX6. Scale bar: 50μm. (I) Unprocessed western

immunoblot from **Figure 3.8H**. **(J)** Rac1 activity levels in shCTL and sh*CRLF3* NSCs. Each data point represents individual NSC sample. Statistical analysis by unpaired, two-tailed *t*-test. **(K)** RhoA activity in 2DIV TGD and sh*CRLF3* hCOs with and without 1  $\mu\text{g/mL}$  CN03 RhoA activator (CN03) treatment for 24 hours. Each data point represents 6 pooled hCOs. Statistical analysis by two-way ANOVA with Sidak's multiple comparison test performed comparing untreated with treated hCOs. All data are shown as the mean  $\pm$  SEM and the *P* values are shown above each bar. **(L-N)** Representative images of **(L)** NeuroD1<sup>+</sup> (green)/ NeuN<sup>+</sup> (red) neurons, **(M)** cleaved caspase-3<sup>+</sup> apoptotic immature neurons and **(N)** SMI-32<sup>+</sup> dendrites in 35DIV CTL, TGD and sh*CRLF3* hCOs with and without CN03 treatment. Scale bars: 50  $\mu\text{m}$ .

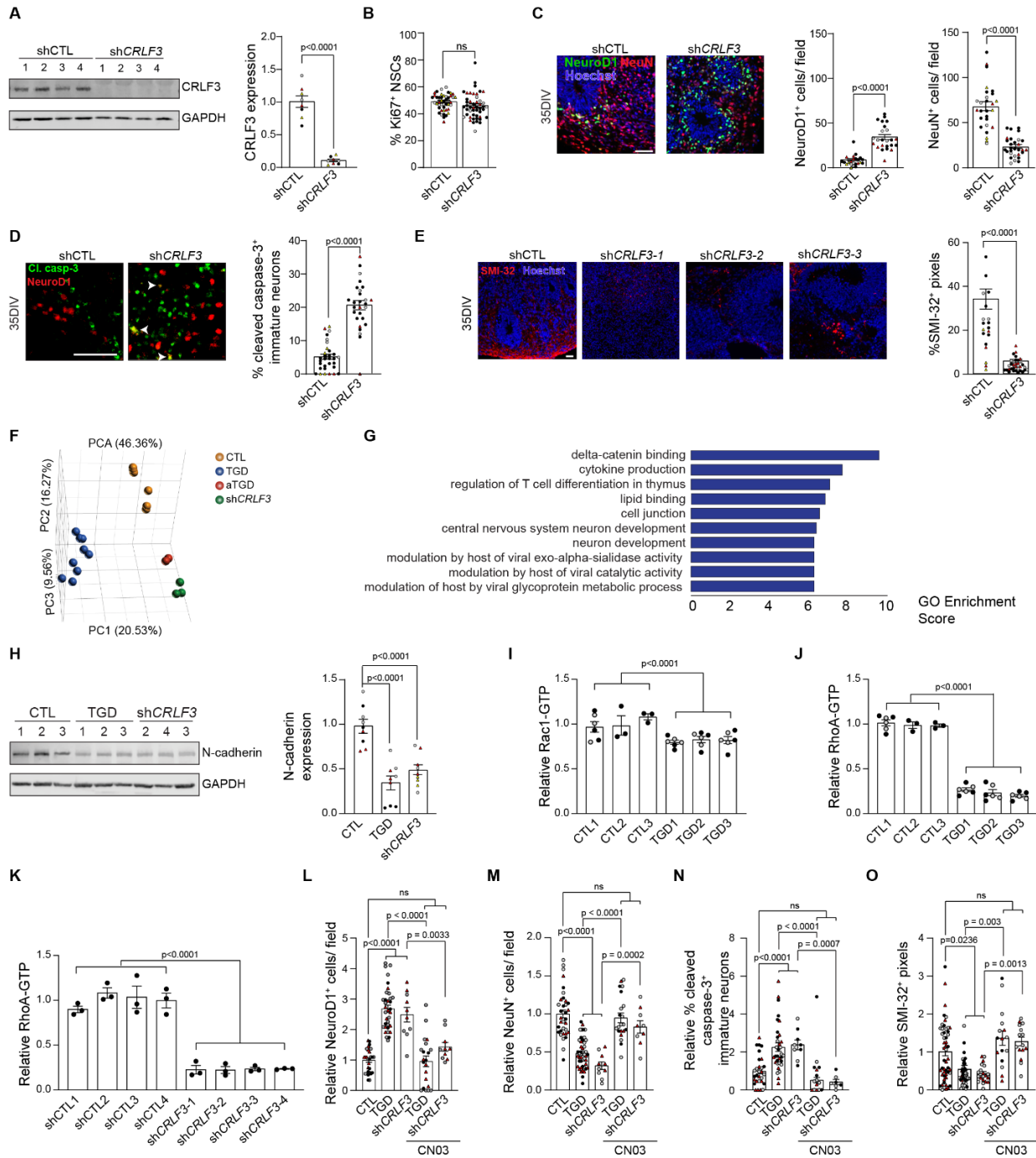


**Figure 3.8 | Impaired RhoA signaling drives *CRLF3*-mediated neuronal defects.**

(A) Western blot showing reduced *CRLF3* protein levels in CTL1 hiPSCs infected with *shCRLF3* constructs relative to *shCTL*. (B) NSC proliferation (%Ki67<sup>+</sup> NSCs) in 16DIV hCos

from shCTL and sh*CRLF3* lines. **(C-E)** Images and quantification of shCTL and sh*CRLF3* hCOs showing **(C)** increased production of NeuroD1<sup>+</sup> (green) neurons and reduced NeuN<sup>+</sup> (red) neurons, **(D)** increased apoptotic (Cl. casp-3, green) immature (NeuroD1, red) neurons, and **(E)** reduced SMI-32<sup>+</sup> dendrites in sh*CRLF3* compared to shCTL hCOs. **(C-E)** Each data point represents one hCO, 3-10 hCOs per hiPSC line. Statistical analysis by unpaired, two-tailed *t*-test. **(F)** Principal component analysis showing distinct transcriptional profiles in CTL, TGD, aTGD, and sh*CRLF3* NSCs. **(G)** Enrichment scores of the top 10 gene ontologies (*P* value ≤ 0.01) in sh*CRLF3* and TGD relative to CTL and aTGD NSCs. **(H)** Western blot and quantification of N-cadherin protein levels in CTL, TGD, and sh*CRLF3* NSCs. *n* = 3 biological replicates per genotype. Statistical analysis by one-way ANOVA with Dunnett's multiple comparisons test. **(I)** Rac1 and **(J-K)** RhoA activity levels in **(I-J)** CTL and TGD or **(K)** shCTL and sh*CRLF3* NSCs. **(I-K)** Each data point represents an independently generated biological replicate, 3 biological replicates per genotype. Statistical analysis by unpaired, two-tailed *t*-test. **(L-O)** Quantitation of **(L)** NeuroD1<sup>+</sup> neurons, **(M)** NeuN<sup>+</sup> neurons, **(N)** cl. caspase-3<sup>+</sup> apoptotic immature neurons and **(O)** SMI-32<sup>+</sup> immunopositive dendrites in 35DIV TGD and sh*CRLF3* hCOs with and without CN03 treatment relative to control hCOs. Data are represented as fold-change relative to controls. Each data point represents one hCO, 2-6 hCOs per experimental replicate, 3-5 experimental replicates per genotype. **(A-O)** All data are shown as the mean ± SEM. Independent hiPSC lines representing **(A-E)** four different shCTL or sh*CRLF3* lines (black, shCTL1 / sh*CRLF3*-1; white, shCTL2 / sh*CRLF3*-2; red, shCTL3 / sh*CRLF3*-3; yellow, shCTL4 / sh*CRLF3*-4), **(H, L-O)** three different CTL, TGD or sh*CRLF3* lines (black, CTL1 / TGD1 / sh*CRLF3*-1; white CTL2 / TGD2 / sh*CRLF3*-2; red, CTL3 / TGD3 / sh*CRLF3*-3), or **(I, J)** two different clones for each line (black, clone 1; grey, clone 2) are shown. Scale bars: 50 μm.

**Table 3.1 | Patient-derived CTL1-3, TGD1-3 and aTGD (atypical TGD) hiPSC lines and isogenic hiPSC lines CRISPR/Cas9-engineered to harbor NF1 patient *NF1* gene mutations.**

Genotype	Sex	Age (years)	Specimen source	No. clones
CTL1 <sup>a</sup>	Male	Fetal	Skin biopsy	2
CTL2 <sup>b</sup>	Male	27	Skin biopsy	1
CTL3 <sup>c</sup>	Male	41	Skin biopsy	1
TGD1	Male	44	Skin biopsy	2
TGD2	Male	6	Urine	2
TGD3	Male	11	Blood	3
aTGD	Female	16	Blood	3
NF1 patient mutation	Protein level		Mutation Type	No. clones
c.1149C>A	p.Cys383X		Nonsense	2
c.1185+1G>A	p.Asn355_Lys395del		Splice site	2
c.3431-32_dupGT	p.Thr1145Val_FS		Frameshift	2
c.5425C>T	p.Arg1809Cys		Missense	2
c.6619C>T	p.Gln2207X		Nonsense	1

<sup>a</sup>BJFF.6 commercially available

<sup>b</sup>Dr. Matthew B. Harms (WUSM)

<sup>c</sup>Dr. Fumihiko Urano (WUSM)

**Table 3.2 | Human genomic DNA whole-exome sequencing.**

<b>Patient ID</b>	<b>SRS-2</b>	<b>Age (years)</b>	<b>Sex</b>	<b><i>CRLF3</i>-mutation</b>	<b><i>NF1</i>-mutation</b>
OtB3317	81	10	M	c.1166T>C	c.5305C>T
OtC6610	48	11	F		c.3137_3138delCA
OtB3335	64	11	M		c.1756_1759delACTA
OtB3325	45	11	F		c.3888T>G
OtC6607	70	11	F		c.3449C>T
OtB3313	98	13	M	c.1166T>C	c.7255_7256delCT
OtC6614	48	13	M		c.2965G>T
OtC6612	50	13	M	c.1166T>C	c.910C>T
OtB3333	91	13	M	c.1166T>C	c.204+1G>T
OtB3326	54	15	F	c.1166T>C	c.2125T>C
OtB3321	88	15	M		c.6855C>A
OtB3312	98	15	M	c.1166T>C	c.4514delG
OtC6619	46	16	F		c.4006C>T
OtC6615	76	16	M		c.205-19T>A
OtB3319	74	16	F	c.1166T>C	c.4985G>A
OtB3323	56	17	M		c.1885G>A
OtB3336	46	18	M		c.3520C>T

**Table 3.3 | Differentially expressed gene list filtered for non-significant genes in the comparison of TGD vs shCRLF3 samples.**

<b>Gene symbol</b>	<b>P value (TGD vs. shCRLF3)</b>	<b>FDR step up (TGD vs. shCRLF3)</b>	<b>Fold change (TGD vs. shCRLF3)</b>
<i>KCP</i>	0.1073	0.1689	2.99
<i>SPN</i>	0.2332	0.3201	2.90
<i>THSD7A</i>	0.0109	0.0248	2.84
<i>MMP23B</i>	0.0177	0.0373	2.67
<i>ACOT11</i>	0.0456	0.0826	2.25
<i>ASCL1</i>	0.9106	0.9346	1.82
<i>DACT1</i>	0.0700	0.1184	1.75
<i>LDHAP4</i>	0.7063	0.7715	1.29
<i>ADGRE5</i>	0.7043	0.7696	1.25
<i>RUBCNL</i>	0.8635	0.8992	1.20
<i>NEFM</i>	0.5160	0.6030	1.13
<i>EPB41L4A</i>	0.9420	0.9570	-1.09
<i>TENM2</i>	0.2461	0.3342	-1.27
<i>MDGA2</i>	0.1567	0.2308	-1.27
<i>CAMK4</i>	0.5252	0.6119	-1.31
<i>SORBS2</i>	0.0812	0.1341	-1.64
<i>ATCAY</i>	0.1408	0.2112	-1.69
<i>PTX3</i>	0.0732	0.1229	-1.72
<i>MANEAL</i>	0.0455	0.0825	-1.78
<i>ITGB8</i>	0.0134	0.0296	-1.86
<i>DCLK2</i>	0.0091	0.0214	-1.91
<i>SYT5</i>	0.0236	0.0474	-2.25
<i>SYP</i>	0.0102	0.0234	-2.25
<i>RASGRP1</i>	0.0241	0.0481	-2.58
<i>MSI1</i>	0.0047	0.0121	-2.58
<i>CRABP1</i>	0.0052	0.0134	-2.82
<i>FCHO1</i>	0.0056	0.0142	-2.85
<i>ECEL1</i>	0.0114	0.0257	-2.90
<i>PLEKHA7</i>	0.0097	0.0225	-3.02
<i>ULBP1</i>	0.0051	0.0131	-3.43
<i>MMRN1</i>	0.0103	0.0237	-3.89

**Table 3.4 | Summary of experimental samples, replicates and statistical tests used.**

Relative to main Figure	Readout	Sample type	Assay	Quantitation	Independent CTL lines used	Independent mutant lines used	Min. times experiment performed	Min. biological replicates/line or clone	Statistical test used
Figure 1	Ki67	hCOs	IF: Figure 1B	Figure 1D	3 CTL cell lines (CTL1, CTL2, CTL3)	3 TGD cell lines (TGD1, TGD2, TGD3)	3	7	unpaired, 2-tailed t-test
	NeuroD1	hCOs	IF: Figure 1C	Figure 1E			3	8	unpaired, 2-tailed t-test
	NeuN	hCOs	IF: Figure 1C	Figure 1F			3	7	unpaired, 2-tailed t-test
	Cleaved Caspase-3	hCOs	IF: Figure 1H	Figure 1G			3	10	unpaired, 2-tailed t-test
	MAP2	hCOs	IF: Figure 1I	n/a			3	9	n/a
	SMI-32	hCOs	IF: Figure 1I	Figure 1F			3	11	unpaired, 2-tailed t-test
	SMI-312	hCOs	IF: Figure 1J	n/a			3	9	n/a
	SMI-32	2D neurons	IF: Figure 1J	Figure 1J			3	39	1-way ANOVA with Bonferroni correction
	TBR1	hCOs	IF: Figure 1G	Figure 1H			3	6	unpaired, 2-tailed t-test
	SATB2	hCOs	IF: Figure 1H	Figure 1I			3	10	unpaired, 2-tailed t-test
	Ki67	hCOs	IF: Figure 2B	Figure 2B			3	7	unpaired, 2-tailed t-test
	RAS-GTP	hCOs	ELISA: Figure 2C	Figure 2C			3	12	1-way ANOVA with Bonferroni correction
	Ki67	hCOs + IN-1	IF: Figure 2D	Figure 2D			3	12	1-way ANOVA with Bonferroni correction
	NeuroD1	hCOs	IF: Figure 2E	n/a			3	3/clone, 9/line	unpaired, 2-tailed t-test
	NeuN	hCOs	IF: Figure 2E	n/a			3	9	n/a
Figure 2	Cleaved Caspase-3	hCOs	IF: Figure 2F	Figure 2E	3	9	unpaired, 2-tailed t-test		
	MAP2	hCOs	IF: Figure 2G	Figure 2F	3	8	unpaired, 2-tailed t-test		
	SMI-32	hCOs	IF: Figure 2G	n/a	3	9	n/a		
	SMI-312	hCOs	IF: Figure 2G	n/a	3	9	n/a		
	EdU	hCOs	n/a	Figure 2A	3	8	unpaired, 2-tailed t-test		
	NeuN	hCOs	n/a	Figure 2B	3	15	1-way ANOVA with Bonferroni correction		
	TUNEL	hCOs	IF: Figure 2C	Figure 2B	3	7	unpaired, 2-tailed t-test		
	RAS-GTP	EBs	ELISA: Figure 2C	Figure 2C	3	7	unpaired, 2-tailed t-test		
	RAS-GTP	hCOs	ELISA: Figure 2C	Figure 2C	3	60	1-way ANOVA with Dunnett's multiple comparison		
	RAS-GTP	hCOs + IN-1	ELISA: Figure 2C	Figure 2C	3	12	1-way ANOVA with Dunnett's multiple comparison		
	RAS-GTP	hCOs + IN-1	ELISA: Figure 2C	Figure 2C	3	9	unpaired, 2-tailed t-test		
	Ki67	hCOs + IN-1	ELISA: Figure 2C	Figure 2C	3	12	unpaired, 2-tailed t-test		
	NeuroD1	hCOs + IN-1	n/a	Figure 2D	3	6	unpaired, 2-tailed t-test		
	CRLF3	hCOs	WB: Figure 3C	Figure 3C	3	3/clone, 10/line	unpaired, 2-tailed t-test		
	Figure 3	SRS-2 Score	patient DNA	SRS-2 analysis	Figure 3E	10 patients without CRLF3 mutation	4 (TGD1, TGD2, TGD3, atGD)	n/a	7
mRNA Expression		hCOs	mRNA expression	Figure 3E	1 CTL (CTL1)	7 patients with CRLF3 mutation	2	4	n/a
CRLF3		shCRLF3 hiPSCs	WB: Figure 4A	Figure 3I	4 shCTL	n/a	3	4	unpaired, 2-tailed t-test
Ki67		shCRLF3 hCOs	n/a	Figure 4A	4 shCTL	4 shCRLF3	3	4	unpaired, 2-tailed t-test
NeuroD1		shCRLF3 hCOs	IF: Figure 4C	Figure 4B	4 shCTL	4 shCRLF3	3	9	unpaired, 2-tailed t-test
NeuN		shCRLF3 hCOs	IF: Figure 4C	Figure 4C	4 shCTL	4 shCRLF3	3	4	unpaired, 2-tailed t-test
Cleaved Caspase-3		shCRLF3 hCOs	IF: Figure 4E	Figure 4D	4 shCTL	4 shCRLF3	3	4	unpaired, 2-tailed t-test
SMI-32		shCRLF3 hCOs	IF: Figure 4E	Figure 4E	4 shCTL	4 shCRLF3	3	3	unpaired, 2-tailed t-test
N-cadherin		NSCs	WB: Figure 4H	Figure 4E	3 CTL	4 shCRLF3	3	3	unpaired, 2-tailed t-test
Rac1-GTP		NSCs	ELISA: Figure 4I	Figure 4F	3 CTL	6 (3 TGD, 3 shCRLF3)	3	3	1-way ANOVA with Bonferroni correction
RhoA-GTP		NSCs	ELISA: Figure 4J	Figure 4I	3 CTL	3 TGD	3	3/clone, 3/line	unpaired, 2-tailed t-test
NeuroD1		hCOs + CN03	IF: Figure 4L	Figure 4J	3 CTL	3 TGD	3	3	unpaired, 2-tailed t-test
NeuroD1		hCOs + CN03	IF: Figure 4L	Figure 4K	3 CTL	4 shCRLF3	3	3	unpaired, 2-tailed t-test
Cleaved Caspase-3		hCOs + CN03	IF: Figure 4M	Figure 4L	3 CTL	3 TGD, 2 shCRLF3	3	5	1-way ANOVA with Tukey multiple comparison
SMI-32		hCOs + CN03	IF: Figure 4M	Figure 4M	3 CTL	3 TGD, 2 shCRLF3	3	4	1-way ANOVA with Tukey multiple comparison
Neurofibromin	NSCs	WB: Figure 4D	Figure 4N	3 CTL	3 TGD, 2 shCRLF3	3	3	unpaired, 2-tailed t-test	
Neurofibromin	NSCs	WB: Figure 4E	Figure 4D	3 shCTL	3 TGD, 3 shCRLF3	3	3	unpaired, 2-tailed t-test	
CRLF3	NSCs	WB: Figure 4F	Figure 4E	3 shCTL	3 shCRLF3	3	3	unpaired, 2-tailed t-test	
SATB2	shCRLF3 hCOs	IF: Figure 4F	Figure 4F	2 CTL	4 NF1+, 2 NF1-	3	3	1-way ANOVA with Bonferroni correction	
Rac1-GTP	shCRLF3 hCOs	ELISA: Figure 4J	Figure 4F	4 shCTL	2 shCRLF3	3	5	unpaired, 2-tailed t-test	
RhoA-GTP	NSCs + CN03	ELISA: Figure 4K	Figure 4H	n/a	4 shCRLF3	3	3	unpaired, 2-tailed t-test	



**Table 3.5 | Key resources table.**

<b>REAGENT or RESOURCE</b>	<b>SOURCE</b>	<b>IDENTIFIER</b>
<b>Antibodies</b>		
Mouse monoclonal anti-SOX2	Cell Signaling Technology	Cat# 4900, RRID: AB_10560516
Rabbit monoclonal anti-SOX2	Abcam	Cat# ab92494, RRID: AB_10585428
Rabbit monoclonal anti-Oct-4A	Cell Signaling Technology	Cat# 2840, RRID: AB_2167691
Rabbit polyclonal anti-Nanog	Cell Signaling Technology	Cat# 3580, RRID: AB_2150399
Mouse monoclonal anti-SMI-32	Biolegend	Cat# 801701, RRID: AB_2564642
Mouse monoclonal anti-SMI-312	Biolegend	Cat# 837904, RRID: AB_2566782
Rabbit monoclonal anti-NeuroD1	Abcam	Cat# ab205300
Mouse monoclonal anti-NeuroD1	Abcam	Cat# ab60704, RRID: AB_943491
Mouse monoclonal anti-NeuN	Millipore	Cat# MAB377, RRID: AB_2298772
Mouse monoclonal anti-Ki-67	BD Biosciences	Cat# 556003, RRID: AB_396287
Mouse monoclonal anti-MAP2 [HM-2]	Abcam	Cat# ab11267, RRID: AB_297885
Rabbit monoclonal anti-Cleaved Caspase-3 (Asp175) (5A1E)	Cell Signaling Technology	Cat# 9664, RRID: AB_2070042
Rabbit polyclonal anti-active Caspase-3	R&D systems	Cat# AF835, RRID: AB_2243952
Goat anti-Rabbit IgG (H+L) Secondary Antibody, Alexa Fluor 488	Thermo Fisher Scientific	Cat# A-11034, RRID: AB_2576217
Goat Anti-Mouse IgG (H+L) Secondary Antibody, Alexa Fluor 488	Thermo Fisher Scientific	Cat# A-11029, RRID: AB_138404
Goat Anti-Rabbit IgG (H+L) Secondary Antibody, Alexa Fluor 568	Thermo Fisher Scientific	Cat# A-11011, RRID: AB_143157
Goat Anti-Mouse IgG (H+L) Secondary Antibody, Alexa Fluor 568	Thermo Fisher Scientific	Cat# A-11004, RRID: AB_2534072
Rabbit polyclonal anti-SUZ12	Abcam	Cat# ab12073, RRID: AB_442939
Rabbit polyclonal anti-COPRS	Novus Biologicals	Cat# NBP2-30884
Rabbit polyclonal anti-CRLF3	Sigma-Aldrich	Cat# HPA007596, RRID: AB_1847241
Rabbit polyclonal anti-ATAD5	Lifespan Biosciences	Cat# LS-C19118-100, RRID: AB_1569353
Rabbit polyclonal anti-UTP6	Proteintech	Cat# 17671-1-AP, RRID: AB_2214465
Mouse monoclonal anti-GAPDH [6C5]	Abcam	Cat# ab8245, RRID: AB_2107448

IRDye 680RD Goat anti-Rabbit IgG antibody	LI-COR Biosciences	Cat# 926-68071, RRID: AB_10956166
IRDye 800CW Goat anti-Mouse IgG antibody	LI-COR Biosciences	Cat# 925-32210, RRID: AB_2687825
Rabbit monoclonal anti-PAX6	Abcam	Cat# ab19504, RRID: RRID:AB_2750924
Mouse monoclonal anti-OTX2	Thermo Fisher Scientific	Cat# MA5-15854, RRID:AB_11155193
Rabbit polyclonal anti-EN1	Thermo Fisher Scientific	Cat# PA5-14149, RRID:AB_2231168
Mouse monoclonal anti-GBX2	Lifespan Biosciences	Cat# LS-C197281, NA
Rabbit monoclonal anti-TBR1	Abcam	Cat# ab31940, RRID:AB_2200219
Mouse monoclonal anti-SATB2	Abcam	Cat# ab51502, RRID:AB_882455
Rabbit polyclonal anti-N-cadherin	Abcam	Cat# ab18203, RRID:AB_444317
Mouse monoclonal anti-Neurofibromin	Manuscript in preparation	N/A
Rabbit polyclonal anti-Nestin	Abcam	Cat# ab92391, RRID:AB_10561437
Rabbit monoclonal anti-Vimentin	Cell Signaling Technology	Cat# 5741, RRID:AB_10695459
Rabbit monoclonal Anti-Vinculin	Abcam	Cat# ab129002, RRID:AB_11144129
Mouse monoclonal anti-neurofibromin	proprietary	n/a
<b>Bacterial and Virus Strains</b>		
<i>CRLF3</i> shRNA lentiviral particles	Santa Cruz Biotechnology	Cat# sc-94066-V
Control shRNA lentiviral particles	Santa Cruz Biotechnology	Cat# sc-108080
<i>CRLF3</i> -Human shRNA lentiviral particles (4 unique 29mer target-specific shRNA, 1 scramble control)	OriGene Technologies	Cat# TL305215V
Control Lenti particles, scrambled shRNA	OriGene Technologies	Cat# TR30021V
<b>Biological Samples</b>		
N/A		
<b>Chemicals, Peptides, and Recombinant Proteins</b>		
Matrigel® Basement Membrane Matrix	Corning	Cat# 354234
mTeSR™ Plus	STEMCELL Technologies	Cat# 05825
ReLeSR™	STEMCELL technologies	Cat# 05873
STEMdiff™ Neural Induction Medium	STEMCELL technologies	Cat# 05835
Recombinant Human FGF-basic (154 a.a.)	PeproTech	Cat# 100-18B
Y27632 RHO/ROCK pathway inhibitor	STEMCELL technologies	Cat# 72307
Gibco™ B-27 Plus Supplement (50X)	Thermo Fisher Scientific	Cat# A3582801
Gibco™ Neurobasal™ Medium	Thermo Fisher Scientific	Cat# 21-103-049
Gibco™ DMEM/F-12, HEPES	Thermo Fisher Scientific	Cat# 11330057
Gibco™ N-2 Supplement (100X)	Thermo Fisher Scientific	Cat# 17502001
Human recombinant insulin	Sigma-Aldrich	Cat# I2643-25MG
Gibco™ Penicillin-Streptomycin (5,000 U/mL)	Thermo Fisher Scientific	Cat# 15070063

RIPA Lysis and Extraction Buffer	Thermo Fisher Scientific	Cat# 89900
Gibco™ MEM Non-Essential Amino Acids Solution (100X)	Thermo Fisher Scientific	Cat# 11140050
Gibco™ GlutaMax™ Supplement	Thermo Fisher Scientific	Cat# 35050061
2-Mercaptoethanol	Sigma-Aldrich	Cat# M6250
Recombinant Human Erythropoietin/ EPO (Tissue Culture Grade)	R&D Systems	Cat# 287-TC-500
Triton™ X-100	Sigma-Aldrich	Cat# X100
Shandon™ Immu-Mount™	Thermo Fisher Scientific	Cat# 9990402
Tissue-Tek® O.C.T. Compound, Sakura® Finetek	Electron Microscopy Sciences	Cat# 4583
Hoechst 33258, Pentahydrate (bis-Benzimide)	Thermo Fisher Scientific	Cat# H3569
Pan-RAS-IN-1	MedChemExpress	Cat# HY-101295
4x Laemmli Sample Buffer	Bio-Rad	Cat# 1610747
Aprotinin, serine protease inhibitor	Abcam	Cat# ab146286
Leupeptin	Sigma-Aldrich	Cat# L2884
PMSF	Sigma-Aldrich	Cat# 10837091001
Puromycin	STEMCELL Technologies	Cat# 73342
Gibco™ Goat serum	Thermo Fisher Scientific	Cat# 16210064
Poly-L-Ornithine Solution (0.01%)	Sigma-Aldrich	Cat# A-004-C
CellAdhere™ Laminin-521	STEMCELL Technologies	Cat# 77003
SB 431542	Tocris	Cat# 1614
Compound E	STEMCELL Technologies	Cat# 73952
Dorsomorphin	Abcam	Cat# ab120843
Recombinant Human LIF	PeproTech	Cat# 300-05
Accutase® Cell Detachment Solution	Fisher Scientific	Cat# MT25058CI
RhoA activator CN03A	Cytoskeleton	Cat# NC0272107
Recombinant Human/Murine/Rat BDNF	PeproTech	Cat# 450-02
Recombinant Human IGF-I	PeproTech	Cat# 100-11
Human Recombinant GDNF	STEMCELL Technologies	Cat# 78058
Dibutyryl-cAMP, sodium salt 250mg	PeproTech	Cat# 1698950
<b>Critical Commercial Assays</b>		
Click-iT™ EdU Cell Proliferation Kit for Imaging, Alexa Fluor™ 488 dye	Thermo Fisher Scientific	Cat# C10337
<i>In Situ</i> Cell Death Detection Kit, Fluorescein	Sigma-Aldrich	Cat# 11684795910
Ras Activation ELISA, Colorimetric	Cell Biolabs	Cat# STA-440
RNeasy Mini Kit	Qiagen	Cat# 74104
Applied Biosystems™ High-Capacity cDNA Reverse Transcription Kit with RNase Inhibitor	Thermo Fisher Scientific	Cat# 4374966
Applied Biosystems™ TaqMan™ Fast Advanced Master Mix, no UNG	Thermo Fisher Scientific	Cat# A44359
Pierce™ BCA Protein Assay Kit	Thermo Fisher Scientific	Cat# 23225
RhoA G-LISA Activation Assay, colorimetric	Cytoskeleton	Cat# BK124

Rac1 G-LISA Activation Assay, colorimetric	Cytoskeleton	Cat# BK128
<b>Deposited Data</b>		
Whole exome sequencing data	This paper	GEO accession # pending
RNA sequencing data	This paper	GEO accession # pending
Human RNA-seq time-series of the development of seven major organs	Expression Atlas	<a href="https://www.ebi.ac.uk/gxa/experiments/E-MTAB-6814/Results">https://www.ebi.ac.uk/gxa/experiments/E-MTAB-6814/Results</a>
<b>Experimental Models: Cell Lines</b>		
BJFF.6 (CTL1) hiPSCs	GeiC – Washington University	RRID: CVCL_VU02
TGD1 hiPSCs	This paper	N/A
TGD2 hiPSCs	This paper	N/A
TGD3 hiPSCs	This paper	N/A
aTGD hiPSCs	This paper	N/A
shCTL1 hiPSCs	This paper	N/A
shCTL2 hiPSCs	This paper	N/A
shCTL3 hiPSCs	This paper	N/A
shCTL4 hiPSCs	This paper	N/A
shCRLF3-1 hiPSCs	This paper	N/A
shCRLF3-2 hiPSCs	This paper	N/A
shCRLF3-3 hiPSCs	This paper	N/A
shCRLF3-4 hiPSCs	This paper	N/A
c.1149C>A <i>NF1</i> -mutant hiPSCs	(Anastasaki et al., 2020)	N/A
c.1185+1G>A <i>NF1</i> -mutant hiPSCs	(Anastasaki et al., 2020)	N/A
c.3431-32_dupGT <i>NF1</i> -mutant hiPSCs	(Anastasaki et al., 2020)	N/A
c.5425C>T <i>NF1</i> -mutant hiPSCs	(Anastasaki et al., 2020)	N/A
c.6619C>T <i>NF1</i> -mutant hiPSCs	(Anastasaki et al., 2020)	N/A
CTL2 hiPSCs	GeiC – Washington University (Dr. Matthew B. Harms)	N/A
CTL3 hiPSCs	GeiC – Washington University (Dr. Fumihiko Urano)	N/A
<b>Experimental Models: Organisms/Strains</b>		
N/A	N/A	N/A
<b>Oligonucleotides</b>		
Human <i>CRLF3</i> - TaqMan® Gene Expression Assay FAM-MGB	Thermo Fisher Scientific	Hs00367579_m1
Human <i>ATAD5</i> TaqMan® Gene Expression Assay FAM-MGB	Thermo Fisher Scientific	Hs00227495_m1
Human <i>TEFM</i> TaqMan® Gene Expression Assay FAM-MGB	Thermo Fisher Scientific	Hs00895248_m1
Human <i>ADAP2</i> TaqMan® Gene Expression Assay FAM-MGB	Thermo Fisher Scientific	Hs01106939_m1
Human <i>COPRS</i> TaqMan® Gene Expression Assay FAM-MGB	Thermo Fisher Scientific	Hs01047650_m1

Human <i>UTP6</i> TaqMan® Gene Expression Assay FAM-MGB	Thermo Fisher Scientific	Hs00251161_m1
Human <i>SUZ12</i> TaqMan® Gene Expression Assay FAM-MGB	Thermo Fisher Scientific	Hs00248742_m1
Human <i>LRRC37B</i> TaqMan® Gene Expression Assay FAM-MGB	Thermo Fisher Scientific	Hs03045845_m1
Human <i>MIR193A</i> TaqMan® Gene Expression Assay FAM-MGB	Thermo Fisher Scientific	Hs04273253_s1
Human <i>MIR365B</i> TaqMan® Gene Expression Assay FAM-MGB	Thermo Fisher Scientific	Hs04231549_s1
Human <i>MIR4725</i> TaqMan® Gene Expression Assay FAM-MGB	Thermo Fisher Scientific	Hs06637953_s1
Human <i>MIR4733</i> TaqMan® Gene Expression Assay FAM-MGB	Thermo Fisher Scientific	Hs04274676_s1
Human <i>GAPDH</i> TaqMan® Gene Expression Assay FAM-MGB	Thermo Fisher Scientific	Hs02786624_g1
<b>Recombinant DNA</b>		
N/A	N/A	N/A
<b>Software and Algorithms</b>		
Samtools 1.4.1	<a href="http://samtools.sourceforge.net/">http://samtools.sourceforge.net/</a>	RRID: SCR_002105
SnEff	<a href="http://snpeff.sourceforge.net/">http://snpeff.sourceforge.net/</a>	RRID: SCR_005191
Combined Annotation Dependent Depletion (CADD)	<a href="https://cadd.gs.washington.edu/">https://cadd.gs.washington.edu/</a>	RRID: SCR_018393
SIFT	<a href="http://sift.bii.a-star.edu.sg/">http://sift.bii.a-star.edu.sg/</a>	RRID: SCR_012813
PolyPhen: Polymorphism Phenotyping	<a href="http://genetics.bwh.harvard.edu/pph2/">http://genetics.bwh.harvard.edu/pph2/</a>	RRID: SCR_013189
Likelihood ratio test (LRT)	<a href="http://www.genetics.wustl.edu/jflab/lrt_query.html">http://www.genetics.wustl.edu/jflab/lrt_query.html</a>	N/A
GERP++	<a href="http://mendel.stanford.edu/SidowLab/downloads/gerp/">http://mendel.stanford.edu/SidowLab/downloads/gerp/</a>	RRID: SCR_000563
Fathmm	<a href="http://fathmm.biocompute.org.uk/fathmm-xf/about.html">http://fathmm.biocompute.org.uk/fathmm-xf/about.html</a>	N/A
Leica Application Suite X software	<a href="https://www.bio-rad.com/en-us/sku/1845000-cfx-manager-software?ID=1845000">https://www.bio-rad.com/en-us/sku/1845000-cfx-manager-software?ID=1845000</a>	RRID: SCR_013673
ImageJ/ Fiji v1.8	<a href="http://fiji.sc">http://fiji.sc</a>	RRID: SCR_002285
Bio-Rad CFX Manager 3.1	<a href="https://www.bio-rad.com/en-us/sku/1845000-cfx-manager-software?ID=1845000">https://www.bio-rad.com/en-us/sku/1845000-cfx-manager-software?ID=1845000</a>	N/A
LI-COR Image Studio Software v5.2	<a href="https://www.licor.com/bio/products/software/image_studio/?gclid=EAIaIQobChMIrv7s26ug1wIVQUCGCh1kvQgLEAAYASAAEgLcYPD_BwE">https://www.licor.com/bio/products/software/image_studio/?gclid=EAIaIQobChMIrv7s26ug1wIVQUCGCh1kvQgLEAAYASAAEgLcYPD_BwE</a>	RRID: SCR_015795
COBALT: Constraint-based Multiple Alignment Tool	<a href="http://www.ncbi.nlm.nih.gov/tools/cobalt/cobalt.cgi?link_1oc=BlastHomeAd">http://www.ncbi.nlm.nih.gov/tools/cobalt/cobalt.cgi?link_1oc=BlastHomeAd</a>	RRID: SCR_004152

GraphPad Prism 8	<a href="http://www.graphpad.com/">http://www.graphpad.com/</a>	RRID: SCR_002798
Adobe Illustrator 2020	<a href="http://www.adobe.com/products/illustrator.html">http://www.adobe.com/products/illustrator.html</a>	RRID: SCR_010279
Adobe Photoshop 2020	<a href="https://www.adobe.com/products/photoshop.html">https://www.adobe.com/products/photoshop.html</a>	RRID: SCR_014199
Jalview	<a href="http://www.jalview.org/">http://www.jalview.org/</a>	RRID: SCR_006459
Samtools	<a href="http://samtools.sourceforge.net/">http://samtools.sourceforge.net/</a>	RRID:SCR_002105
bcl2fastq	<a href="https://support.illumina.com/sequencing/sequencing_software/bcl2fastq-conversion-software.html">https://support.illumina.com/sequencing/sequencing_software/bcl2fastq-conversion-software.html</a>	RRID:SCR_015058
STAR version 2.7.3a	<a href="https://github.com/alexdobin/STAR">https://github.com/alexdobin/STAR</a>	RRID:SCR_015899
Ensembl	<a href="http://www.ensembl.org/">http://www.ensembl.org/</a>	RRID:SCR_002344
DESeq2	<a href="https://bioconductor.org/packages/release/bioc/html/DESeq2.html">https://bioconductor.org/packages/release/bioc/html/DESeq2.html</a>	RRID:SCR_015687
Partek Flow software, version 9.0.20	<a href="https://www.partek.com/?q=partekgs">https://www.partek.com/?q=partekgs</a>	RRID:SCR_011860
Gene Ontology enrichment	<a href="http://geneontology.org/">http://geneontology.org/</a>	RRID:SCR_002811
<b>Other</b>		
Corning® Costar® Ultra-Low Attachment 96 well round bottom plate	Sigma-Aldrich	Cat# CLS7007
Corning® Costar® Ultra-Low Attachment 24 well plate	Sigma-Aldrich	Cat# CLS3473
25cm <sup>2</sup> Tissue Culture Flask - Vent Cap, Sterile	CELLTREAT	Cat# 229331
6 Well Tissue Culture Plate, Sterile	Celltreat	Cat# 229106

### 3.7 Discussion

The successful deployment of the hCO platform to identify the cellular and molecular etiologies for human 17q11.2 microdeletion-related neurodevelopmental abnormalities raises several important points. First, it adds *CRLF3* to the growing list of genes contained within the *NF1*-TGD locus that could contribute to specific clinical phenotypes observed not only in patients with NF1, but also in the general population. For example, mutations in *RNF135* have been reported in patients with autism (Tastet et al., 2015) and in families with dysmorphic facial features and learning disabilities (Douglas et al., 2007). Biallelic loss of *SUZ12* is frequently observed in malignant peripheral nerve sheath tumors (MPNSTs) (Lee et al., 2014; Zhang et al., 2014), while *ADAP2* is required for normal cardiac morphogenesis (Venturin et al., 2014) relevant to cardiovascular malformations observed in 17q11.2 microdeletion patients (Venturin et al., 2004). Further investigation into the roles of other deleted genes within this interval may provide new insights relevant to the diagnosis and treatment of human disease. Second, using a combination of lentiviral *CRLF3* genetic silencing and pharmacologic rescue of RhoA activity experiments (CN03 treatments), we establish that *CRLF3* regulates human neurogenesis, neuron survival, and dendritic development through RhoA activation, extending prior studies on the role of RhoA signaling in murine neuron maturation relevant to neurodevelopment and cognition (Richter et al., 2019). Third, the provocative early-phase clinical analyses suggest that *CRLF3* mutation might identify a high-risk group of NF1 patients more likely to harbor an increased autism trait burden. While *CRLF3* has not been previously implicated as an autism risk gene (Abrahams et al., 2013; Banerjee-Basu and Packer, 2010), it constitutes a potential therapeutic

target and a risk assessment tool in future studies involving larger numbers of individuals, with a focus on its sensitivity and specificity for predicting ASD symptomatology in children with NF1.

### **Limitations of the Study**

While we show that CRLF3 reduction accounts for the impaired neuronal maturation and dendritic outgrowth in *NF1*-TGD hCOs, further work will be required to establish a link between *NF1*-TGD dendritic dysfunction and autism. Additionally, analysis of an *in vivo* model would be required to validate the translatability of these results. Similarly, as aTGD mutations are quite rare, additional studies should focus on the neuronal function in this subset of TGD patients. Lastly, with the availability of reliable antibodies that recognize the proteins encoded by other genes in the microdeletion locus and *CRLF3* expression constructs, future studies could explore the relationship between these deleted genes and brain development.



# **Chapter 4: Conclusions and Future Directions**

## 4.1 Preface

**Parts of this chapter are adapted from the following manuscript:**

**Wegscheid, M.L., Anastasaki, C. & Gutmann, D.H.** Human stem cell modeling in neurofibromatosis type 1 (NF1). *Experimental Neurology* **299**, 270-280 (2018).

**Author contributions for the citation above:**

M.L.W. and D.H.G. wrote the paper. M.L.W. and C.A. made the figures.

## 4.2 Summary of findings

The implementation of precision medicine strategies requires the identification of the factors that underlie individual disease risk and predict clinical outcome, as well as the development of human cellular platforms for therapeutic evaluation. This challenge is exemplified by NF1, a common neurogenetic single-gene disorder in which affected individuals exhibit a wide range of medical problems (Jett and Friedman, 2010). Based on emerging population-based genotype-phenotype association studies in NF1 (Anastasaki et al., 2017; Koczkowska et al., 2018b; Mautner et al., 2010; Morris et al., 2016a; Morris and Gutmann, 2018; Pinna et al., 2015; Sharif et al., 2011; Trevisson et al., 2019; Upadhyaya et al., 2007), **we hypothesized that the germline *NF1* gene mutation represents one clinically actionable risk factor for NF1-associated symptomatology.** The experiments described in this dissertation critically evaluated this hypothesis by investigating the effects of different *NF1* mutations on human neurodevelopment using a collection of isogenic and non-isogenic hiPSC-derived CNS cells and human cerebral organoids (hCOs) harboring patient-derived *NF1* germline gene mutations.

The hypothesis that was raised in Chapter 1 was addressed in Chapter 2 of this dissertation and is summarized in **Figure 4.1**. In Chapter 2, we analyzed an isogenic series of CRISPR/Cas9-engineered hiPSCs harboring seven different intragenic NF1 patient germline *NF1* gene mutations, as well as patient-derived hiPSCs and *Nf1*-mutant mice bearing the same mutations. Importantly, unlike previous studies, the use of an isogenic series of hiPSCs eliminated other contributing factors, such as sex and background genomic variation, and permitted a direct examination of the effects of different *NF1* gene mutations. These experiments revealed both

common and differential effects of distinct *NF1* germline gene mutations on CNS cells and tissues.

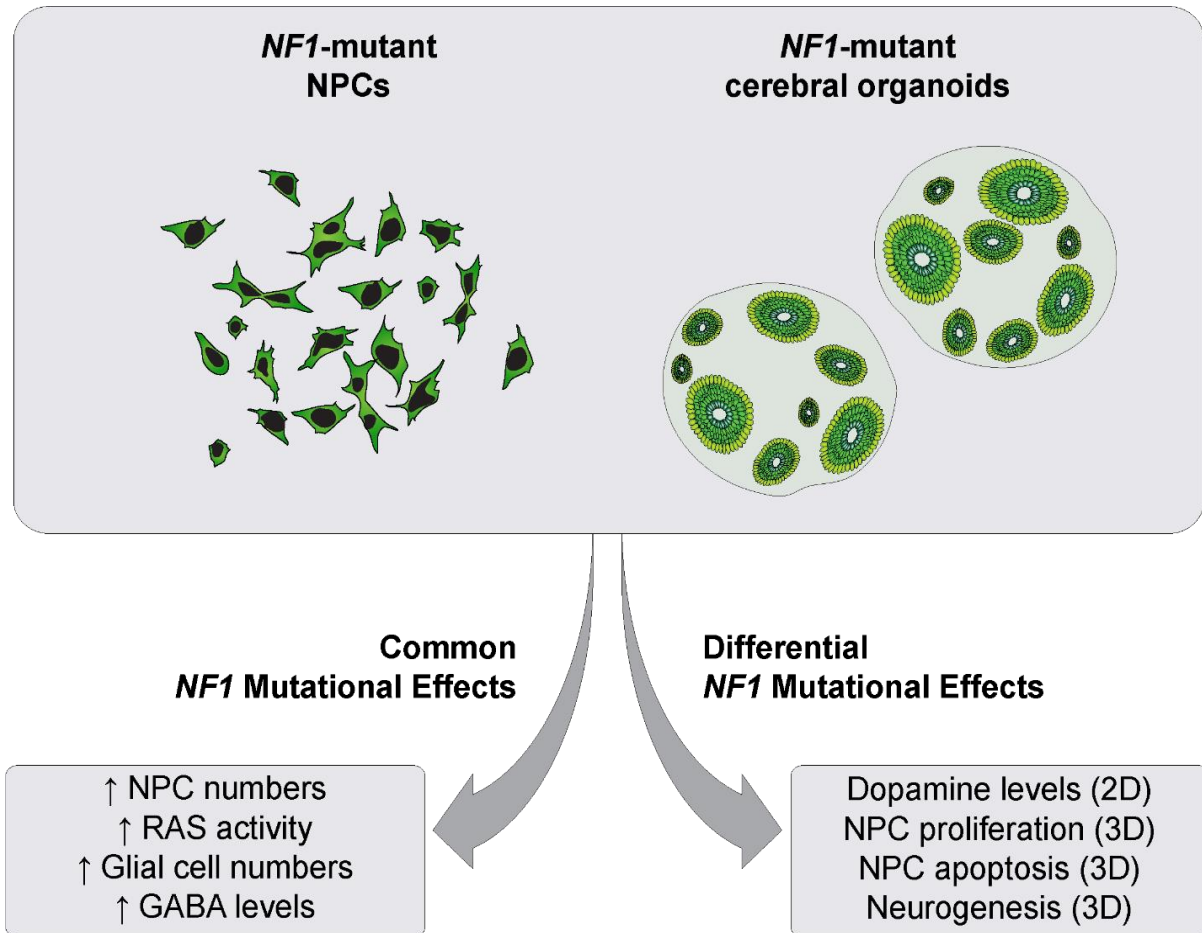


**Figure 4.1 | Experimental conclusions from Chapter 2.** hiPSC-derived *NF1*-mutant NPCs and hCOs revealed both common and differential effects of distinct *NF1* gene mutations on human CNS cells and tissues.

Consistent with numerous reports in *Nf1*-mutant mouse models describing *NF1*/RAS-mediated control of cell proliferation (Hegedus et al., 2007; Kaul et al., 2015; Lee et al., 2010; Wang et al., 2012), all isogenic *NF1*-mutant 2D NPCs and astrocytes exhibited an increase in RAS activity, as well as increased cell proliferation. Patient-derived NPCs, as well as to whole-brain lysates

from genetically engineered mice harboring analogous germline *Nf1* gene mutations, were also confirmed to have increased RAS activity. Similarly, isogenic and patient-derived *NF1*-mutant hCOs exhibited increased whole-organoid RAS activity and production of astrocytes, illustrating that all heterozygous *NF1* mutations increase RAS activity and RAS-regulated cell proliferation in human and murine CNS cells. Experiments leveraging 2D hiPSC-derived GABAergic neurons also revealed a shared abnormality of increased GABA levels, consistent with previous studies describing increased GABAergic tone in *Nf1*-mutant (*Nf1*<sup>+/-</sup>) mice (Costa et al., 2002; Cui et al., 2008).

In contrast, we observed differential effects of *NF1* germline gene mutations on 2D NPC dopamine (DA) levels, as well as NPC proliferation, apoptosis and neuronal differentiation in 3D hCOs. In contrast to *Nf1*<sup>+/-</sup> mice exhibiting 50% reductions in hippocampal DA levels (Anastasaki et al., 2015), one group of *NF1*-mutant NPCs (c.1149C>A; c.2041C>T; c.6619C>T), had >70% reduction in dopamine levels compared to controls, whereas another group of *NF1*-mutant NPCs (c.1185+1G>A; c.3431-32\_dupGT, c.5425C>T, and c.6513T>A) had <40% reduction in DA levels. This finding was recapitulated in patient-derived 2D NPCs, as well as *Nf1*-mutant genetically engineered mouse brain lysates harboring analogous mutations. In isogenic and patient-derived hiPSC-hCOs, one group of *NF1* mutants (c.1185+1G>A; c.5425C>T; c.6619C>T) exhibited increased NPC proliferation and apoptosis, while the other group of *NF1* mutants (c.1149C>A; c.3431-32\_dupGT) had normal NPC proliferation, but reduced NPC apoptosis. In addition, this latter group of *NF1* mutants had delayed production of immature neurons. The proof-of-concept experiments described in Chapter 2 clearly demonstrate that distinct *NF1* mutations have differential effects on human CNS cells and tissues. In

combination with compelling population-based genotype-phenotype associations, these experiments (1) suggest that the germline *NF1* gene mutation is one of the factors that underlies clinical heterogeneity in patients with NF1 and (2) highlight the significance of employing preclinical models with different patient germline mutations to better represent the unique pathologies in patients. In addition, these findings support the existence of RAS-independent neurofibromin functions, as the observed differences in neuronal differentiation in cerebral organoids and NPC DA levels do not correlate with RAS activity levels. Lastly, the observation that all *NF1*-mutant 2D NPCs exhibited increased proliferation, but only a subset of *NF1*-mutant hCOs exhibited increased NPC proliferation, attests to the critical role of heterogeneous cell-cell interactions (*e.g.*, differentiating neurons, astrocytes and NPCs) in dictating phenotypic outcomes. This notion is further supported by previously reported cell-autonomous and non-cell-autonomous (stromal) effects of distinct *Nf1* gene mutations on astrocyte proliferation in genetically engineered murine models of optic pathway glioma (Kaul et al., 2015). Future studies aimed at dissecting the complex interplay between different cell types relevant to brain developmental abnormalities and tumorigenesis in personalized NF1 preclinical models will be instrumental in defining molecular and cellular mechanisms underlying disease heterogeneity.

In Chapter 3, we sought to understand the molecular and cellular etiologies underlying the severe developmental delays and intellectual disability seen in children with a specific type of *NF1* mutation involving a heterozygous microdeletion of the *NF1* gene and several contiguous genes (1.4 Mb *NF1*-total gene deletion [*NF1*-TGD]). For these studies, we analyzed hCOs derived from three neurologically normal control individuals and three individuals harboring a 1.4 Mb *NF1*-TGD. The experimental conclusions from Chapter 3 are summarized in **Figure 4.2**.

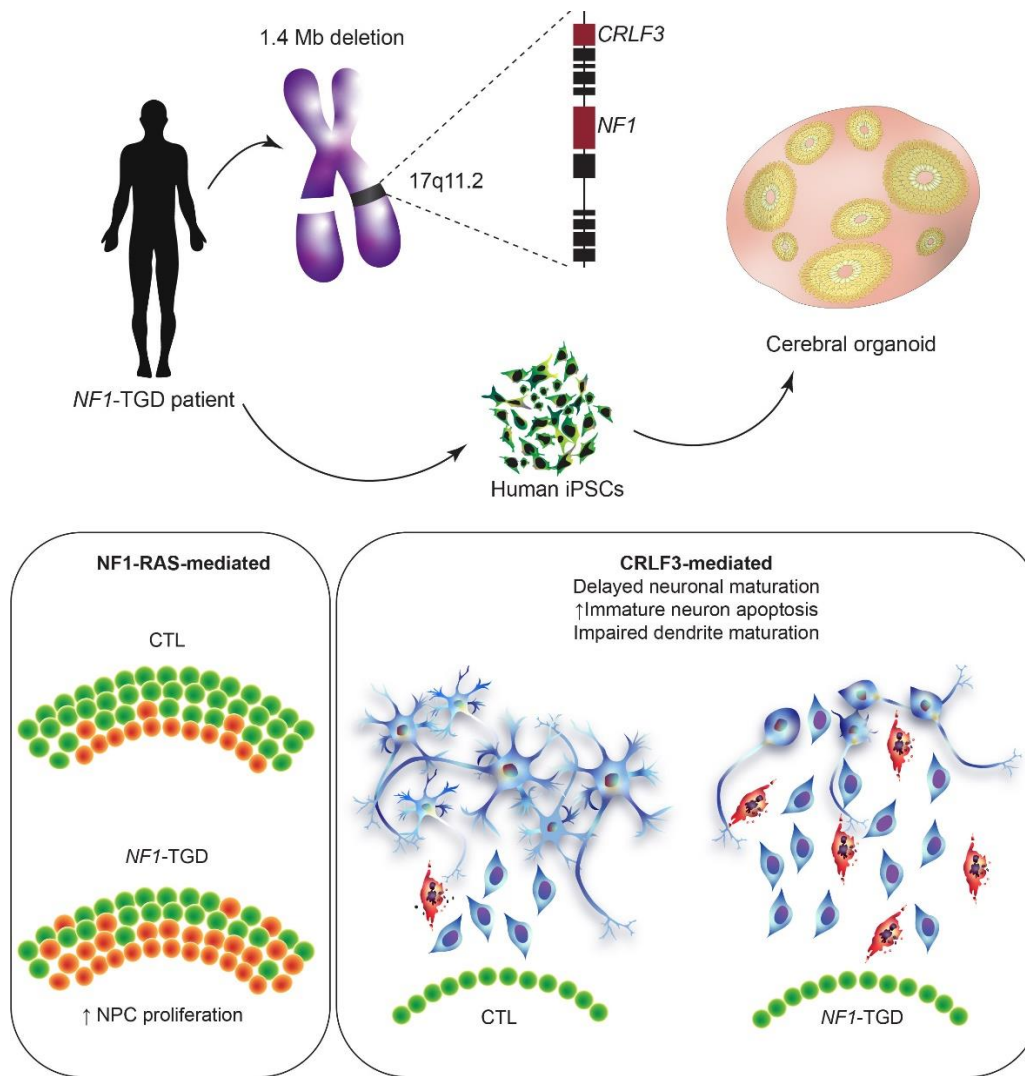


**Figure 4.2 | Experimental conclusions from Chapter 3.** Patient-derived hiPSC-hCOs harboring a 1.4 Mb *NF1*-TGD revealed RAS-dependent roles for the *NF1* gene in human NPC proliferation, as well as critical roles for *CRLF3*-dependent RhoA activation in neuronal survival, differentiation, and maturation.

First, our experiments revealed that total deletion of one copy of the *NF1* gene increases NPC proliferation through RAS inactivation in hCOs. This finding is consistent with results from one

group of *NF1*-mutant hCOs harboring c.1185+1G>A, c.5425C>T, and c.6619C>T intragenic *NF1* mutations. Second, we identified neuronal defects (delayed neuronal differentiation, reduced immature neuron survival and markedly impaired dendrite maturation) in the 1.4 Mb *NF1*-TGD hCOs that were not found in hCOs harboring *NF1* intragenic mutations or a 0.6-0.9 Mb atypical deletion. Third, we discovered impaired cytokine receptor-like factor 3 (*CRLF3*)-mediated RhoA signaling as the etiologic mechanism underlying the 1.4 Mb *NF1*-TGD defects in neuronal differentiation, survival and dendrite maturation. Lastly, we demonstrated a higher autistic trait burden in NF1 patients harboring a deleterious germline mutation in the *CRLF3* gene (c.1166T>C, p.Leu389Pro). Collectively, these experiments revealed a causative gene within the *NF1*-TGD locus responsible for the profound neurodevelopmental defects in *NF1*-TGD hCOs and autistic trait burden in children with NF1.

### 4.3 Future directions

The experiments herein have demonstrated that distinct *NF1* gene mutations exert differential effects on human CNS cells and tissues. These proof-of-concept studies serve as a foundation for future studies aimed at (1) investigating the cellular and physiological consequences of specific germline patient mutations relevant to NF1 disease pathogenesis and (2) dissecting the molecular mechanisms underlying *NF1*-associated phenotypes. Mechanistic etiologies underlying the observed neurogenic abnormalities in intragenic and *NF1*-TGD *NF1*-mutant hCOs from Chapter 2 and 3 are discussed in section 4.3.1. The potential applications of this *NF1*-mutant iPSC-hCO platform to model additional NF1-associated pathologies is discussed in section 4.3.2.



### 4.3.1 Mechanistic etiologies

#### *RAS signaling pathway responsible for NPC hyperproliferation*

To define the RAS downstream signaling pathway responsible for driving increased NPC proliferation in *NF1*-TGD and several intragenic *NF1*-mutant hCOs, we surveyed RAS effectors that have been previously implicated in the regulation of CNS cell proliferation and differentiation in murine models of NF1 (ERK, AKT, S6, cyclic AMP) (Chen et al., 2015; Hegedus et al., 2007; Kaul et al., 2015; Lee et al., 2010; Sanchez-Ortiz et al., 2014; Wang et al., 2012). There was no difference in intracellular levels of cAMP between *NF1*-TGD and control (CTL) hCOs at 16DIV (**Figure 4.3A**). Furthermore, preliminary western blotting results revealed inconsistent changes in ERK, AKT or S6 phosphorylation between genotypes (**Figure 4.3B-E**).

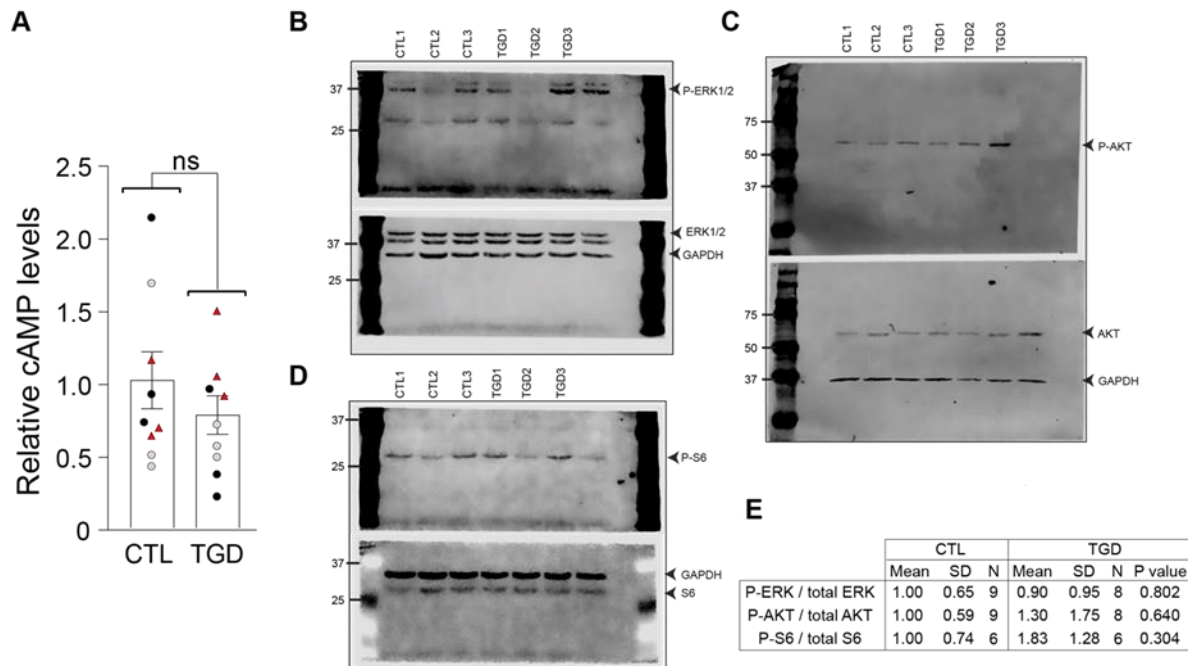


**Figure 4.3 | Analysis of RAS downstream effectors in TGD hiPSC-hCOs.**

(A) cAMP levels in TGD compared to CTL 16DIV hCOs. Independent hiPSC lines representing three different CTL lines (black, CTL1; white, CTL2; red, CTL3) and three different TGD lines (black, TGD1; white, TGD2; red, TGD3) are shown. Each data point represents 3 pooled organoids. (B-D) Representative Western blots and (E) quantification of  $pAKT^{S473}$ ,  $pERK1/2^{T202/T204}$  and  $pS6^{S240/244}$  levels in CTL and 1.4 Mb *NFI*-TGD 16DIV hCOs. GAPDH was used as a total protein loading control. N represents the number of independent organoid lysates analyzed. Statistical analysis by unpaired, two-tailed *t*-test.

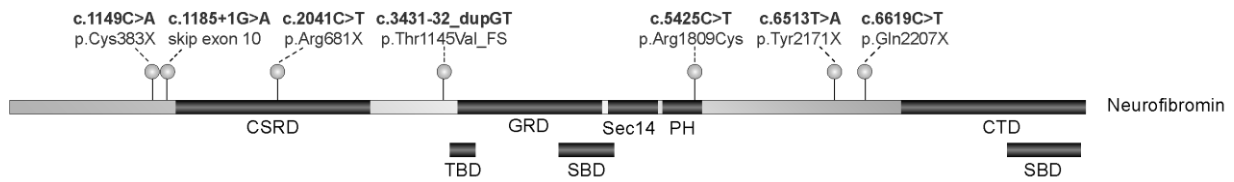
One possible explanation for the highly variable results in phospho-protein activation in iPSC-hCOs could be the heterogenous composition of the organoid cultures. While spontaneous unguided hCO differentiation offers the unique opportunity to model the evolution of self-organizing cerebral tissues, each organoid generated by this protocol contains variable numbers

of NPC-containing zones. It is possible that the variability in hCO NPC zone numbers per tissue could affect the measured whole organoid effector activation. One strategy to overcome this would be to generate hCOs containing a single ventricle-like zone using defining patterning molecules to improve reproducibility (Lee et al., 2016). Alternatively, hCO-NPCs could be isolated using fluorescent activated cell sorting (FACS) (Janssens et al., 2019), and downstream effector engagement assayed on a pure population of hCO-derived NPCs. We have previously attempted to measure effector activation in 2D hiPSC-NPCs, but had similarly variable results in ERK, AKT and S6 phosphorylation across replicates. Further optimization will be required to assess RAS downstream effector activation in 2D NPCs and 3D hCOs. Ultimately, future experiments aimed at understanding (1) how *NF1*/RAS downstream signaling pathway engagement dictates cellular responses and (2) how those outputs can be contextually modified (genetic, cellular and tissue levels) (Smithson et al., 2016), will lead to the design of more effective, individualized therapies for NF1-associated pathologies.

#### ***Alternative neurofibromin-binding partners***

The fact that the observed differences in neuronal differentiation in intragenic *NF1*-mutant hCOs and 2D NPC DA levels do not correlate with RAS activation supports the existence of non-RAS-mediated neurofibromin functions. Putative neurofibromin binding partners include proteins important for neuronal differentiation, such as syndecans (Hsueh et al., 2001), vasolin-containing protein (Wang et al., 2011), tubulin (Bollag et al., 1993), and serotonin 5-HT<sub>6</sub> receptors (Deraredj Nadim et al., 2016) (**Figure 4.4**). However, the validation of neurofibromin binding partners has largely been hindered by a lack of high affinity anti-neurofibromin antibodies. To overcome this obstacle, the Gutmann Laboratory has generated an endogenous FLAG-tagged

*NF1* allele in both hiPSCs and genetically engineered mice to effectively immunoprecipitate neuron-specific neurofibromin binding complexes and investigate these protein-protein interactions using mass spectrometry. These investigations will be critical to advance our understanding of how *NF1* mutations differentially affect cognition and behavior in children with NF1.



	Domain	Interacting proteins	References
<b>CSRD</b>	Cysteine–serine-rich domain	DDAH1	(Tokuo et al., 2001)
<b>TBD</b>	Tubulin-binding domain	Tubulin LRPPRC	(Bollag et al., 1993) (Arun et al., 2013)
<b>GRD</b>	GTPase-activating protein-related domain	RAS APP ETEA SPRED1	(Martin et al., 1990) (De Schepper et al., 2006) (Phan et al., 2010) (Stowe et al., 2012)
<b>SBD</b>	Syndecan-binding domain	Syndecans	(Hsueh et al., 2001)
<b>Sec14/PH</b>	Sec14 domain and pleckstrin homology domain	Phospholipids VCP LIMK2 Calveolin 5-HT <sub>6</sub>	(Welti et al., 2007) (Wang et al., 2011) (Vallee et al., 2012) (Boyanapalli et al., 2006) (Deraredj Nadim et al., 2016)
<b>CTD</b>	Carboxy-terminal domain	5-HT <sub>6</sub> CRMP2 14-3-3 FAK DDAH1 CRMP2/4	(Deraredj Nadim et al., 2016) (Hensley et al., 2010) (Feng et al., 2004) (Kweh et al., 2009) (Tokuo et al., 2001) (Patrakitkomjorn et al., 2008)

**Figure 4.4 | Neurofibromin domains and putative binding partners.**

Schematic diagram illustrating neurofibromin domains, including a cysteine–serine-rich domain (CSRD), a tubulin-binding domain (TBD), a GTPase-activating protein-related domain (GRD), a Sec14 domain, a pleckstrin homology (PH) domain, a carboxy-terminal domain (CTD), and a syndecan-binding domain (SBD). Positions of the intragenic patient-derived *NF1* mutations discussed in this dissertation are indicated. Proteins that are believed to interact with each domain are indicated in the accompanying table. Adapted from (Ratner and Miller, 2015).

### 4.3.2 Prospective directions for hCO modeling of NF1-associated brain pathologies

#### *Neuronal subtype specification and functional maturation*

In this dissertation, we leveraged an iPSC-hCO experimental platform to investigate the effects of different *NF1* mutations on early human brain development, as transcriptome and epigenome studies have demonstrated that hCOs most closely resemble fetal brain expression signatures during the first and early second trimester (Camp et al., 2015; Luo et al., 2016; Qian et al., 2016a; Velasco et al., 2019). However, hiPSC-hCOs can also be leveraged to investigate *NF1* mutational effects on mid-gestational neuronal subtype specification and functional maturation. Preliminary results and alternative approaches to investigating these parameters are discussed below.

Neurodevelopmental disorders frequently involve neuronal subtype (*e.g.*, excitatory and inhibitory) imbalances that arise during brain development (Gao and Penzes, 2015). Based on this observation, we hypothesized that *NF1* gene mutations may differentially impair the specification and functional maturation of excitatory and inhibitory neurons during brain development. To evaluate the effects of *NF1* gene mutations on neuronal subtype specification, we evaluated the production of glutamatergic (glutaminase<sup>+</sup>) and GABAergic (GAD67<sup>+</sup>) neurons in hCOs using immunohistochemistry at 105 days *in vitro* (DIV). In contrast to previous reports describing mature neuronal subtypes and spontaneous synaptic activity in hCOs between 3-6 months in culture (Monzel et al., 2017; Pasca et al., 2015; Qian et al., 2016b; Quadrato et al., 2017; Trujillo et al., 2019), our preliminary experiments revealed that distinct populations of glutamatergic and GABAergic neurons did not form 105DIV in *NF1*-mutant or control cerebral

organoids. Furthermore, using a Maestro multi-electrode array (MEA) system, we confirmed that 105DIV hCOs did not spontaneously fire action potentials.

Notably, hCO differentiation protocols used in studies describing subtype specification and functional maturation supplemented cerebral organoid differentiation media with BDNF, GDNF, L-ascorbic acid, cAMP and TGF $\beta$ 3 to promote maturation. Based on this observation, we generated cerebral organoids using a modified protocol to promote neuronal maturation, in which standard hCO media was supplemented with 200  $\mu$ M L-ascorbic acid, 500  $\mu$ M dibutyryl cAMP, 1 ng/mL TGF $\beta$ 3, 10 ng/mL BDNF and 10 ng/mL GDNF. Using immunohistochemistry, we confirmed that distinct neuronal subtypes were produced in cerebral organoids by 105DIV using this modified protocol (**Figure 4.5A**). However, >70% of the neurons were still double positive for GAD67 and glutaminase in controls and *NFI*-mutants after 105DIV using the modified protocol, suggesting that subtype specification was incomplete.

In addition, synaptic activity was detected in cerebral organoids after 105DIV in hCOs generated using the modified maturation protocol (**Figure 4.5B**). Action potentials and burst activity were detected in CTL and *NFI*-mutant hCOs. Network bursting activity, which measures the presence and functionality of mature neuronal networks, was not detected. Maximum mean firing rates in CTL and *NFI*-mutant hCOs were lower than reported averages in the literature for 105DIV hCOs, (~0.6 Hz compared to reported 2.5 Hz) (Trujillo et al., 2019), and largely derived from only a handful of active electrodes. In addition, different tissues from the same experimental replicate frequently exhibited variable activity, with some tissues still having no spontaneous activity.

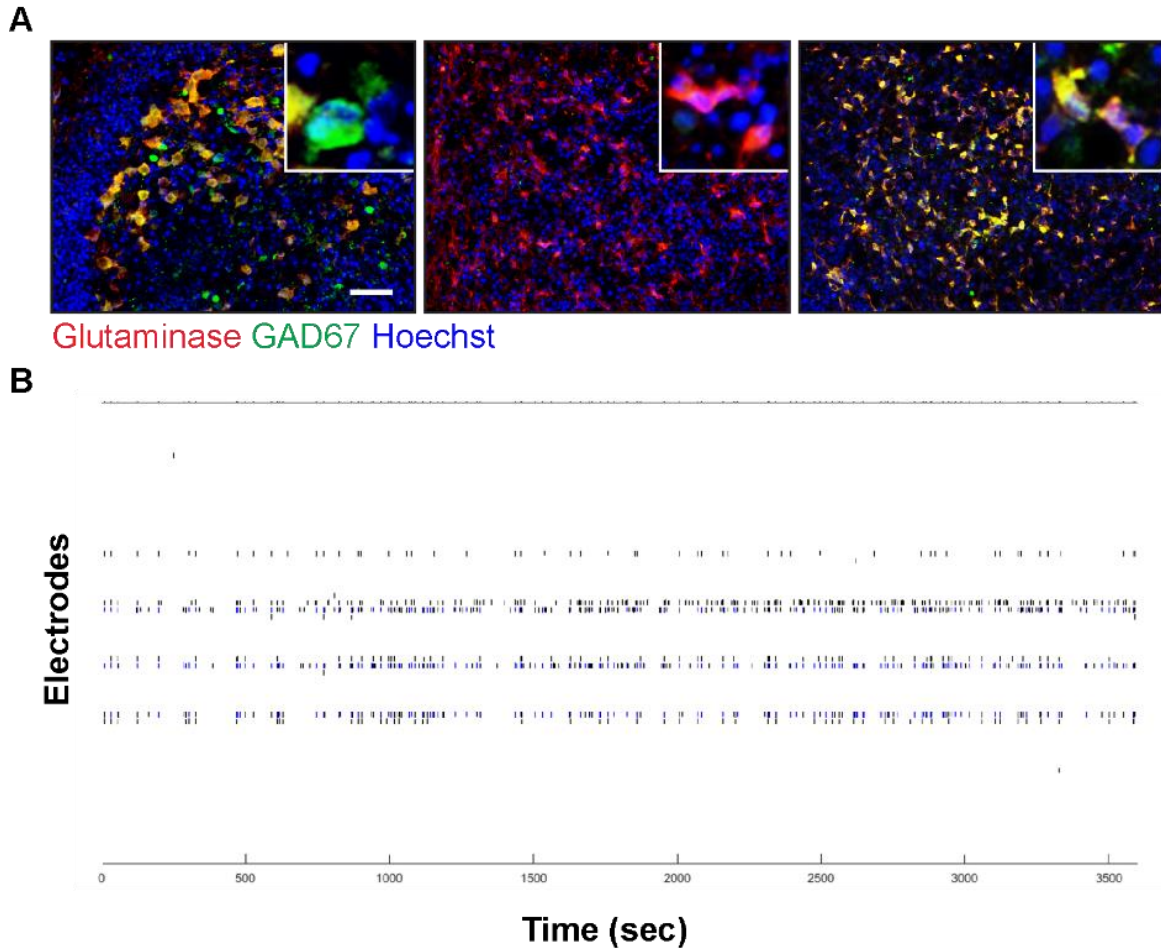


**Figure 4.5 | hCO neuronal subtype specification and functional maturation.**

(A) Representative images of 105DIV cerebral organoids immunolabeled for glutamatergic neurons (glutaminase, red) and GABAergic neurons (GAD67, green). The insets illustrate mature GABAergic neurons (GAD67<sup>+</sup>, glutaminase<sup>-</sup>), mature glutamatergic neurons (glutaminase<sup>+</sup>, GAD67<sup>-</sup>) and neurons of unspecified subtype (glutaminase<sup>+</sup>, GAD67<sup>+</sup>). Scale bar: 50  $\mu$ m. (B) A representative image of a spike raster plot illustrating neuronal network activity over 64 electrodes during a 60-minute recording session in a 105DIV cerebral organoid. Each individual spike represents an action potential from a neuron. Neuronal bursting activity is indicated by blue spikes.



Taken together, these results demonstrate the need to maintain CTL and *NFI*-mutant hCOs for longer than 105DIV to achieve neuronal subtype specification and functional maturation, and to assess for differences in those parameters. Another potentially important difference between our hCO protocol and many described in the literature involves embedding of 3D tissues in gelatinous protein matrices (Matrigel). While several hCO protocols do not employ Matrigel embedding (Anastasaki et al., 2020; Pasca et al., 2015; Trujillo et al., 2019), many protocols do incorporate extracellular matrices to support the outgrowth of neuroepithelial buds. We spent several months optimizing cerebral organoid cultures with this Matrigel embedding step. However, ~40% of hCOs did not survive Matrigel embedding, and the remaining hCOs embedded in Matrigel had highly heterogeneous shapes and sizes across experimental replicates. Further optimization of this protocol, either by incorporating micro-scaffolds or solubilized Matrigel (Lancaster et al., 2017), may improve reproducibility of long-term cultures and derivation of cortical tissues with mature neuronal subtypes.

### ***Methods for MEA***

MEA recording was conducted using the Maestro MEA system from Axion BioSystems. A 6-well MEA plate (catalog no. M384-TMEA-6W) plate containing 64 platinum microelectrodes per well, was precoated with polyethyleneimine and 10 $\mu$ g/mL laminin. Cerebral organoids were placed onto the array at 84DIV and were cultured on the plates for an additional 3 weeks prior to recording. Measurements were collected 3 hours after medium was changed at 105DIV of differentiation. The plate was first allowed to rest in the Maestro device for 10 minutes prior to data collection. Spontaneous activity was recorded using AxIS Software v2.5.2.1, Spontaneous Neural Configuration (Axion Biosystems) at a sampling rate of 12.5 kHz for 15 minutes at 37°C

in neuronal maturation media. A Butterworth band pass filter with 200-3000 Hz cutoff frequency and a threshold of 6 x SD were set to minimize false-positives and missed detections. The Neural Metric Tool v2.6 (Axion BioSystems) was used to analyze the spike raster plots. Electrodes with an average of  $\geq 5$  spikes/min were defined as active. Bursts were identified in the data recorded from each individual electrode using an inter-spike interval (ISI) threshold requiring a minimum number of 5 spikes with a maximum ISI of 100 ms. A minimum of 10 spikes under the same ISI with a minimum of 25% active electrodes were required for network bursts in the well.

### ***Myelination/ Oligodendrocytes***

Another critically important cell type in the developing human brain, amenable to hCO modeling, is oligodendrocytes. Oligodendrocyte ensheathment of neuronal axons is a prerequisite for saltatory nerve conduction (Kaplan et al., 1997). Furthermore, oligodendrocytes play a critical role in providing neurotrophic and metabolic support to neurons (Dougherty et al., 2000; Wilkins et al., 2003). 60-70% of children with NF1 exhibit white matter abnormalities (enlarged brain white matter tracts, T2 hyperintensities and altered fractional anisotropy and diffusivity on diffusion tensor imaging) (Karlsgodt et al., 2012; North, 2000) that could contribute to NF1-associated neurological abnormalities. While *Nf1* gene inactivation in murine models has been shown to result in increased numbers of oligodendrocyte progenitors (OPCs) (Bennett et al., 2003; Hegedus et al., 2007), the effects of *NF1* gene mutations on oligodendrocyte differentiation and function have not been assessed. Recently, cerebral organoid cultures (>100DIV) that incorporate factors to promote OPC survival and oligodendrocyte maturation have been shown to develop OPCs and myelinating oligodendrocytes (Kim et al., 2019; Madhavan et al., 2018; Marton et al., 2019). These iPSC-hCOs

could provide a unique experimental platform to investigate the cellular and molecular consequences of patient *NF1* mutations on oligodendrogenesis and myelination.

### ***Microglia***

The critical importance of microglia to brain development and homeostasis is underscored by numerous reports demonstrating that microglia regulate synaptic plasticity through pruning (Liu et al., 2017; Lui et al., 2016), as well as underlie some of the behavioral and cognitive abilities of rodents (Acharya et al., 2016; Rice et al., 2015). Studies have shown that mesoderm progenitors (Quadrato et al., 2017) and microglia (Ormel et al., 2018) develop spontaneously in hCOs generated without the use of inhibitors or molecular pathway manipulators. Based on these studies, we hypothesized that microglia were also present in CTL and *NF1*-mutant hiPSC-hCOs. Preliminary immunofluorescence experiments in CTL hCOs have revealed that IBA-1<sup>+</sup> cells develop in hCOs by 56DIV; however, the fraction of IBA-1<sup>+</sup> cells per organoid and between replicates was variable. Future experiments should confirm the cellular identity of the IBA-1<sup>+</sup> cells in hCOs using additional markers of microglia (*e.g.*, TMEM119, P2RY12 receptor) and critically evaluate whether the microglia population in control hCOs is representative of what is found in the normal human brain (0.5-16.6% of all cells) (Mittelbronn et al., 2001). If the microglia that spontaneously develop in hCOs are not representative of the normal human brain, future studies could incorporate hiPSC-microglia into cerebral organoids to assess the effects of microglia on *NF1*-associated brain pathologies. Advances in iPSC reprogramming now enable the generation of human microglia-like cells with expression profiles similar to both primary fetal and adult microglia (Abud et al., 2017; Muffat et al., 2016).

### ***Brain tumors***

Optic pathway gliomas (OPGs) are seen in 15-20% of children with NF1 and are almost never biopsied as part of routine medical care (Jett and Friedman, 2010). As a result, much of our understanding of NF1-OPG pathogenesis derives from the use of *Nf1* genetically engineered mouse (GEM) models. Mice heterozygous for a germline *Nf1* gene mutation (Gutmann et al., 1999a), in which somatic *Nf1* loss occurs in neuroglial progenitors, develop optic gliomas (Bajenaru et al., 2002). Importantly, *Nf1* loss in neuroglial progenitor cells alone does not result in gliomagenesis. Tumor formation requires the presence of cells heterozygous for an inactivating *Nf1* gene mutation (Bajenaru et al., 2003). This finding suggests that *Nf1*<sup>+/-</sup> stromal cells are critical for tumor formation and maintenance (Bajenaru et al., 2003). One of these non-neoplastic cell types in these tumors are microglia, immune system-like cells that mature within the developing brain (Ginhoux et al., 2013). Formal proof for the critical role for microglia in murine optic glioma formation and maintenance derives from studies in which pharmacologic or genetic inhibition of microglial function is sufficient to delay tumorigenesis and reduce tumor proliferation, respectively (Daginakatte and Gutmann, 2007; Pong et al., 2013; Solga et al., 2015).

While these mouse tumors share many of the histologic and biologic features of their human counterparts, there are important differences. One difference relates to the level of microglial enrichment in gliomas, which is much smaller in mice (~10-15%) relative to most human NF1-low grade gliomas (35-50%) (Simmons et al., 2011). Future studies using 3D mixed cultures containing *NF1*-deficient human neuroglial progenitor cells in combination with heterozygous *NF1*-mutant iPSC-stromal cells may reveal new targets for future stroma-directed low-grade

glioma treatments. In this regard, the Gutmann Laboratory has engineered representative homozygous *NF1*-mutant (*NF1* null) hiPSC lines. Preliminary experiments have employed mixed organoids, in which 1-10% of starting cells were *NF1* null and 90-99% of starting cells were heterozygous for a patient *NF1* gene mutation, to assess for histological characteristics of low-grade gliomas (*e.g.*, increased cellularity, increased proliferation, gliogenesis and tissue disorganization). However, microglia were not assessed in these preliminary co-cultures. Further optimization of these co-culture platforms will potentially allow for more detailed characterization of host-specific tumor pathophysiology and could serve as a tractable preclinical platform for drug development and screening.

## 4.4 Concluding Remarks

The findings presented in this dissertation advance our understanding of the key determinants that account for differences between individuals with NF1-associated neurodevelopmental abnormalities. Collectively, these studies lay the foundation for future preclinical research using human iPSCs and cerebral organoids for NF1 precision medicine. As the number of NF1 patient-derived iPSCs grows, one could envision the creation of an international repository for high-throughput cellular and molecular phenotyping. The use of patient-derived iPSCs, in conjunction with credentialed small-animal disease models, offers unprecedented opportunities to discover subgroups of patients most likely to exhibit specific NF1 clinical features or respond to specific therapies. This “fingerprinting” approach might facilitate the identification of individuals at greatest risk for specific symptomatology in NF1, as well as the development of personalized therapeutic strategies.

# References

Abrahams, B.S., Arking, D.E., Campbell, D.B., Mefford, H.C., Morrow, E.M., Weiss, L.A., Menashe, I., Wadkins, T., Banerjee-Basu, S., and Packer, A. (2013). SFARI Gene 2.0: a community-driven knowledgebase for the autism spectrum disorders (ASDs). *Molecular autism* 4, 36.

Abud, E.M., Ramirez, R.N., Martinez, E.S., Healy, L.M., Nguyen, C.H.H., Newman, S.A., Yeromin, A.V., Scarfone, V.M., Marsh, S.E., Fimbres, C., *et al.* (2017). iPSC-Derived Human Microglia-like Cells to Study Neurological Diseases. *Neuron* 94, 278-293 e279.

Acharya, M.M., Green, K.N., Allen, B.D., Najafi, A.R., Syage, A., Minasyan, H., Le, M.T., Kawashita, T., Giedzinski, E., Parihar, V.K., *et al.* (2016). Elimination of microglia improves cognitive function following cranial irradiation. *Scientific reports* 6, 31545.

Anastasaki, C., Morris, S.M., Gao, F., and Gutmann, D.H. (2017). Children with 5'-end NF1 gene mutations are more likely to have glioma. *Neurology Genetics* 3, e192.

Anastasaki, C., Wegscheid, M.L., Hartigan, K., Papke, J.B., Kopp, N.D., Chen, J., Cobb, O., Dougherty, J.D., and Gutmann, D.H. (2020). Human iPSC-Derived Neurons and Cerebral Organoids Establish Differential Effects of Germline NF1 Gene Mutations. *Stem cell reports*.

Anastasaki, C., Woo, A.S., Messiaen, L.M., and Gutmann, D.H. (2015). Elucidating the impact of neurofibromatosis-1 germline mutations on neurofibromin function and dopamine-based learning. *Human molecular genetics* 24, 3518-3528.

Arikkath, J., Peng, I.F., Ng, Y.G., Israely, I., Liu, X., Ullian, E.M., and Reichardt, L.F. (2009). Delta-catenin regulates spine and synapse morphogenesis and function in hippocampal neurons during development. *The Journal of neuroscience : the official journal of the Society for Neuroscience* 29, 5435-5442.

Arun, V., Wiley, J.C., Kaur, H., Kaplan, D.R., and Guha, A. (2013). A novel neurofibromin (NF1) interaction with the leucine-rich pentatricopeptide repeat motif-containing protein links neurofibromatosis type 1 and the French Canadian variant of Leigh's syndrome in a common molecular complex. *J Neurosci Res* 91, 494-505.

Ashburner, M., Ball, C.A., Blake, J.A., Botstein, D., Butler, H., Cherry, J.M., Davis, A.P., Dolinski, K., Dwight, S.S., Eppig, J.T., *et al.* (2000). Gene ontology: tool for the unification of biology. The Gene Ontology Consortium. *Nature genetics* 25, 25-29.

Bajenaru, M.L., Hernandez, M.R., Perry, A., Zhu, Y., Parada, L.F., Garbow, J.R., and Gutmann, D.H. (2003). Optic nerve glioma in mice requires astrocyte Nf1 gene inactivation and Nf1 brain heterozygosity. *Cancer research* 63, 8573-8577.

Bajenaru, M.L., Zhu, Y., Hedrick, N.M., Donahoe, J., Parada, L.F., and Gutmann, D.H. (2002). Astrocyte-specific inactivation of the neurofibromatosis 1 gene (NF1) is insufficient for astrocytoma formation. *Mol Cell Biol* 22, 5100-5113.

Banerjee-Basu, S., and Packer, A. (2010). SFARI Gene: an evolving database for the autism research community. *Disease models & mechanisms* 3, 133-135.

Bell, C.C., Magor, G.W., Gillinder, K.R., and Perkins, A.C. (2014). A high-throughput screening strategy for detecting CRISPR-Cas9 induced mutations using next-generation sequencing. *BMC Genomics* 15, 1002.

Bennett, M.R., Rizvi, T.A., Karyala, S., McKinnon, R.D., and Ratner, N. (2003). Aberrant growth and differentiation of oligodendrocyte progenitors in neurofibromatosis type 1 mutants. *The Journal of neuroscience : the official journal of the Society for Neuroscience* 23, 7207-7217.

Bershteyn, M., Nowakowski, T.J., Pollen, A.A., Di Lullo, E., Nene, A., Wynshaw-Boris, A., and Kriegstein, A.R. (2017). Human iPSC-Derived Cerebral Organoids Model Cellular Features of Lissencephaly and Reveal Prolonged Mitosis of Outer Radial Glia. *Cell stem cell* 20, 435-449.e434.

Bolcekova, A., Nemethova, M., Zatkova, A., Hlinkova, K., Pozgayova, S., Hlavata, A., Kadasi, L., Durovcikova, D., Gerinec, A., Husakova, K., *et al.* (2013). Clustering of mutations in the 5' tertile of the NF1 gene in Slovakia patients with optic pathway glioma. *Neoplasma* 60, 655-665.

Bollag, G., McCormick, F., and Clark, R. (1993). Characterization of full-length neurofibromin: tubulin inhibits Ras GAP activity. *The EMBO journal* 12, 1923-1927.

Boyanapalli, M., Lahoud, O.B., Messiaen, L., Kim, B., Anderle de Saylor, M.S., Duckett, S.J., Somara, S., and Mikol, D.D. (2006). Neurofibromin binds to caveolin-1 and regulates ras, FAK, and Akt. *Biochem Biophys Res Commun* 340, 1200-1208.

Brennand, K.J., Simone, A., Jou, J., Gelboin-Burkhart, C., Tran, N., Sangar, S., Li, Y., Mu, Y., Chen, G., Yu, D., *et al.* (2011). Modelling schizophrenia using human induced pluripotent stem cells. *Nature* 473, 221-225.

Camp, J.G., Badsha, F., Florio, M., Kanton, S., Gerber, T., Wilsch-Brauninger, M., Lewitus, E., Sykes, A., Hevers, W., Lancaster, M., *et al.* (2015). Human cerebral organoids recapitulate gene expression programs of fetal neocortex development. *Proceedings of the National Academy of Sciences of the United States of America* *112*, 15672-15677.

Chen, H.M., DeLong, C.J., Bame, M., Rajapakse, I., Herron, T.J., McInnis, M.G., and O'Shea, K.S. (2014). Transcripts involved in calcium signaling and telencephalic neuronal fate are altered in induced pluripotent stem cells from bipolar disorder patients. *Translational psychiatry* *4*, e375.

Chen, Y.H., Gianino, S.M., and Gutmann, D.H. (2015). Neurofibromatosis-1 regulation of neural stem cell proliferation and multilineage differentiation operates through distinct RAS effector pathways. *Genes & development* *29*, 1677-1682.

Coe, B.P., Stessman, H.A.F., Sulovari, A., Geisheker, M.R., Bakken, T.E., Lake, A.M., Dougherty, J.D., Lein, E.S., Hormozdiari, F., Bernier, R.A., *et al.* (2019). Neurodevelopmental disease genes implicated by de novo mutation and copy number variation morbidity. *Nature genetics* *51*, 106-116.

Constantino, J.N., Zhang, Y., Holzhauer, K., Sant, S., Long, K., Vallorani, A., Malik, L., and Gutmann, D.H. (2015). Distribution and Within-Family Specificity of Quantitative Autistic Traits in Patients with Neurofibromatosis Type I. *J Pediatr* *167*, 621-626 e621.

Costa, R.M., Federov, N.B., Kogan, J.H., Murphy, G.G., Stern, J., Ohno, M., Kucherlapati, R., Jacks, T., and Silva, A.J. (2002). Mechanism for the learning deficits in a mouse model of neurofibromatosis type 1. *Nature* *415*, 526-530.

Cui, Y., Costa, R.M., Murphy, G.G., Elgersma, Y., Zhu, Y., Gutmann, D.H., Parada, L.F., Mody, I., and Silva, A.J. (2008). Neurofibromin regulation of ERK signaling modulates GABA release and learning. *Cell* *135*, 549-560.

Daginakatte, G.C., and Gutmann, D.H. (2007). Neurofibromatosis-1 (Nf1) heterozygous brain microglia elaborate paracrine factors that promote Nf1-deficient astrocyte and glioma growth. *Human molecular genetics* *16*, 1098-1112.

De Raedt, T., Beert, E., Pasmant, E., Luscan, A., Brems, H., Ortonne, N., Helin, K., Hornick, J.L., Mautner, V., Kehrer-Sawatzki, H., *et al.* (2014). PRC2 loss amplifies Ras-driven transcription and confers sensitivity to BRD4-based therapies. *Nature* *514*, 247-251.

De Schepper, S., Boucneau, J.M., Westbroek, W., Mommaas, M., Onderwater, J., Messiaen, L., Naeyaert, J.M., and Lambert, J.L. (2006). Neurofibromatosis type 1 protein and amyloid precursor protein interact in normal human melanocytes and colocalize with melanosomes. *J Invest Dermatol* *126*, 653-659.



Deraredj Nadim, W., Chaumont-Dubel, S., Madouri, F., Cobret, L., De Tauzia, M.L., Zajdel, P., Benedetti, H., Marin, P., and Morisset-Lopez, S. (2016). Physical interaction between neurofibromin and serotonin 5-HT6 receptor promotes receptor constitutive activity. *Proceedings of the National Academy of Sciences of the United States of America* 113, 12310-12315.

Descheemaeker, M.J., Roelandts, K., De Raedt, T., Brems, H., Fryns, J.P., and Legius, E. (2004). Intelligence in individuals with a neurofibromatosis type 1 microdeletion. *American journal of medical genetics Part A* 131, 325-326.

Dobin, A., Davis, C.A., Schlesinger, F., Drenkow, J., Zaleski, C., Jha, S., Batut, P., Chaisson, M., and Gingeras, T.R. (2013). STAR: ultrafast universal RNA-seq aligner. *Bioinformatics* 29, 15-21.

Dombi, E., Baldwin, A., Marcus, L.J., Fisher, M.J., Weiss, B., Kim, A., Whitcomb, P., Martin, S., Aschbacher-Smith, L.E., Rizvi, T.A., *et al.* (2016). Activity of Selumetinib in Neurofibromatosis Type 1-Related Plexiform Neurofibromas. *N Engl J Med* 375, 2550-2560.

Dougherty, K.D., Dreyfus, C.F., and Black, I.B. (2000). Brain-derived neurotrophic factor in astrocytes, oligodendrocytes, and microglia/macrophages after spinal cord injury. *Neurobiol Dis* 7, 574-585.

Douglas, J., Cilliers, D., Coleman, K., Tatton-Brown, K., Barker, K., Bernhard, B., Burn, J., Huson, S., Josifova, D., Lacombe, D., *et al.* (2007). Mutations in RNF135, a gene within the NF1 microdeletion region, cause phenotypic abnormalities including overgrowth. *Nature genetics* 39, 963-965.

Elia, L.P., Yamamoto, M., Zang, K., and Reichardt, L.F. (2006). p120 catenin regulates dendritic spine and synapse development through Rho-family GTPases and cadherins. *Neuron* 51, 43-56.

Feng, L., Yunoue, S., Tokuo, H., Ozawa, T., Zhang, D., Patrakitkomjorn, S., Ichimura, T., Saya, H., and Araki, N. (2004). PKA phosphorylation and 14-3-3 interaction regulate the function of neurofibromatosis type I tumor suppressor, neurofibromin. *FEBS Lett* 557, 275-282.

Fisher, M.J., Belzberg, A.J., de Blank, P., De Raedt, T., Elefteriou, F., Ferner, R.E., Giovannini, M., Harris, G.J., Kalamarides, M., Karajannis, M.A., *et al.* (2018). 2016 Children's Tumor Foundation conference on neurofibromatosis type 1, neurofibromatosis type 2, and schwannomatosis. *American journal of medical genetics Part A* 176, 1258-1269.

Frega, M., Linda, K., Keller, J.M., Gumus-Akay, G., Mossink, B., van Rhijn, J.R., Negwer, M., Klein Gunnewiek, T., Foreman, K., Kompier, N., *et al.* (2019). Neuronal network

dysfunction in a model for Kleefstra syndrome mediated by enhanced NMDAR signaling. *Nature communications* *10*, 4928.

Fukata, M., and Kaibuchi, K. (2001). Rho-family GTPases in cadherin-mediated cell-cell adhesion. *Nature reviews Molecular cell biology* *2*, 887-897.

Gao, R., and Penzes, P. (2015). Common mechanisms of excitatory and inhibitory imbalance in schizophrenia and autism spectrum disorders. *Current molecular medicine* *15*, 146-167.

Gilbert, J., and Man, H.Y. (2016). The X-Linked Autism Protein KIAA2022/KIDLIA Regulates Neurite Outgrowth via N-Cadherin and delta-Catenin Signaling. *eNeuro* *3*.

Ginhoux, F., Lim, S., Hoeffel, G., Low, D., and Huber, T. (2013). Origin and differentiation of microglia. *Frontiers in cellular neuroscience* *7*, 45.

Grayton, H.M., Fernandes, C., Rujescu, D., and Collier, D.A. (2012). Copy number variations in neurodevelopmental disorders. *Progress in neurobiology* *99*, 81-91.

Guo, X., Pan, Y., and Gutmann, D.H. (2019). Genetic and genomic alterations differentially dictate low-grade glioma growth through cancer stem cell-specific chemokine recruitment of T cells and microglia. *Neuro-oncology* *21*, 1250-1262.

Gutmann, D.H., Loehr, A., Zhang, Y., Kim, J., Henkemeyer, M., and Cashen, A. (1999a). Haploinsufficiency for the neurofibromatosis 1 (NF1) tumor suppressor results in increased astrocyte proliferation. *Oncogene* *18*, 4450-4459.

Gutmann, D.H., Zhang, Y., and Hirbe, A. (1999b). Developmental regulation of a neuron-specific neurofibromatosis 1 isoform. *Annals of neurology* *46*, 777-782.

Hahn, N., Buschgens, L., Schwedhelm-Domeyer, N., Bank, S., Geurten, B.R.H., Neugebauer, P., Massih, B., Gopfert, M.C., and Heinrich, R. (2019). The Orphan Cytokine Receptor CRLF3 Emerged With the Origin of the Nervous System and Is a Neuroprotective Erythropoietin Receptor in Locusts. *Frontiers in molecular neuroscience* *12*, 251.

Hahn, N., Knorr, D.Y., Liebig, J., Wustefeld, L., Peters, K., Buscher, M., Bucher, G., Ehrenreich, H., and Heinrich, R. (2017). The Insect Ortholog of the Human Orphan Cytokine Receptor CRLF3 Is a Neuroprotective Erythropoietin Receptor. *Frontiers in molecular neuroscience* *10*, 223.

Hegedus, B., Dasgupta, B., Shin, J.E., Emmett, R.J., Hart-Mahon, E.K., Elghazi, L., Bernal-Mizrachi, E., and Gutmann, D.H. (2007). Neurofibromatosis-1 regulates neuronal and glial cell

differentiation from neuroglial progenitors in vivo by both cAMP- and Ras-dependent mechanisms. *Cell stem cell* *1*, 443-457.

Hensley, K., Christov, A., Kamat, S., Zhang, X.C., Jackson, K.W., Snow, S., and Post, J. (2010). Proteomic identification of binding partners for the brain metabolite lanthionine ketimine (LK) and documentation of LK effects on microglia and motoneuron cell cultures. *The Journal of neuroscience : the official journal of the Society for Neuroscience* *30*, 2979-2988.

Hsueh, Y.P., Roberts, A.M., Volta, M., Sheng, M., and Roberts, R.G. (2001). Bipartite interaction between neurofibromatosis type I protein (neurofibromin) and syndecan transmembrane heparan sulfate proteoglycans. *The Journal of neuroscience : the official journal of the Society for Neuroscience* *21*, 3764-3770.

Huch, M., and Koo, B.K. (2015). Modeling mouse and human development using organoid cultures. *Development (Cambridge, England)* *142*, 3113-3125.

Hutsler, J.J., and Zhang, H. (2010). Increased dendritic spine densities on cortical projection neurons in autism spectrum disorders. *Brain research* *1309*, 83-94.

Hyman, S.L., Arthur Shores, E., and North, K.N. (2006). Learning disabilities in children with neurofibromatosis type 1: subtypes, cognitive profile, and attention-deficit-hyperactivity disorder. *Developmental medicine and child neurology* *48*, 973-977.

Hyman, S.L., Shores, A., and North, K.N. (2005). The nature and frequency of cognitive deficits in children with neurofibromatosis type 1. *Neurology* *65*, 1037-1044.

Janssens, S., Schotsaert, M., Manganaro, L., Dejosez, M., Simon, V., Garcia-Sastre, A., and Zwaka, T.P. (2019). FACS-Mediated Isolation of Neuronal Cell Populations From Virus-Infected Human Embryonic Stem Cell-Derived Cerebral Organoid Cultures. *Current protocols in stem cell biology* *48*, e65.

Jett, K., and Friedman, J.M. (2010). Clinical and genetic aspects of neurofibromatosis 1. *Genetics in medicine : official journal of the American College of Medical Genetics* *12*, 1-11.

Joo, K.M., Kim, J., Jin, J., Kim, M., Seol, H.J., Muradov, J., Yang, H., Choi, Y.L., Park, W.Y., Kong, D.S., *et al.* (2013). Patient-specific orthotopic glioblastoma xenograft models recapitulate the histopathology and biology of human glioblastomas in situ. *Cell reports* *3*, 260-273.

Kaplan, M.R., Meyer-Franke, A., Lambert, S., Bennett, V., Duncan, I.D., Levinson, S.R., and Barres, B.A. (1997). Induction of sodium channel clustering by oligodendrocytes. *Nature* *386*, 724-728.

Karlsgodt, K.H., Rosser, T., Lutkenhoff, E.S., Cannon, T.D., Silva, A., and Bearden, C.E. (2012). Alterations in white matter microstructure in neurofibromatosis-1. *PloS one* *7*, e47854.

Kaul, A., Toonen, J.A., Cimino, P.J., Gianino, S.M., and Gutmann, D.H. (2015). Akt- or MEK-mediated mTOR inhibition suppresses Nf1 optic glioma growth. *Neuro-oncology* *17*, 843-853.

Kehrer-Sawatzki, H., Mautner, V.F., and Cooper, D.N. (2017). Emerging genotype-phenotype relationships in patients with large NF1 deletions. *Human genetics* *136*, 349-376.

Kim, H., Xu, R., Padmashri, R., Dunaevsky, A., Liu, Y., Dreyfus, C.F., and Jiang, P. (2019). Pluripotent Stem Cell-Derived Cerebral Organoids Reveal Human Oligodendrogenesis with Dorsal and Ventral Origins. *Stem cell reports* *12*, 890-905.

Kluwe, L., Siebert, R., Gesk, S., Friedrich, R.E., Tinschert, S., Kehrer-Sawatzki, H., and Mautner, V.F. (2004). Screening 500 unselected neurofibromatosis 1 patients for deletions of the NF1 gene. *Hum Mutat* *23*, 111-116.

Koczkowska, M., Callens, T., Gomes, A., Sharp, A., Chen, Y., Hicks, A.D., Aylsworth, A.S., Azizi, A.A., Basel, D.G., Bellus, G., *et al.* (2018a). Expanding the clinical phenotype of individuals with a 3-bp in-frame deletion of the NF1 gene (c.2970\_2972del): an update of genotype-phenotype correlation. *Genetics in medicine : official journal of the American College of Medical Genetics*.

Koczkowska, M., Chen, Y., Callens, T., Gomes, A., Sharp, A., Johnson, S., Hsiao, M.C., Chen, Z., Balasubramanian, M., Barnett, C.P., *et al.* (2018b). Genotype-Phenotype Correlation in NF1: Evidence for a More Severe Phenotype Associated with Missense Mutations Affecting NF1 Codons 844-848. *American journal of human genetics* *102*, 69-87.

Korf, B.R. (2013). Neurofibromatosis. *Handbook of clinical neurology* *111*, 333-340.

Kweh, F., Zheng, M., Kurenova, E., Wallace, M., Golubovskaya, V., and Cance, W.G. (2009). Neurofibromin physically interacts with the N-terminal domain of focal adhesion kinase. *Mol Carcinog* *48*, 1005-1017.

Lancaster, M.A., Corsini, N.S., Wolfinger, S., Gustafson, E.H., Phillips, A.W., Burkard, T.R., Otani, T., Livesey, F.J., and Knoblich, J.A. (2017). Guided self-organization and cortical plate formation in human brain organoids. *Nature biotechnology* *35*, 659-666.

Lancaster, M.A., and Knoblich, J.A. (2014). Generation of cerebral organoids from human pluripotent stem cells. *Nature protocols* 9, 2329-2340.

Lancaster, M.A., Renner, M., Martin, C.A., Wenzel, D., Bicknell, L.S., Hurles, M.E., Homfray, T., Penninger, J.M., Jackson, A.P., and Knoblich, J.A. (2013). Cerebral organoids model human brain development and microcephaly. *Nature* 501, 373-379.

Lazar, M., Miles, L.M., Babb, J.S., and Donaldson, J.B. (2014). Axonal deficits in young adults with High Functioning Autism and their impact on processing speed. *NeuroImage Clinical* 4, 417-425.

Lee, C.T., Chen, J., Kindberg, A.A., Bendriem, R.M., Spivak, C.E., Williams, M.P., Richie, C.T., Handreck, A., Mallon, B.S., Lupica, C.R., *et al.* (2016). CYP3A5 Mediates Effects of Cocaine on Human Neocortigenesis: Studies using an In Vitro 3D Self-Organized hPSC Model with a Single Cortex-Like Unit. *Neuropsychopharmacology* : official publication of the American College of Neuropsychopharmacology.

Lee, D.Y., Yeh, T.H., Emmett, R.J., White, C.R., and Gutmann, D.H. (2010). Neurofibromatosis-1 regulates neuroglial progenitor proliferation and glial differentiation in a brain region-specific manner. *Genes & development* 24, 2317-2329.

Lee, W., Teckie, S., Wiesner, T., Ran, L., Prieto Granada, C.N., Lin, M., Zhu, S., Cao, Z., Liang, Y., Sboner, A., *et al.* (2014). PRC2 is recurrently inactivated through EED or SUZ12 loss in malignant peripheral nerve sheath tumors. *Nature genetics* 46, 1227-1232.

Li, K., Turner, A.N., Chen, M., Brosius, S.N., Schoeb, T.R., Messiaen, L.M., Bedwell, D.M., Zinn, K.R., Anastasaki, C., Gutmann, D.H., *et al.* (2016). Mice with missense and nonsense NF1 mutations display divergent phenotypes compared with human neurofibromatosis type I. *Disease models & mechanisms* 9, 759-767.

Liu, Y., Liu, H., Sauvey, C., Yao, L., Zarnowska, E.D., and Zhang, S.C. (2013). Directed differentiation of forebrain GABA interneurons from human pluripotent stem cells. *Nature protocols* 8, 1670-1679.

Liu, Y., Zhou, L.J., Wang, J., Li, D., Ren, W.J., Peng, J., Wei, X., Xu, T., Xin, W.J., Pang, R.P., *et al.* (2017). TNF-alpha Differentially Regulates Synaptic Plasticity in the Hippocampus and Spinal Cord by Microglia-Dependent Mechanisms after Peripheral Nerve Injury. *The Journal of neuroscience* : the official journal of the Society for Neuroscience 37, 871-881.

Love, M.I., Huber, W., and Anders, S. (2014). Moderated estimation of fold change and dispersion for RNA-seq data with DESeq2. *Genome Biol* 15, 550.

Lui, H., Zhang, J., Makinson, S.R., Cahill, M.K., Kelley, K.W., Huang, H.Y., Shang, Y., Oldham, M.C., Martens, L.H., Gao, F., *et al.* (2016). Progranulin Deficiency Promotes Circuit-Specific Synaptic Pruning by Microglia via Complement Activation. *Cell* *165*, 921-935.

Luo, C., Lancaster, M.A., Castanon, R., Nery, J.R., Knoblich, J.A., and Ecker, J.R. (2016). Cerebral Organoids Recapitulate Epigenomic Signatures of the Human Fetal Brain. *Cell reports* *17*, 3369-3384.

Madhavan, M., Nevin, Z.S., Shick, H.E., Garrison, E., Clarkson-Paredes, C., Karl, M., Clayton, B.L.L., Factor, D.C., Allan, K.C., Barbar, L., *et al.* (2018). Induction of myelinating oligodendrocytes in human cortical spheroids. *Nature methods* *15*, 700-706.

Makalowski, W., Zhang, J., and Boguski, M.S. (1996). Comparative analysis of 1196 orthologous mouse and human full-length mRNA and protein sequences. *Genome research* *6*, 846-857.

Marchetto, M.C., Carromeu, C., Acab, A., Yu, D., Yeo, G.W., Mu, Y., Chen, G., Gage, F.H., and Muotri, A.R. (2010). A model for neural development and treatment of Rett syndrome using human induced pluripotent stem cells. *Cell* *143*, 527-539.

Mariani, J., Coppola, G., Zhang, P., Abyzov, A., Provini, L., Tomasini, L., Amenduni, M., Szekely, A., Palejev, D., Wilson, M., *et al.* (2015). FOXP1-Dependent Dysregulation of GABA/Glutamate Neuron Differentiation in Autism Spectrum Disorders. *Cell* *162*, 375-390.

Martin, G.A., Viskochil, D., Bollag, G., McCabe, P.C., Crosier, W.J., Haubruck, H., Conroy, L., Clark, R., O'Connell, P., Cawthon, R.M., *et al.* (1990). The GAP-related domain of the neurofibromatosis type 1 gene product interacts with ras p21. *Cell* *63*, 843-849.

Marton, R.M., Miura, Y., Sloan, S.A., Li, Q., Revah, O., Levy, R.J., Huguenard, J.R., and Pasca, S.P. (2019). Differentiation and maturation of oligodendrocytes in human three-dimensional neural cultures. *Nature neuroscience* *22*, 484-491.

Matter, C., Pribadi, M., Liu, X., and Trachtenberg, J.T. (2009). Delta-catenin is required for the maintenance of neural structure and function in mature cortex in vivo. *Neuron* *64*, 320-327.

Mautner, V.F., Kluwe, L., Friedrich, R.E., Roehl, A.C., Bammert, S., Hogel, J., Spori, H., Cooper, D.N., and Kehrer-Sawatzki, H. (2010). Clinical characterisation of 29 neurofibromatosis type-1 patients with molecularly ascertained 1.4 Mb type-1 NF1 deletions. *Journal of medical genetics* *47*, 623-630.

Messiaen, L., Vogt, J., Bengesser, K., Fu, C., Mikhail, F., Serra, E., Garcia-Linares, C., Cooper, D.N., Lazaro, C., and Kehrer-Sawatzki, H. (2011). Mosaic type-1 NF1 microdeletions

as a cause of both generalized and segmental neurofibromatosis type-1 (NF1). *Hum Mutat* 32, 213-219.

Mittelbronn, M., Dietz, K., Schluesener, H.J., and Meyermann, R. (2001). Local distribution of microglia in the normal adult human central nervous system differs by up to one order of magnitude. *Acta Neuropathol* 101, 249-255.

Molnar, Z., Vasistha, N.A., and Garcia-Moreno, F. (2011). Hanging by the tail: progenitor populations proliferate. *Nature neuroscience* 14, 538-540.

Monzel, A.S., Smits, L.M., Hemmer, K., Hachi, S., Moreno, E.L., van Wuellem, T., Jarazo, J., Walter, J., Bruggemann, I., Boussaad, I., *et al.* (2017). Derivation of Human Midbrain-Specific Organoids from Neuroepithelial Stem Cells. *Stem cell reports* 8, 1144-1154.

Mor-Shaked, H., and Eiges, R. (2016). Modeling Fragile X Syndrome Using Human Pluripotent Stem Cells. *Genes* 7.

Morris, S.M., Acosta, M.T., Garg, S., Green, J., Huson, S., Legius, E., North, K.N., Payne, J.M., Plasschaert, E., Frazier, T.W., *et al.* (2016a). Disease Burden and Symptom Structure of Autism in Neurofibromatosis Type 1: A Study of the International NF1-ASD Consortium Team (INFACT). *JAMA psychiatry*.

Morris, S.M., Acosta, M.T., Garg, S., Green, J., Huson, S., Legius, E., North, K.N., Payne, J.M., Plasschaert, E., Frazier, T.W., *et al.* (2016b). Disease Burden and Symptom Structure of Autism in Neurofibromatosis Type 1: A Study of the International NF1-ASD Consortium Team (INFACT). *JAMA Psychiatry* 73, 1276-1284.

Morris, S.M., and Gutmann, D.H. (2018). A genotype-phenotype correlation for quantitative autistic trait burden in neurofibromatosis 1. *Neurology* 90, 377-379.

Muffat, J., Li, Y., Yuan, B., Mitalipova, M., Omer, A., Corcoran, S., Bakiasi, G., Tsai, L.H., Aubourg, P., Ransohoff, R.M., *et al.* (2016). Efficient derivation of microglia-like cells from human pluripotent stem cells. *Nature medicine* 22, 1358-1367.

Mukaetova-Ladinska, E.B., Arnold, H., Jaros, E., Perry, R., and Perry, E. (2004). Depletion of MAP2 expression and laminar cytoarchitectonic changes in dorsolateral prefrontal cortex in adult autistic individuals. *Neuropathol Appl Neurobiol* 30, 615-623.

North, K. (2000). Neurofibromatosis type 1. *Am J Med Genet* 97, 119-127.

Omrani, A., van der Vaart, T., Mientjes, E., van Woerden, G.M., Hojjati, M.R., Li, K.W., Gutmann, D.H., Levelt, C.N., Smit, A.B., Silva, A.J., *et al.* (2015). HCN channels are a novel

therapeutic target for cognitive dysfunction in Neurofibromatosis type 1. *Molecular psychiatry* 20, 1311-1321.

Ormel, P.R., Vieira de Sa, R., van Bodegraven, E.J., Karst, H., Harschnitz, O., Sneeboer, M.A.M., Johansen, L.E., van Dijk, R.E., Scheefhals, N., Berdenis van Berlekom, A., *et al.* (2018). Microglia innately develop within cerebral organoids. *Nature communications* 9, 4167.

Ostrowski, D., and Heinrich, R. (2018). Alternative Erythropoietin Receptors in the Nervous System. *J Clin Med* 7.

Ottenhoff, M.J., Rietman, A.B., Mous, S.E., Plasschaert, E., Gawehns, D., Brems, H., Oostenbrink, R., Team, E.-N., van Minkelen, R., Nellist, M., *et al.* (2020). Examination of the genetic factors underlying the cognitive variability associated with neurofibromatosis type 1. *Genetics in medicine : official journal of the American College of Medical Genetics*.

Papadopoulos, J.S., and Agarwala, R. (2007). COBALT: constraint-based alignment tool for multiple protein sequences. *Bioinformatics* 23, 1073-1079.

Partek Inc (2020). Partek® Flow® software, version 9.0 Copyright © (St. Louis, MO, USA).

Pasca, A.M., Sloan, S.A., Clarke, L.E., Tian, Y., Makinson, C.D., Huber, N., Kim, C.H., Park, J.Y., O'Rourke, N.A., Nguyen, K.D., *et al.* (2015). Functional cortical neurons and astrocytes from human pluripotent stem cells in 3D culture. *Nature methods* 12, 671-678.

Pasmant, E., Sabbagh, A., Spurlock, G., Laurendeau, I., Grillo, E., Hamel, M.J., Martin, L., Barbarot, S., Leheup, B., Rodriguez, D., *et al.* (2010). NF1 microdeletions in neurofibromatosis type 1: from genotype to phenotype. *Hum Mutat* 31, E1506-1518.

Patrakitkomjorn, S., Kobayashi, D., Morikawa, T., Wilson, M.M., Tsubota, N., Irie, A., Ozawa, T., Aoki, M., Arimura, N., Kaibuchi, K., *et al.* (2008). Neurofibromatosis type 1 (NF1) tumor suppressor, neurofibromin, regulates the neuronal differentiation of PC12 cells via its associating protein, CRMP-2. *The Journal of biological chemistry* 283, 9399-9413.

Phan, V.T., Ding, V.W., Li, F., Chalkley, R.J., Burlingame, A., and McCormick, F. (2010). The RasGAP proteins Ira2 and neurofibromin are negatively regulated by Gpb1 in yeast and ETEA in humans. *Mol Cell Biol* 30, 2264-2279.

Pinna, V., Lanari, V., Daniele, P., Consoli, F., Agolini, E., Margiotti, K., Bottillo, I., Torrente, I., Bruselles, A., Fusilli, C., *et al.* (2015). p.Arg1809Cys substitution in neurofibromin is associated with a distinctive NF1 phenotype without neurofibromas. *European Journal of Human Genetics* 23, 1068-1071.



Pong, W.W., Higer, S.B., Gianino, S.M., Emmett, R.J., and Gutmann, D.H. (2013). Reduced microglial CX3CR1 expression delays neurofibromatosis-1 glioma formation. *Annals of neurology* 73, 303-308.

Pucilowska, J., Vithayathil, J., Pagani, M., Kelly, C., Karlo, J.C., Robol, C., Morella, I., Gozzi, A., Brambilla, R., and Landreth, G.E. (2018). Pharmacological Inhibition of ERK Signaling Rescues Pathophysiology and Behavioral Phenotype Associated with 16p11.2 Chromosomal Deletion in Mice. *The Journal of neuroscience : the official journal of the Society for Neuroscience* 38, 6640-6652.

Qian, X., Nguyen, H.N., Song, M.M., Hadiono, C., Ogden, S.C., Hammack, C., Yao, B., Hamersky, G.R., Jacob, F., Zhong, C., *et al.* (2016a). Brain-Region-Specific Organoids Using Mini-bioreactors for Modeling ZIKV Exposure. *Cell* 165, 1238-1254.

Qian, X., Nguyen, H.N., Song, M.M., Hadiono, C., Ogden, S.C., Hammack, C., Yao, B., Hamersky, G.R., Jacob, F., Zhong, C., *et al.* (2016b). Brain-Region-Specific Organoids Using Mini-bioreactors for Modeling ZIKV Exposure. *Cell* 165, 1238-1254.

Quadrato, G., Brown, J., and Arlotta, P. (2016). The promises and challenges of human brain organoids as models of neuropsychiatric disease. *Nature medicine* 22, 1220-1228.

Quadrato, G., Nguyen, T., Macosko, E.Z., Sherwood, J.L., Min Yang, S., Berger, D.R., Maria, N., Scholvin, J., Goldman, M., Kinney, J.P., *et al.* (2017). Cell diversity and network dynamics in photosensitive human brain organoids. *Nature* 545, 48-53.

Ramocki, M.B., Bartnik, M., Szafranski, P., Kolodziejska, K.E., Xia, Z., Bravo, J., Miller, G.S., Rodriguez, D.L., Williams, C.A., Bader, P.I., *et al.* (2010). Recurrent distal 7q11.23 deletion including HIP1 and YWHAG identified in patients with intellectual disabilities, epilepsy, and neurobehavioral problems. *American journal of human genetics* 87, 857-865.

Rasmussen, S.A., Colman, S.D., Ho, V.T., Abernathy, C.R., Arn, P.H., Weiss, L., Schwartz, C., Saul, R.A., and Wallace, M.R. (1998). Constitutional and mosaic large NF1 gene deletions in neurofibromatosis type 1. *Journal of medical genetics* 35, 468-471.

Ratner, N., and Miller, S.J. (2015). A RASopathy gene commonly mutated in cancer: the neurofibromatosis type 1 tumour suppressor. *Nature reviews Cancer* 15, 290-301.

Rice, R.A., Spangenberg, E.E., Yamate-Morgan, H., Lee, R.J., Arora, R.P., Hernandez, M.X., Tenner, A.J., West, B.L., and Green, K.N. (2015). Elimination of Microglia Improves Functional Outcomes Following Extensive Neuronal Loss in the Hippocampus. *The Journal of neuroscience : the official journal of the Society for Neuroscience* 35, 9977-9989.

Richter, M., Murtaza, N., Scharrenberg, R., White, S.H., Johanns, O., Walker, S., Yuen, R.K.C., Schwanke, B., Bedurftig, B., Henis, M., *et al.* (2019). Altered TAOK2 activity causes autism-related neurodevelopmental and cognitive abnormalities through RhoA signaling. *Molecular psychiatry* 24, 1329-1350.

Rojnueangnit, K., Xie, J., Gomes, A., Sharp, A., Callens, T., Chen, Y., Liu, Y., Cochran, M., Abbott, M.A., Atkin, J., *et al.* (2015). High Incidence of Noonan Syndrome Features Including Short Stature and Pulmonic Stenosis in Patients carrying NF1 Missense Mutations Affecting p.Arg1809: Genotype-Phenotype Correlation. *Hum Mutat* 36, 1052-1063.

Sanchez-Ortiz, E., Cho, W., Nazarenko, I., Mo, W., Chen, J., and Parada, L.F. (2014). NF1 regulation of RAS/ERK signaling is required for appropriate granule neuron progenitor expansion and migration in cerebellar development. *Genes & development* 28, 2407-2420.

Semple, B.D., Blomgren, K., Gimlin, K., Ferriero, D.M., and Noble-Haeusslein, L.J. (2013). Brain development in rodents and humans: Identifying benchmarks of maturation and vulnerability to injury across species. *Progress in neurobiology* 106-107, 1-16.

Sharif, S., Upadhyaya, M., Ferner, R., Majounie, E., Shenton, A., Baser, M., Thakker, N., and Evans, D.G. (2011). A molecular analysis of individuals with neurofibromatosis type 1 (NF1) and optic pathway gliomas (OPGs), and an assessment of genotype-phenotype correlations. *Journal of medical genetics* 48, 256-260.

Shcheglovitov, A., Shcheglovitova, O., Yazawa, M., Portmann, T., Shu, R., Sebastiano, V., Krawisz, A., Froehlich, W., Bernstein, J.A., Hallmayer, J.F., *et al.* (2013). SHANK3 and IGF1 restore synaptic deficits in neurons from 22q13 deletion syndrome patients. *Nature* 503, 267-271.

Sherekar, M., Han, S.W., Ghirlando, R., Messing, S., Drew, M., Rabara, D., Waybright, T., Juneja, P., O'Neill, H., Stanley, C.B., *et al.* (2020). Biochemical and structural analyses reveal that the tumor suppressor neurofibromin (NF1) forms a high-affinity dimer. *The Journal of biological chemistry* 295, 1105-1119.

Simmons, G.W., Pong, W.W., Emnett, R.J., White, C.R., Gianino, S.M., Rodriguez, F.J., and Gutmann, D.H. (2011). Neurofibromatosis-1 heterozygosity increases microglia in a spatially and temporally restricted pattern relevant to mouse optic glioma formation and growth. *Journal of neuropathology and experimental neurology* 70, 51-62.

Sloan, S.A., Andersen, J., Pasca, A.M., Birey, F., and Pasca, S.P. (2018). Generation and assembly of human brain region-specific three-dimensional cultures. *Nature protocols* 13, 2062-2085.

- Smith, A.M., and Dragunow, M. (2014). The human side of microglia. *Trends in neurosciences* 37, 125-135.
- Smithson, L.J., Anastasaki, C., Chen, R., Toonen, J.A., Williams, S.B., and Gutmann, D.H. (2016). Contextual signaling in cancer. *Seminars in cell & developmental biology* 58, 118-126.
- Solga, A.C., Pong, W.W., Kim, K.Y., Cimino, P.J., Toonen, J.A., Walker, J., Wylie, T., Magrini, V., Griffith, M., Griffith, O.L., *et al.* (2015). RNA Sequencing of Tumor-Associated Microglia Reveals Ccl5 as a Stromal Chemokine Critical for Neurofibromatosis-1 Glioma Growth. *Neoplasia (New York, NY)* 17, 776-788.
- Soucy, E.A., Wessel, L.E., Gao, F., Albers, A.C., Gutmann, D.H., and Dunn, C.M. (2015). A pilot study for evaluation of hypotonia in children with neurofibromatosis type 1. *Journal of child neurology* 30, 382-385.
- Stowe, I.B., Mercado, E.L., Stowe, T.R., Bell, E.L., Oses-Prieto, J.A., Hernandez, H., Burlingame, A.L., and McCormick, F. (2012). A shared molecular mechanism underlies the human rasopathies Legius syndrome and Neurofibromatosis-1. *Genes & development* 26, 1421-1426.
- Takahashi, K., Tanabe, K., Ohnuki, M., Narita, M., Ichisaka, T., Tomoda, K., and Yamanaka, S. (2007). Induction of pluripotent stem cells from adult human fibroblasts by defined factors. *Cell* 131, 861-872.
- Takahashi, K., and Yamanaka, S. (2006). Induction of pluripotent stem cells from mouse embryonic and adult fibroblast cultures by defined factors. *Cell* 126, 663-676.
- Tan, Z.J., Peng, Y., Song, H.L., Zheng, J.J., and Yu, X. (2010). N-cadherin-dependent neuron-neuron interaction is required for the maintenance of activity-induced dendrite growth. *Proceedings of the National Academy of Sciences of the United States of America* 107, 9873-9878.
- Tastet, J., Decalonne, L., Marouillat, S., Malvy, J., Thepault, R.A., Toutain, A., Paubel, A., Tabagh, R., Benedetti, H., Laumonnier, F., *et al.* (2015). Mutation screening of the ubiquitin ligase gene RNF135 in French patients with autism. *Psychiatr Genet* 25, 263-267.
- Tcw, J., Wang, M., Pimenova, A.A., Bowles, K.R., Hartley, B.J., Lacin, E., Machlovi, S.I., Abdelaal, R., Karch, C.M., Phatnani, H., *et al.* (2017). An Efficient Platform for Astrocyte Differentiation from Human Induced Pluripotent Stem Cells. *Stem cell reports* 9, 600-614.
- Tokuo, H., Yunoue, S., Feng, L., Kimoto, M., Tsuji, H., Ono, T., Saya, H., and Araki, N. (2001). Phosphorylation of neurofibromin by cAMP-dependent protein kinase is regulated via

a cellular association of N(G),N(G)-dimethylarginine dimethylaminohydrolase. *FEBS Lett* 494, 48-53.

Toonen, J.A., Anastasaki, C., Smithson, L.J., Gianino, S.M., Li, K., Kesterson, R.A., and Gutmann, D.H. (2016). NF1 germline mutation differentially dictates optic glioma formation and growth in neurofibromatosis-1. *Human molecular genetics* 25, 1703-1713.

Trevisson, E., Morbidoni, V., Forzan, M., Daolio, C., Fumini, V., Parrozzani, R., Cassina, M., Midena, E., Salviati, L., and Clementi, M. (2019). The Arg1038Gly missense variant in the NF1 gene causes a mild phenotype without neurofibromas. *Mol Genet Genomic Med*, e616.

Trujillo, C.A., Gao, R., Negraes, P.D., Gu, J., Buchanan, J., Preissl, S., Wang, A., Wu, W., Haddad, G.G., Chaim, I.A., *et al.* (2019). Complex Oscillatory Waves Emerging from Cortical Organoids Model Early Human Brain Network Development. *Cell stem cell* 25, 558-569 e557.

Turner, T.N., Sharma, K., Oh, E.C., Liu, Y.P., Collins, R.L., Sosa, M.X., Auer, D.R., Brand, H., Sanders, S.J., Moreno-De-Luca, D., *et al.* (2015). Loss of delta-catenin function in severe autism. *Nature* 520, 51-56.

Upadhyaya, M., Huson, S.M., Davies, M., Thomas, N., Chuzhanova, N., Giovannini, S., Evans, D.G., Howard, E., Kerr, B., Griffiths, S., *et al.* (2007). An absence of cutaneous neurofibromas associated with a 3-bp inframe deletion in exon 17 of the NF1 gene (c.2970-2972 delAAT): evidence of a clinically significant NF1 genotype-phenotype correlation. *American journal of human genetics* 80, 140-151.

Uusitalo, E., Hammis, A., Palonen, E., Brandt, A., Makela, V.V., Kallionpaa, R., Jouhilahti, E.M., Poyhonen, M., Soini, J., Peltonen, J., *et al.* (2014). Neurofibromatosis type 1 gene mutation analysis using sequence capture and high-throughput sequencing. *Acta dermatovenereologica* 94, 663-666.

Vallee, B., Doudeau, M., Godin, F., Gombault, A., Tchalikian, A., de Tauzia, M.L., and Benedetti, H. (2012). Nf1 RasGAP inhibition of LIMK2 mediates a new cross-talk between Ras and Rho pathways. *PloS one* 7, e47283.

Velasco, S., Kedaigle, A.J., Simmons, S.K., Nash, A., Rocha, M., Quadrato, G., Paulsen, B., Nguyen, L., Adiconis, X., Regev, A., *et al.* (2019). Individual brain organoids reproducibly form cell diversity of the human cerebral cortex. *Nature* 570, 523-527.

Venturin, M., Carra, S., Gaudenzi, G., Brunelli, S., Gallo, G.R., Moncini, S., Cotelli, F., and Riva, P. (2014). ADAP2 in heart development: a candidate gene for the occurrence of cardiovascular malformations in NF1 microdeletion syndrome. *Journal of medical genetics* 51, 436-443.

Venturin, M., Guarnieri, P., Natacci, F., Stabile, M., Tenconi, R., Clementi, M., Hernandez, C., Thompson, P., Upadhyaya, M., Larizza, L., *et al.* (2004). Mental retardation and cardiovascular malformations in NF1 microdeleted patients point to candidate genes in 17q11.2. *Journal of medical genetics* *41*, 35-41.

Wang, H.F., Shih, Y.T., Chen, C.Y., Chao, H.W., Lee, M.J., and Hsueh, Y.P. (2011). Valosin-containing protein and neurofibromin interact to regulate dendritic spine density. *The Journal of clinical investigation* *121*, 4820-4837.

Wang, Y., Kim, E., Wang, X., Novitsch, B.G., Yoshikawa, K., Chang, L.S., and Zhu, Y. (2012). ERK inhibition rescues defects in fate specification of Nf1-deficient neural progenitors and brain abnormalities. *Cell* *150*, 816-830.

Wassef, M., Luscan, A., Aflaki, S., Zielinski, D., Jansen, P., Baymaz, H.I., Battistella, A., Kersouani, C., Servant, N., Wallace, M.R., *et al.* (2019). EZH1/2 function mostly within canonical PRC2 and exhibit proliferation-dependent redundancy that shapes mutational signatures in cancer. *Proceedings of the National Academy of Sciences of the United States of America* *116*, 6075-6080.

Welti, S., Fraterman, S., D'Angelo, I., Wilm, M., and Scheffzek, K. (2007). The sec14 homology module of neurofibromin binds cellular glycerophospholipids: mass spectrometry and structure of a lipid complex. *J Mol Biol* *366*, 551-562.

Wilkins, A., Majed, H., Layfield, R., Compston, A., and Chandran, S. (2003). Oligodendrocytes promote neuronal survival and axonal length by distinct intracellular mechanisms: a novel role for oligodendrocyte-derived glial cell line-derived neurotrophic factor. *The Journal of neuroscience : the official journal of the Society for Neuroscience* *23*, 4967-4974.

Wolff, J.J., Gu, H., Gerig, G., Elison, J.T., Styner, M., Gouttard, S., Botteron, K.N., Dager, S.R., Dawson, G., Estes, A.M., *et al.* (2012). Differences in white matter fiber tract development present from 6 to 24 months in infants with autism. *Am J Psychiatry* *169*, 589-600.

World Health, O. (2017). Global accelerated action for the health of adolescents (AA-HA!): guidance to support country implementation: summary (Geneva: World Health Organization).

Yang, F., Xu, Y.P., Li, J., Duan, S.S., Fu, Y.J., Zhang, Y., Zhao, Y., Qiao, W.T., Chen, Q.M., Geng, Y.Q., *et al.* (2009). Cloning and characterization of a novel intracellular protein p48.2 that negatively regulates cell cycle progression. *Int J Biochem Cell Biol* *41*, 2240-2250.

Zhang, M., Wang, Y., Jones, S., Sausen, M., McMahon, K., Sharma, R., Wang, Q., Belzberg, A.J., Chaichana, K., Gallia, G.L., *et al.* (2014). Somatic mutations of SUZ12 in malignant peripheral nerve sheath tumors. *Nature genetics* 46, 1170-1172.

# **Curriculum Vitae**

## **MICHELLE L. WEGSCHEID**

### **EDUCATION**

- 2014-2022 M.D. | Washington University School of Medicine in St. Louis
- 2016-2020 Ph.D., Neuroscience | Washington University in St. Louis
- 2009-2013 B.S., Biochemistry | University of Illinois at Urbana-Champaign  
Highest Distinction. GPA: 3.94/4.00.

### **HONORS AND AWARDS**

- 2021 O’Leary Prize Competition Finalist
- 2019 American Neurological Association Poster Presentation Awardee
- 2019 Children’s Tumor Foundation Conference Poster Competition Semi-Finalist
- 2018 Children’s Tumor Foundation Young Investigator Award
- 2013 Graduated with Highest Distinction in Biochemistry
- 2013 William T. and Lynn Jackson Senior Thesis Award
- 2012 American Society for Microbiology Undergraduate Research Fellowship
- 2012 Helen Alford Hays Undergraduate Research Award
- 2012 Biochemistry Summer Research Scholarship
- 2011 Harvey L. Pretula Memorial Undergraduate Research Award
- 2011 James Scholar Research Award
- 2009-2013 Richard and Mary Shelton Scholarship for academic excellence
- 2009-2013 Edmund J. James Scholar
- 2009-2013 University of Illinois at Urbana-Champaign Dean’s List
- 2009-2011 Wilson Scholarship for academic excellence
- 2009 Applied Health Sciences Scholar Award

### **RESEARCH EXPERIENCE**

- 2016-2020 **Graduate Student Researcher**  
*Washington University School of Medicine in St. Louis*  
Advisor: David H. Gutmann, M.D., Ph.D.  
Dissertation: “Genetic risk factors for neurodevelopmental disorders: insights from hiPSC-cerebral organoids.”
- 2015 **Research Laboratory Rotation**  
*Washington University in St. Louis*  
Advisor: Shelly Sakiyama-Elbert, Ph.D.  
Focus: Nerve regeneration in spinal cord injury models.

- 2014            **Research Laboratory Rotation**  
*Washington University School of Medicine in St. Louis*  
 Advisor: Randall Bateman, M.D.  
 Focus: Amyloid-beta (A $\beta$ ) protein and Apolipoprotein E (ApoE) isoform kinetics in Alzheimer's disease.
- 2013-2014    **Research Assistant**  
*University of Chicago*  
 Advisor: Maciej Lesniak, M.D.  
 Focus: Nanotheranostics for primary and metastatic brain cancers.
- 2010-2013    **Undergraduate Student Researcher**  
*University of Illinois at Urbana-Champaign*  
 Advisor: Brenda A. Wilson, Ph.D.  
 Thesis: "Development and characterization of modular delivery vehicles based on BoNT/A."
- 2009            **Undergraduate Student Researcher**  
*University of Illinois at Urbana-Champaign*  
 Advisor: Charles Hillman, Ph.D.  
 Focus: Correlations between cardiorespiratory fitness and cognition in preadolescent children.

## RESEARCH GRANTS

- 2018-2020    Children's Tumor Foundation grant, "Employing human induced pluripotent stem cells (hiPSCs) to define brain developmental defects in NF1."

## TEACHING/ MENTORSHIP EXPERIENCE

- 2021-2022    **Clinical Mentor**  
*Washington University School of Medicine in St. Louis*
- 2021-2022    **Surgery Clerkship Teaching Fellow**  
*Washington University School of Medicine in St. Louis*
- 2017-2021    **Research Student Mentor**  
*Washington University School of Medicine in St. Louis*
- 2016            **Molecular Foundations of Medicine Course Teaching Assistant**  
*Washington University School of Medicine in St. Louis*
- 2010-2012    **Chemistry Tutor, Office of Minority Student Affairs**  
*University of Illinois at Urbana-Champaign*



2009-2011 **Leadership Program**  
*University of Illinois at Urbana-Champaign*

## **PRESENTATIONS**

- 2021 **Joint Meeting of AAP/ASCI/APSA**  
Poster Presentation: Human iPSC-derived cerebral organoids establish differential effects of germline *NF1* gene mutations.
- 2021 **O’Leary Prize Competition**  
Oral Presentation: Patient-derived iPSC-cerebral organoids establish *CRLF3* as a critical regulator of neurogenesis and a candidate autism risk gene.
- 2019 **Washington University in St. Louis MSTP Works in Progress Seminar**  
Oral Presentation: hiPSC-derived cerebral organoids reveal differential effects of distinct *NF1* gene mutations.
- 2019 **144th Annual Meeting of the American Neurological Association**  
Poster Presentation: Human iPSC-derived cerebral organoids establish mutational specificity in NF1.
- 2019 **Children’s Tumor Foundation International NF Conference**  
Oral and Poster Presentation: Human iPSC-derived cerebral organoids establish mutational specificity in NF1.
- 2017 **Washington University in St. Louis Neuroscience Works in Progress Seminar**  
Oral Presentation: Using stem cell platforms to model brain abnormalities in NF1.
- 2013 **American Society for Microbiology 113th General Meeting**  
Poster Presentation: Development and characterization of modular BoNT/A-based delivery vehicles.
- 2012 **University of Illinois Annual Microbiology Research Conference**  
Poster Presentation: Development and characterization of modular BoNT/A-based delivery vehicles.

## **PEER-REVIEWED PUBLICATIONS**

- 1 Anastasaki, C.\*, **Wegscheid, M.L.\***, Hartigan, K., Papke, J.B., Kopp, N.D., Chen, J., Cobb, O., Dougherty, J.D., and Gutmann, D.H. (2020). Human iPSC-Derived Neurons and Cerebral Organoids Establish Differential Effects of Germline NF1 Gene Mutations. *Stem cell reports* 14, 541-550. **\*co-first authors**

- 2 Anastasaki, C., Wilson, A.F., Chen, A.S., **Wegscheid, M.L.**, and Gutmann, D.H. (2022). Generation of human induced pluripotent stem cell-derived cerebral organoids for cellular and molecular characterization. *STAR Protoc* 3, 101173.
- 3 Cheng, Y., Dai, Q., Morshed, R.A., Fan, X., **Wegscheid, M.L.**, Wainwright, D.A., Han, Y., Zhang, L., Auffinger, B., Tobias, A.L., et al. (2014). Blood-brain barrier permeable gold nanoparticles: an efficient delivery platform for enhanced malignant glioma therapy and imaging. *Small (Weinheim an der Bergstrasse, Germany)* 10, 5137-5150.
- 4 Chung, E.J., Cheng, Y., Morshed, R., Nord, K., Han, Y., **Wegscheid, M.L.**, Auffinger, B., Wainwright, D.A., Lesniak, M.S., and Tirrell, M.V. (2014). Fibrin-binding, peptide amphiphile micelles for targeting glioblastoma. *Biomaterials* 35, 1249-1256.
- 5 Morshed, R.A., Cheng, Y., Auffinger, B., **Wegscheid, M.L.**, and Lesniak, M.S. (2013). The potential of polymeric micelles in the context of glioblastoma therapy. *Frontiers in pharmacology* 4, 157.
- 6 Morshed, R.A., Muroski, M.E., Dai, Q., **Wegscheid, M.L.**, Auffinger, B., Yu, D., Han, Y., Zhang, L., Wu, M., Cheng, Y., et al. (2016). Cell-Penetrating Peptide-Modified Gold Nanoparticles for the Delivery of Doxorubicin to Brain Metastatic Breast Cancer. *Molecular pharmaceutics* 13, 1843-1854.
- 7 **Wegscheid, M.L.**, Anastasaki, C., and Gutmann, D.H. (2018). Human stem cell modeling in neurofibromatosis type 1 (NF1). *Experimental neurology* 299, 270-280.
- 8 **Wegscheid, M.L.**, Anastasaki, C., Hartigan, K.A., Cobb, O.M., Papke, J.B., Traber, J.N., Morris, S.M., and Gutmann, D.H. (2021). Patient-derived iPSC-cerebral organoid modeling of the 17q11.2 microdeletion syndrome establishes CRLF3 as a critical regulator of neurogenesis. *Cell reports* 36, 109315.
- 9 **Wegscheid, M.L.**, Morshed, R.A., Cheng, Y., and Lesniak, M.S. (2014). The art of attraction: applications of multifunctional magnetic nanomaterials for malignant glioma. *Expert opinion on drug delivery* 11, 957-975.